Growth and Characterization of Chalcogenide Alloy Nanowires with

Controlled Spatial Composition Variation for Optoelectronic Applications

by

Patricia Nichols

A Dissertation Presented in Partial Fulfillment
of the Requirements for the Degree
Doctor of Philosophy

Approved November 2012 by the
Graduate Supervisory Committee:

Cun-Zheng Ning, Chair
Ray Carpenter
Peter Bennett
David Smith

ARIZONA STATE UNIVERSITY

December 2012

ABSTRACT

The energy band gap of a semiconductor material critically influences the operating wavelength of an optoelectronic device. Realization of any desired band gap, or even spatially graded band gaps, is important for applications such as lasers, light-emitting diodes (LEDs), solar cells, and detectors. Compared to thin films, nanowires offer greater flexibility for achieving a variety of alloy compositions. Furthermore, the nanowire geometry permits simultaneous incorporation of a wide range of compositions on a single substrate. Such controllable alloy composition variation can be realized either within an individual nanowire or between distinct nanowires across a substrate.

This dissertation explores the control of spatial composition variation in ternary alloy nanowires. Nanowires were grown by the vapor-liquid-solid (VLS) mechanism using chemical vapor deposition (CVD). The gas-phase supersaturation was considered in order to optimize the deposition morphology. Composition and structure were characterized by scanning electron microscopy (SEM), transmission electron microscopy (TEM), energy dispersive x-ray spectroscopy (EDS), and x-ray diffraction (XRD). Optical properties were investigated through photoluminescence (PL) measurements.

The chalcogenides selected as alloy endpoints were lead sulfide (PbS), cadmium sulfide (CdS), and cadmium selenide (CdSe). Three growth modes of PbS were identified, which included contributions from spontaneously generated catalyst. The resulting wires were found capable of lasing with wavelengths over 4000 nm, representing the longest known wavelength from a sub-wavelength

wire. For $Cd_xPb_{1-x}S$ nanowires, it was established that the cooling process significantly affects the alloy composition and structure. Quenching was critical to retain metastable alloys with x up to 0.14, representing a new composition in nanowire form. Alternatively, gradual cooling caused phase segregation, which created heterostructures with light emission in both the visible and mid-infrared regimes. The CdSSe alloy system was fully explored for spatial composition variation. CdS_xSe_{1-x} nanowires were grown with composition variation across the substrate. Subsequent contact printing preserved the designed composition gradient and led to the demonstration of a variable-wavelength photodetector device. CdSSe axial heterostructure nanowires were also achieved. The growth process involved many variables, including a deliberate and controllable change in substrate temperature. As a result, both red and green light emission was detected from single nanowires.

ACKNOWLEDGMENTS

First, I would like acknowledge my advisor, Prof. C. Z. Ning, for his support throughout my graduate career at ASU, for the opportunity to work in an exciting research area, and for challenging me to continually strive for high goals. I also sincerely thank my committee members, Prof. Ray Carpenter, Prof. Peter Bennett, and Prof. David Smith, for their valuable discussions and suggestions. I thank all of the members of the ASU Nanophotonics group for their patience in teaching me electrical engineering concepts. I specifically acknowledge those who contributed to the experiments and interpretation of data in this dissertation: Derek Caselli, Fan Fan, Zhicheng Liu, Minghua Sun, Sunay Turkdogan, and Leijun Yin.

I am thankful for the facilities and technical support in the LeRoy Eyring Center for Solid State Science at ASU. Specifically, I thank Gordon Tam for FIB processing, Timothy Karcher for vacuum and furnace support, Emmanuel Soignard for XRD training, Zhenquan Liu for guidance on TEM, and David Wright for innumerous problem-solving sessions.

I am grateful for Christine Roeger, scientific glassblower at the Glassblowing Facility at ASU, whose talents in quartz processing permitted the CVD advancements in this dissertation. I also acknowledge the helpful research librarians and staff at the Noble Science and Engineering Library. I would like to acknowledge Yolanda Murphy for her guidance and dedicated support in her role as Graduate Academic Advisor for the Materials Science and Engineering Graduate Program.

I would like thank my aunt, Elizabeth Soffer, for her wise advice throughout the dissertation process and for proofreading this document.

Overall, I am incredibly thankful for all of the people who have supported me to get where I am today. I thank my parents, my sister, my family and friends for providing me with a foundation of encouragement and love.

TABLE OF CONTENTS

LIST OF TABLES

LIST OF FIGURES

Chapter 1

INTRODUCTION

An ideal variable-wavelength optoelectronic device requires the incorporation of a wide range of band gap materials on a single chip. The solution to this formidable challenge has revolutionary applications in many scientific and engineering technologies, including lasers, light emitting diodes (LEDs), solar cells, sensors, and detectors. Semiconductor nanowires provide a solution for these technological demands. The growth of semiconductor alloy nanowires with controllable composition variation offers promising, innovative impacts on many technological areas.

In an optoelectronic device, the operating wavelength is strongly dependent on the fundamental band gap of the semiconductor material. Without alloying, band gap values are limited to discrete values corresponding to naturally existing semiconductor elements and binary compounds. Alloying of semiconductor compounds to form a ternary alloy produces new band gaps in between the values of the two original compounds. Unfortunately, this method of achieving wavelength variability is severely limited by existing techniques for planar, epitaxial growth of semiconductor thin films on a crystalline substrate. The thin film lattice constant must be closely matched to the lattice constant of an appropriate crystalline substrate to permit heteroepitaxial growth of high-quality single crystals. Extremely narrow lattice constant mismatch inhibits the creative design of new semiconductor-based optoelectronic devices.

1

Semiconductor nanowires are not subject to strict lattice mismatch restrictions. Due to their small cross sections, semiconductor nanowires can accommodate over 10% lattice mismatch while still maintaining epitaxial growth.[1] Furthermore, nanowires can also be grown on amorphous substrates and crystal substrates with arbitrary lattice constants, whereby substrates merely act as mechanical support. This permits an even larger range of potential alloy compositions.
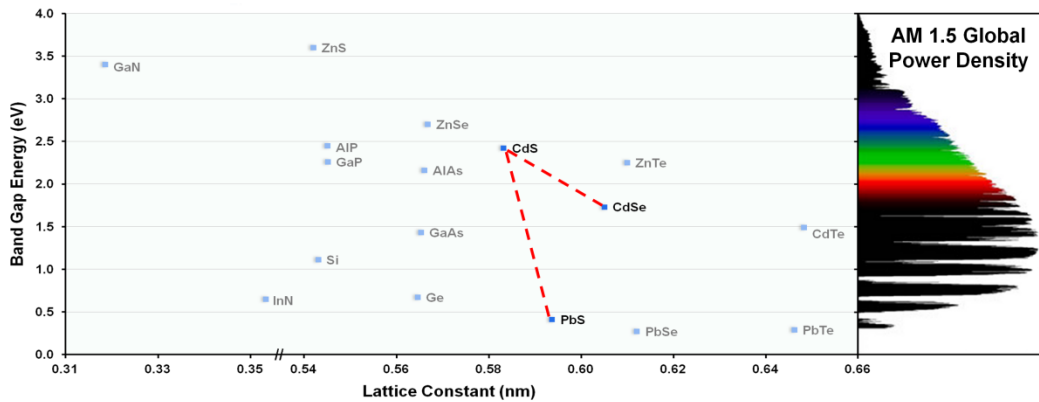
Figure 1. Band gap energy versus lattice constant for common semiconductor materials. Inset, right: solar spectrum.

Figure 1 summarizes the lattice parameter and band gap relationship for common semiconductor materials. For traditional thin film growth, both the thin film and substrate must lie close to a vertical line in order to achieve high-quality, dislocation-free growth. Alloying through nanowire growth is much less constrained. As indicated on the figure, the binary compound materials of interest for this dissertation as alloy endpoints are chalcogenides: cadmium sulfide (CdS), cadmium selenide (CdSe), and lead sulfide (PbS). A chalcogenide is defined as a compound between a group 16 element and a more electropositive element,

although the term is generally reserved for sulfides, selenides, and tellurides, rather than for oxides. Alloys between CdS and CdSe generate a considerable range of band gaps, corresponding to wavelengths in the visible spectrum. A sample with composition variation in this range has applications in multi-spectral photodetection and color-tunable LEDs. Band gaps generated by alloys between CdS and PbS span from the visible to the mid-infrared (IR) spectrum. As compared to the solar spectrum, it is clear that this range includes the spectral window of significance to high-efficiency photovoltaic solar cells.

Nanowires merit investigation for use in optoelectronic devices because the individual nanowire structure intrinsically provides channels for electrical conduction and optical waveguiding.[2] Furthermore, the high-quality crystal material within the nanowires can act as the gain medium required for lasing.[2] Important for absorption-based devices such as solar cells, nanowire arrays can offer significantly enhanced light absorption properties compared to continuous thin films, ultimately leading to improved device performance.[3,4]

In this dissertation, chalcogenide alloy nanowires were created and studied in order to understand spatial composition variation both within individual nanowires and between distinct nanowires across a substrate.

1.1. Alloying and Phase Stability in Nanowires

By definition, nanomaterials have a high surface-to-volume ratio as compared to bulk materials. As size is reduced, the surface atoms play an increasingly crucial role in determining the overall material properties.

Specifically for nanowires, crystal structures and alloy compositions distinct from bulk behavior have been theoretically predicted and experimentally observed.

1.1.1. Modeling Examples

Galicka *et al.* modeled the structure of hexagonal (wurtzite) and cubic (zincblende) nanowires for various diameters.[5] With decreasing nanowire diameter, the surface energy contributes a greater portion to the total energy; thus, surfaces become more influential to determining the stable phase. It was found that the number of dangling bonds at clean, non-saturated surfaces is higher for zincblende than for wurtzite, resulting in higher surface energy for zincblende. Therefore, small diameter nanowires were predicted to be more stable as wurtzite, even if the bulk form prefers zincblende. Another modeling simulation described the compressive stress caused by tensile surface stress along the length direction of nanowires.[6] The surface stress was found to be the driving force for phase transformation into a higher energy metastable crystal structure not typically observed at ambient conditions.

Due to their unconstrained lateral surfaces, nanowires are considered to be able to accommodate strain-relaxed growth. This is particularly relevant for alloys. If two compounds with different equilibrium bond lengths are combined, they may segregate by composition to relieve strain, instead of producing a solid solution. Xiang *et al*. performed detailed modeling of $In_xGa_{1-x}N$ nanowires with x = 0.5, a composition considered to represent the maximum instability for random alloying.[7] They found that the strain energy in the regions near the nanowire lateral surfaces was much less than the strain energy in the bulk regions. The

nanowire configuration was more favorable than bulk for maintaining metastable $In_xGa_{1-x}N$. Practical factors that influence the actual experimental observation of these results include kinetic considerations within non-equilibrium growth processes.

1.1.2. Experimental Examples

Although the theoretical description is still under examination in literature, there are experimental examples of nanowires exhibiting phase and composition behavior distinct from bulk. The $Zn_xCd_{1-x}Se$ ternary alloy can be achieved across the entire composition range, $0 < x < 1$. In bulk material, $x > 0.7$ results in a zincblende structure; $x < 0.5$ results in a wurtzite structure; and $0.5 < x < 0.7$ produces a mixture of both phases.[8] Shan *et al.* grew $Zn_xCd_{1-x}Se$ alloy nanowires over the entire compositional range.[9] They found that nanowires containing $x >$ 0.13 were zincblende, while those with less Zn were wurtzite. Compared to the alloy in bulk form, the crossover from zincblende to wurtzite is suppressed to a much smaller x value. Low dimensional structures such as nanowires have the potential to exhibit phase-composition relationships distinct from bulk.

Another interesting materials system is $In_xGa_{1-x}N$. Because the direct band gap can be tuned from the near-ultraviolet to the near-IR spectrum, $In_xGa_{1-x}N$ ternary alloys have great potential in optoelectronic devices. However, actually producing high quality $In_xGa_{1-x}N$ material over all compositions is not trivial due to spinodal decomposition into In-rich and Ga-rich domains. The large difference in lattice parameter between InN and GaN results in thermodynamically instability over most In-rich concentrations.[10,11] The miscibility gap was

confirmed by attempted growth of thick $In_xGa_{1-x}N$ layers.[12] The resulting

microstructures showed striped composition fluctuations with increasing

amplitude around x = 0.5 - 0.6, the probable center of the miscibility gap.[12]

Another study revealed phase separation, dislocations, and planar defects for thick

films with x > 0.3.[13] Tabata *et al.* also reported phase separation in thick films.[14]

The unique properties of nanowires are essential to achieving growth of

$In_xGa_{1-x}N$ ternary alloys across the entire compositional range. Kuykendall *et al.*

grew nanowires with compositions spanning the entire range on a single substrate

in a single growth run.[15] The miscibility gap predicted for bulk $In_xGa_{1-x}N$ was not

observed. There was no phase separation, and no large variation in composition.

Pendyala *et al.* also demonstrated alloy nanowire growth of a wide range of

$In_xGa_{1-x}N$ materials, deposited onto previously grown GaN nanowires.[16]

Overall, the experimental work supports the proposition that nanowires

can maintain metastable alloy phases that are not easily retained in bulk form.

Nanowires have a complex free energy relationship due to unconstrained lateral

surfaces and a relatively large contribution from surface energy, which can cause

unusual behavior compared to the same composition in bulk form.

1.2. Growth of Nanowires

1.2.1. Substrate Considerations

Heteroepitaxy is defined as the growth of one material onto another. This

process inherently involves a lattice mismatch between the two materials.

Transferring crystallographic directions from the substrate across the growth

interface causes strain in the growing semiconductor. When the growth exceeds

the critical thickness, it becomes energetically favorable to introduce dislocations to relieve coherency strain.

Semiconductor nanowire growth can be considered in a similar manner. Instead of a two-dimensional system of planar growth, the nanowire interfacial dimension is so small that it can be considered a one-dimensional system.[17] Nanowires can accommodate significantly more lattice-mismatch induced strain. Unlike thin films, wires are not constrained laterally. This permits elastic deformation of the lattice parallel to the interface along the nanowire length. The nanowire can relax to its unstrained lattice parameter at a small distance along the nanowire away from the interface.

Nanowires also have a critical size above which it is energetically favorable to introduce misfit dislocations. The critical nanowire radius is dependent on many variables dictated by the materials system, including lattice mismatch and dislocation burgers vector. Modeling predicts nanowire critical radii that are roughly an order of magnitude larger than the critical thickness of the same substrate-thin film system.[17] The lateral relaxation at the nanowire boundary is essential for defect-free epitaxial growth of nanowires with large lattice mismatch.[18] All in all, the nanowire geometry permits creative combinations of semiconductor and substrate, leading to the potential for innovative applications and devices.

Additionally, nanowires can grow non-epitaxially on an arbitrary substrate, which simply acts as mechanical support. Future nanoscale integrated photonic systems may require flexibility of substrate such that the nanostructures

are grown non-epitaxially. Recently demonstrated nanowire-based devices, including photodetectors,[19] waveguide-integrated photoconductors,[20] and electrode connectors,[21] were grown on amorphous or polycrystalline surfaces. In general, the devices showed excellent performance, even compared to equivalent devices made with crystalline bulk. The demonstrated success of non-epitaxial nanowire devices represents an important validation for continued optoelectronic-driven materials research.

1.2.2. Vapor-Liquid-Solid (VLS) Mechanism

The most thoroughly researched growth procedure for nanowires is the vapor-liquid-solid (VLS) mechanism. First demonstrated by the gold-seeded growth of silicon whiskers in 1964 by Wagner and Ellis, the process involves liquid metal droplets as catalysts for unidirectional growth.[22] Continued progress on the initial concept has significantly reduced the diameter of the whiskers, meriting the term "nanowires."

The VLS growth mechanism begins with preparation of the substrate surface. Catalytic metal particles can be introduced by several methods that ultimately achieve similar results. For example, the particles may be deposited directly by the evaporation of a colloidal solution containing particles of a well-defined size.[23] A thin film of metal may be sputtered or evaporated on the substrate. The metal film becomes islands by annealing, either during a separate annealing procedure or simply because the substrate is at elevated temperatures immediately prior and during growth.[23] Autocatalytic or catalyst-free growth describes an exceptional situation to the need for metal particles. In that case, no

8

catalyst is intentionally deposited on the substrate. Instead, if one of the growth components contains a low melting point metal, a liquid catalyst particle may result from its decomposition.[23] The overall function of the catalyst particle is to lower the activation energy of nucleation on the surface.
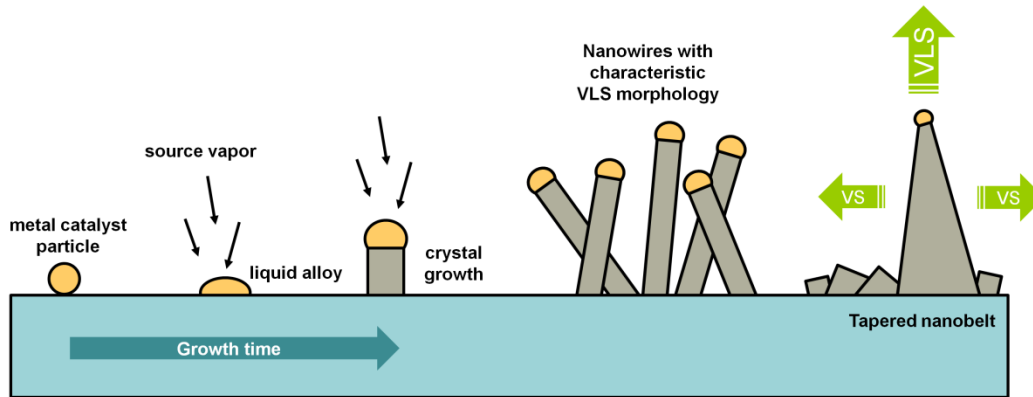
Figure 2. Schematic diagram of VLS and VS growth processes.

As schematically indicated in Figure 2, the next step in VLS growth is to provide source material vapor to the liquid catalyst droplet. The source material vapor pressure can be created by a variety of techniques including chemical vapor deposition (CVD), metalorganic chemical vapor deposition (MOCVD), molecular-beam epitaxy (MBE), pulsed laser ablation, or simply by evaporation.[24] The energy required for incorporation of new material into the liquid particle is much lower than the energy needed to nucleate a new island. According to classical nucleation theory, there is a substantial barrier associated with the formation of a critical nucleation cluster at an atomically flat substrate, known as homogeneous nucleation. Vapor atoms that deposit on the surface in a cluster smaller than the critical size will most likely re-sublime into the vapor phase. If the cluster exceeds the critical size, there is a high probability that it will remain

9

solid on the surface. The catalyst particle acts as a heterogeneous nucleation site. In the original VLS paper, Wagner described the liquid interface of the droplet as "ideally rough;" that is, being entirely composed of steps and ledges, which are accommodation sites for the incoming vapor atoms.[22] This statement assumes that the liquid is undersaturated with respect to the growth species and provides ideal absorption sites for the depositing atoms. When the liquid becomes supersaturated, some sites have the potential to act as desorption sites.[25] Ultimately, the presence of catalyst particles lowers the nucleation barrier at the substrate-nanowire interface, thus promoting preferential growth of nanowires at the liquid catalyst sites.

As the metal particle becomes supersaturated with the growth species, it becomes energetically favorable to crystallize new solid at the particle-substrate interface. Crystallization has been observed to proceed by a layer-by-layer deposition process, which generally creates single crystal material within each nanowire.[26] This process continues such that the semiconductor nanowire increases in length, with the liquid droplet maintained at the tip of the growing wire. If the wires are grown non-epitaxially to the substrate, they will each nucleate and grow in random directions (see Figure 2).

In general, the nanowire diameter is controlled by the catalyst droplet diameter. Additional deposition processes can influence the final morphology. Vapor-solid (VS) growth involves the direct incorporation of vapor into solid material without liquid mediation. This is especially likely to occur on the newly formed crystal material just below the liquid droplet, where the surfaces may be

10

undergoing energy-minimizing reconfiguration.[27] VLS growth of a nanowire in conjunction with continuous VS deposition can result in tapered nanobelt morphology, as shown (right, Figure 2).

1.3. Chemical Vapor Deposition (CVD)

Chemical vapor deposition (CVD) is a common material synthesis method with many possible variations. Overall, gaseous chemical precursors are transported to the vicinity of a substrate, where they react to form solid deposition on the substrate surface. The growth methods developed in this dissertation utilized binary compound powders, thermally sublimated to generate source vapor. The source vapor molecules intermixed at the substrate surface to form solid alloy crystal material. In the system of this work, the entire quartz furnace tube was surrounded by a tube furnace, categorized as a hot wall reactor; on the other hand, a cold wall reactor involves heating the substrate region only. The quartz tube was stable for extended growth times at temperatures up to 1100°C.

In CVD processes, supersaturation is a useful parameter related to the expected morphology of deposition. Generally, supersaturation is defined as the ratio between the actual vapor pressure of source and its equilibrium vapor pressure. This concept was investigated and expanded in more detail for PbS and CdS_xSe_{1-x} growth. Supersaturation indicates the driving force for entering the solid phase from the vapor phase. In CVD growth, epitaxial growth occurs at the lowest supersaturation values, while gas-phase nucleation of powder is promoted at extremely high supersaturations.[28] The general growth trend with increasing supersaturation includes platelets, whiskers, dendrites, polycrystals, and

11

amorphous deposits.[28] A wide spectrum of deposition is achievable by CVD growth. Specifically in the work of this dissertation, catalyst conditions were added to promote one-dimensional nanowire growth. Supersaturation was used to consider the relative contributions of VLS and VS growth to form additional nanostructures, such as tapered nanobelts and bulk crystallites.

For each growth procedure, many growth parameters were adjusted to create the most favorable growth conditions for the desired alloy nanostructures, mainly, source and substrate temperatures, system pressure, flow rate, and growth time. These variables contribute to the supersaturation experienced at the substrate position, which defines the resulting nanostructure morphology as described. Various techniques specifically developed for composition-graded nanowire growth were also employed, including the dual gradient method.[29] Altogether, CVD growth and its associated experimental variables offer the potential to achieve spatial composition variation in nanowire growth.

1.3.1. Post-Growth Treatments

Beyond CVD growth parameters, additional post-growth procedures can dramatically influence the final observed structure and behavior of nanowires. Post-growth treatments are divided into two main categories: thermal considerations during cooling immediately after growth and subsequent defect elimination.

1.3.1.1. Thermal Considerations

At the conclusion of CVD growth, the sample can either be quenched or furnace-cooled. Quenching requires movement of the furnace tube such that the

substrate is relocated to a position outside of the furnace, and a cooling fan is directed onto the exposed tube surface to quickly dissipate the thermal energy through enhanced convection. The cooling rate is very rapid. Alternatively, furnace-cooled implies that the position of the furnace tube is not changed after growth, corresponding to unassisted, gradual cooling to room temperature.

Composition variation within a single nanowire is much more sensitive to cooling procedure than composition variation across a substrate. For composition variation across a substrate, each individual nanowire has a generally uniform composition. The composition changes with position across the sample, with a typical length around 2 cm. For composition variation within a single nanowire, distinct composition regions may only be separated by a few hundred nanometers along the axis of the nanowire. Based on the close proximity of this geometry, diffusion effects are much more likely to blur the composition interface, compromising the heterojunction that divides the two segments. These effects were specifically investigated in CdSSe axial heterostructure nanowires.

1.3.1.2. Defect Elimination

The small diameter of nanowires permits unique post-growth treatment methods for defect elimination. During growth, defects or catalyst metal atoms can become incorporated in the growing nanowire. Nanowires have a large surface-to-volume ratio such that the impurities tend to have lower energy along surfaces. On or near the surface, it is possible to eliminate these defects in ways that are not feasible when they are buried deeply within bulk material. For example, Philipose *et al.* analyzed ZnSe nanowires grown by VLS during CVD.[30]

The photoluminescence (PL) spectrum of the nanowires revealed poor optical properties, with negligible band-edge emission and a very broad defect emission peak, attributed to Zn-vacancies. The same nanowires were then annealed in a Zn-rich atmosphere. The subsequent PL emission behavior was completely reversed, dominated by a strong band-edge emission peak with virtually no defect emission. During annealing, Zn atoms diffused into the nanowires to repair vacancies, which is not possible in bulk materials where many defects are buried too deeply to be penetrated by diffusing Zn atoms. In the case of Au atoms from the initial catalyst particle, it has been found for some growth conditions that they solidify in small clusters along Si nanowire sidewall surfaces.[31] Another study detected the presence of Au atoms in Si wires, but mostly on surfaces.[32] Au can be removed from the surfaces by chemical etching.[32] Passivation of nanowire surfaces was demonstrated through the formation of a self-assembled monolayer of organic molecules. The treatment drastically improved PL emission by promoting recombination corresponding to band-edge emission, thus increasing the signal-to-noise ratio.[33] Nanowires likely contain defects just like thin film and bulk materials, but their unusual dimension properties permit various types of post-growth treatment to effectively reduce defects.

1.4. Characterization Methods

A variety of material and optical characterization methods were required to fully investigate semiconductor alloy nanowires.

1.4.1. Scanning Electron Microscopy (SEM)

Scanning electron microscopy (SEM) was used to characterize the nanostructure morphology and to evaluate the deposition density across the sample surface. In SEM, a focused beam of electrons is scanned across the specimen surface. The high-energy beam electrons, typically around 15 keV, excite electrons in the specimen near the surface. Secondary electron (SE) mode creates an image by collecting the secondary electrons that are ejected from the specimen atoms by inelastic scattering interactions with the beam electrons. Backscattered electron (BSE) mode generates an image by detecting the high-energy beam electrons that are reflected out of the specimen through elastic scattering interactions with the specimen atoms. Backscattering efficiency increases with atomic number; as a result, heavier elements appear brighter than lighter elements in the BSE image. Accordingly, contrast is an indicator of areas with different chemical compositions, which is useful for identifying phase segregation in $Cd_xPb_{1-x}S$ wires. If the specimen excitation volume is large enough, some information about the internal structure is indicated.

For this dissertation, SEM imaging was performed on a FEI XL-30 field-emission SEM with the capability for imaging resolution down to 3 nm.

1.4.2. Transmission Electron Microscopy (TEM)

Transmission electron microscopy (TEM) was crucial to the analysis of the composition, morphology, growth direction, and internal structure of nanowires. Basically, the TEM instrument can be divided into three sections. First, the illumination system includes the electron gun and the condenser lenses,

which serve to focus the beam and direct electrons to the specimen. Second, the electron-sample interaction occurs in the objective lens and stage area of the microscope. This process is the most critical to formation of images and diffraction patterns. Finally, the intermediate and projector lenses of the imaging system magnify the final image or diffraction pattern so that it can be observed on the viewing screen or recorded. Appropriate TEM specimens must be sufficiently transparent to the electron beam, which implies a very thin dimension in the beam direction.

Within the same instrument, scanning transmission electron microscopy (STEM) involves focusing of the electron beam into a narrow spot and rastering it across the specimen surface. The image pixels are collected in series, rather than in parallel as in TEM. Annular dark-field detectors collect high-angle, incoherently scattered electrons. These electrons are highly sensitive to variation in atomic number, which produces a Z-contrast image.

In this work, the nanowires were analyzed in a JEOL 2010F operating at 200 keV. The instrument is equipped with an annular dark field detector and a thin-window light-element-sensitive x-ray spectrometer.

1.4.3. Energy Dispersive X-ray Spectroscopy (EDS)

In both SEM and TEM, the electron beam excites electrons in the specimen. As the excited specimen electron relaxes to its ground state, it emits an x-ray with energy characteristic to that specific element. Energy dispersive x-ray spectroscopy (EDS) analysis collects these characteristic x-rays and provides detailed composition information that corresponds to a SEM, TEM, or STEM

image. EDS is highly accurate for qualitatively indicating the presence of an element within a specimen. On the contrary, quantitative analysis of EDS spectra are subject to errors up to 5 - 10% due to instrument constraints or data processing techniques, including detector efficiency, background subtraction, peak fitting, and assumptions on x-ray fluorescence and absorption.

1.4.4. X-Ray Diffraction (XRD)

X-ray diffraction (XRD) provides important information on the phases and lattice parameters of alloy crystal material present within nanostructures. This information is acquired through interpretation of the scattered intensity resulting from an x-ray beam incident on a sample. High intensity peaks result from coherent interference when Bragg's law is satisfied:

$$n\lambda = 2d \sin(\theta),$$

where n is an integer, λ is the wavelength of the incident x-ray radiation, d is the spacing between the atomic planes in the lattice, and θ is the diffraction angle between the incident radiation and the scattering plane. The as-grown samples in this dissertation contain many randomly oriented wires. This configuration of small single crystals is equivalent to a randomly distributed powder or polycrystalline material. For this reason, the powder method, or θ-2θ scan, was selected. In this setup, θ is scanned through a wide range of values with the detector located at 2θ. High intensity peaks correspond to the atomic plane spacing, which can be reduced to the lattice parameter by indexing of crystal planes. Also, experimental peak positions can be compared to data files for known crystalline materials; however, many alloy materials do not have existing powder

diffraction data. Therefore, Vegard's law was employed to interpolate the lattice parameter of detected alloy phases. Vegard's law is an empirically defined relationship in which a linear relation exists between the lattice parameter of an alloy and the concentrations of the constituent materials.[34]

XRD data was collected on a PANalytical X'Pert Pro Materials Research X-ray Diffractometer equipped with copper K_α radiation.

1.4.5. Photoluminescence (PL)

All of the chalcogenides in this dissertation are direct band gap semiconductors, meaning that the conduction band minimum energy and valence band maximum energy occur in the same position in k-space. This band structure geometry promotes the likelihood of radiative recombination of electrons and holes. During a PL measurement, a laser beam is directed onto the sample surface. The laser beam is made up of photons with energies greater than the band gap of the sample. When illuminated, many electrons in the sample are excited across the band gap into the conduction band. Then, they quickly thermalize to the band edge. Finally, each electron has the potential to return to its non-excited state *via* direct recombination with a hole in the valence band, created by the original excitation process. During this recombination process, a photon is emitted. Consequently, the wavelength of the detected light emission corresponds to the band gap of the material. PL characterization is useful for defining the band gaps of new alloy materials.

PL measurements were performed in the C. Z. Ning research group optical laboratory. The laser excitation source was selected depending on the band gap

range of the alloy material. Temperature-dependent PL measurements were performed with the specimen contained in a cryostat chamber in conjunction with liquid nitrogen (down to 77 K) or liquid helium (down to 4 K). In order to simultaneously collect two useful forms of optical information, the light emitted from the sample was divided using a beam splitter. Some of the signal was directed to the spectrometer to quantitatively measure the intensity from each wavelength, while the rest of the signal was focused into a camera for ultraviolet-illuminated (UV) PL imaging.

Chapter 2

PbS WIRES

PbS is important for a wide range of applications including mid-IR emission and detection,[35,36] electroluminescence,[37] lasers,[38-41] solar cells,[42] and thermophotovoltaics.[43] As a direct band gap material with a small band gap around 0.4 eV, PbS has the potential for very efficient mid-IR emission due to its nearly symmetric conduction and valence bands. The similar effective masses of electrons and holes near the band edge increase efficiency of electron-hole recombination and reduces the probability of Auger recombination, an important non-radiative process in competition with radiative recomination in narrow gap semiconductors.[44,45]

Specifically for PbS in nanowire form, numerous methods for growth have been demonstrated, including chemical vapor deposition,[46-53] hydrothermal,[54-57] solvothermal,[52,58-63] template-assisted solvothermal,[64,65] and template-assisted electrochemical deposition.[66] The growth of large PbS whiskers with 140 micron width and 400 micron length was reported in 1971 by heating solid bulk PbS in a vacuum chamber.[67] Of the more recent CVD methods, some report growth without intentionally introducing any metal catalyst material,[46-51] while others demonstrate the use of various catalyst metals including gold, titanium, chromium and lead.[52,53] Several issues remain before PbS can be fully explored for various applications. Markedly, all of the reported CVD methods use $PbCl_2$ and S powder precursors. The use of $PbCl_2$ in the presence of H_2 gas leads to the formation of HCl which can result in surface roughening by etching.[48] In addition, separate

20

sources of Pb and S require careful balance to produce stoichiometric materials. A systematic and unified understanding of various growth modes is essential for controlled synthesis with desired morphologies.

In this chapter, a simple CVD method was utilized for the growth of PbS wires. By systematically studying growth conditions to achieve various wire and bulk morphologies, three growth modes were identified and related to gas-phase supersaturation.[68] The role of catalyst was studied with and without intentional pre-deposition of metal. PL revealed strong band-edge emission, indicative of the high material quality. Single wires exhibited lasing behavior in the mid-IR spectrum, representing the longest lasing wavelength from an optical cavity with two sub-wavelength dimensions.

2.1. Growth Procedure

PbS wires were grown in a horizontal quartz tube furnace (Lindberg/Blue M Three-Zone Tube Furnace) with stoichiometric PbS powder (Strem Chemicals, Lead (II) sulfide (99.999%)) as the source material in the high temperature zone (see Figure 3). The substrate, Si (100) with or without intentionally added catalyst, was placed on a quartz plate in the low temperature. The temperature zones were isolated by ceramic fiber insulation (Kaowool). The system was evacuated to a pressure of <100 mTorr. Under flowing N_2 or Ar + 5% H_2 at 50 sccm, the pressure was maintained around 15 Torr. After the furnace reached the set temperatures in the high and low temperature zones, the PbS source was inserted into the center of the furnace *via* a magnetic loading rod. The PbS source

powder was sublimated in the high temperature zone, and deposited onto the substrates in the low temperature zone about 10 cm downstream.
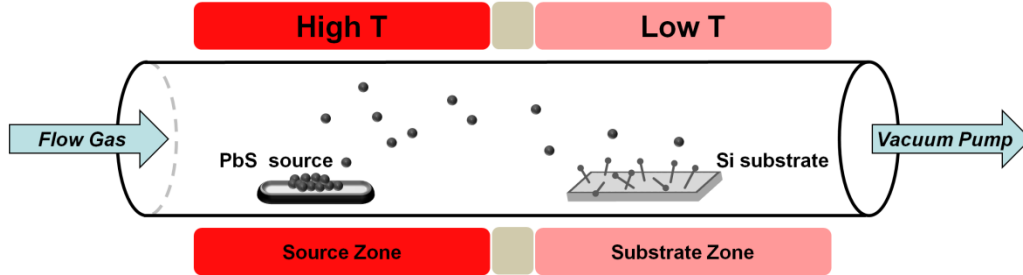
Figure 3. Schematic diagram of furnace system setup indicating high temperature source sublimation zone and low temperature deposition zone.

2.2. Materials Characterization

A diverse range of PbS deposition morphologies resulted from the growth experiments, as summarized in Table 1. The samples were characterized by SEM, XRD, TEM, and EDS.

Table 1. Summary of PbS growth conditions and results (S: Supersaturation)

Figure	Catalyst	Gas	Nominal Source Temp (°C)	Nominal Substrate Temp (°C)	Growth Time (min)	Observed Growth Modes			S
						VLS wires on substrate	VS bulk crystallites	VLS wires on bulk	
4	None	Ar + 5% H_2	600	400	10	✓			Low
5	Pb	N_2	730	450	7	✓	✓		High
6	Pb	N_2	700	500	7	✓	✓	✓	Interm.
7	Pb	N_2	670	500	7		✓	✓	Interm.

2.2.1. SEM

SEM images in Figure 4 are typical as-grown PbS wires on Si(100) with no intentionally added catalyst. There are many distinct, individual wires with minimal deposition of other morphologies. The wires have a square cross section with approximately 1 micron diameter and 10 micron length. The wires show no

orientation relationship with each other or the substrate, indicating wire nucleation directly from the substrate in random directions. These wires show a larger diameter than the diameters reported in literature for PbS CVD growth, ranging from 30 - 350 nm.[46-53] Larger diameters are especially beneficial for many IR optical applications since they provide more optically active material and serve as better waveguides for such long wavelengths in the mid-IR regime.
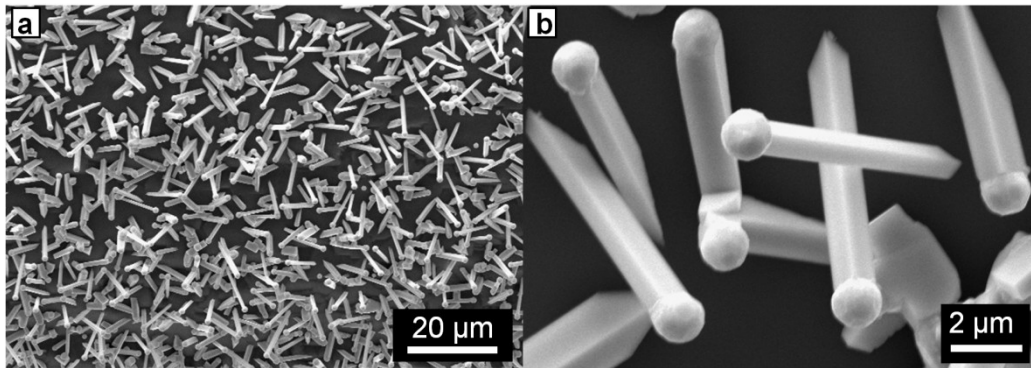
Figure 4. SEM images of as-grown PbS wires with (a) wide area of coverage and (b) direct nucleation from the substrate surface.
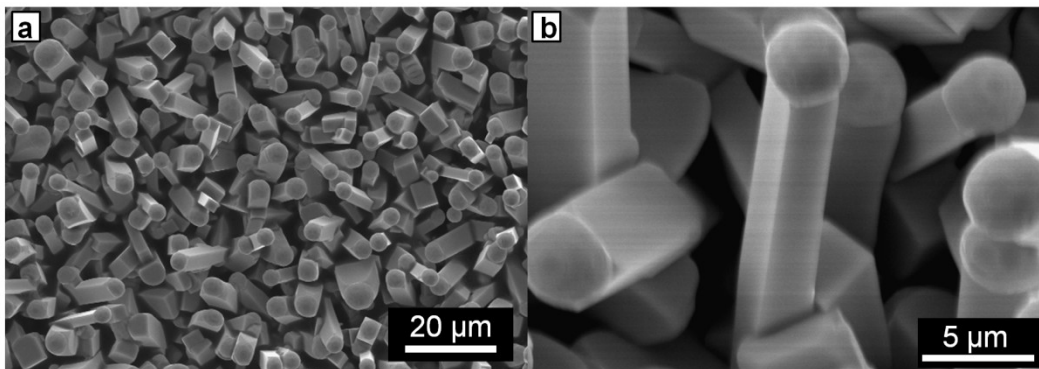
Figure 5. SEM images of as-grown PbS wires with Pb catalyst with (a) dense coverage across the substrate surface and (b) bulk crystallites between the wires.

Growth experiments were also completed with thin Pb catalyst layers deposited prior to the growth process. An approximately 6 nm thick Pb film was evaporated onto Si(100) substrates. The Pb catalyst sample in Figure 5 shows wires with square cross sections, diameters from 3 - 5 microns, and lengths

23

around 20 microns. The wires are surrounded by bulk crystallite deposition. The

sample in Figure 6 was also grown with Pb catalyst film, but with different source

and substrate temperatures than those shown in Figure 5. The growth produced

domains of similarly oriented wires. Figure 7 represents another set of

temperature conditions with Pb catalyst, revealing tapered wires extending from

bulk crystallites.
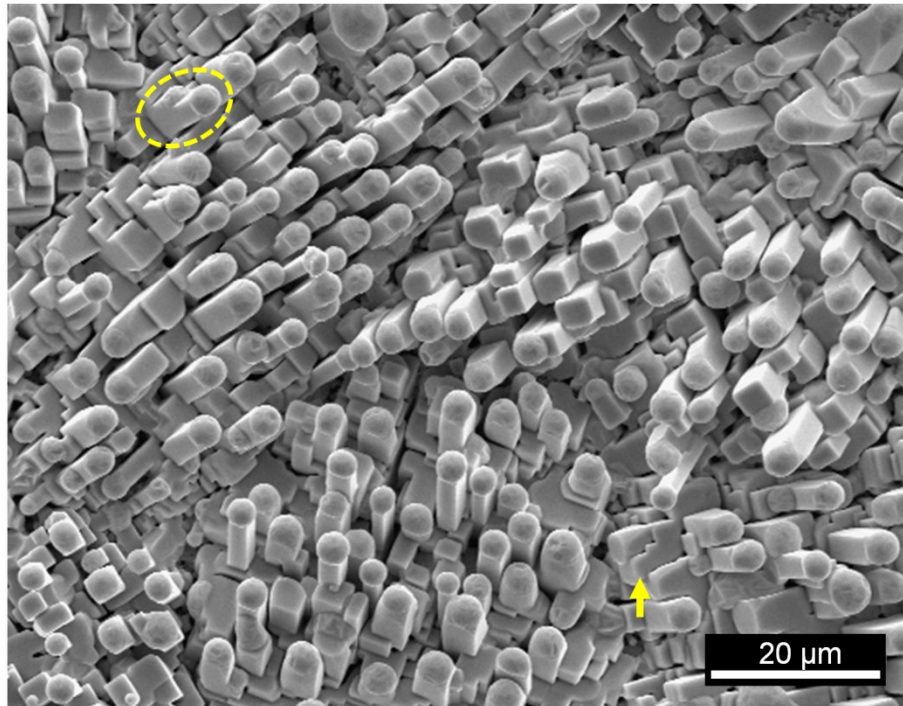
Figure 6. Pb-catalyzed PbS wires with local orientation domains. Arrow indicates
an area of bulk crystallite deposition. Dashed circle indicates example of VLS
wire growth nucleating on top of bulk.
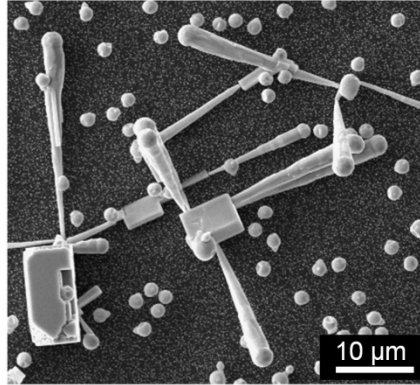
Figure 7. VLS growth of wires on top of PbS bulk.

2.2.2. XRD

XRD was performed on PbS wire samples with a representative scan shown in Figure 8. The peaks are indexed to PbS and Pb as labeled. There were no undesirable oxide phases detected. The PbS phase has cubic NaCl rocksalt structure with calculated lattice parameter of 0.59 nm which matches well with the known PbS lattice parameter of 0.5934 nm (JCPDS card no. 01-077-0244). The remaining peaks index to Pb with lattice parameter of 0.49 nm which is in good agreement with the known lattice parameter of 0.49493 nm (JCPDS card no. 703-065-2873). The sharp peaks indicate high-quality crystal.
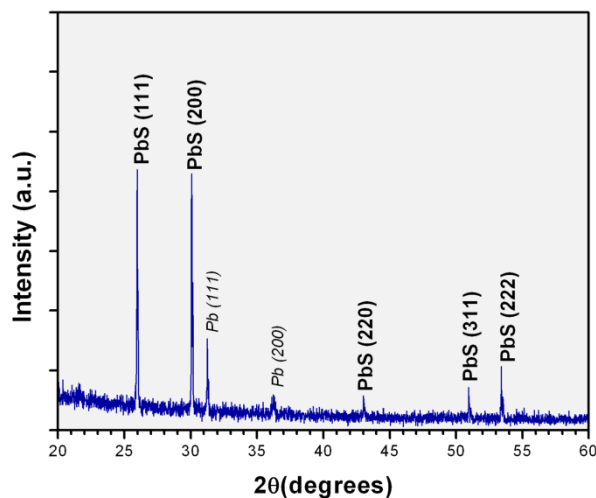
Figure 8. XRD of as-grown PbS wires indexed to corresponding reference peaks.

2.2.3. Individual Wire Analysis

In order to confirm the location of elemental Pb detected by XRD, TEM was necessary to individually probe wires grown without intentionally added catalyst and their round caps. Typical nanowires can be directly dispersed onto a lacy carbon grid for TEM analysis, but due to the large diameter of these PbS wires, auxiliary processing was necessary to create a TEM specimen with electron transparency for high resolution TEM imaging and EDS analysis.

2.2.3.1. Specimen Preparation

The focused-ion beam (FIB) thinning process for PbS wires was modified from a common lift-out procedure for semiconductor devices. First, PbS wires (grown by conditions of Figure 4) were dispersed onto a clean Si substrate (Figure 9a). The wires were encased in layers of platinum (Pt) to protect the wire during lift-out. Electron-beam-induced deposition was used for the first layer of Pt to protect the PbS wire because the electron beam generally does not ablate material; ion-beam-induced deposition of Pt at a much faster rate of deposition then completed the encasement. Trenches were milled on either side of the wire using the Gallium ion beam milling (Figure 9b). The Pt tip was welded to the Pt encasement, and the entire structure was lifted out of the Si wafer (Figure 9c). The wire was attached to a TEM grid using more Pt, and the Pt tip was disconnected from the structure using Ga ion beam milling (Figure 9d). Stage tilt and rotation positioned the structure for perpendicular thinning on both sides. As milling continued, the Ga ion beam current and energy were decreased to minimize amorphization and ion-implantation damage to the PbS crystal.
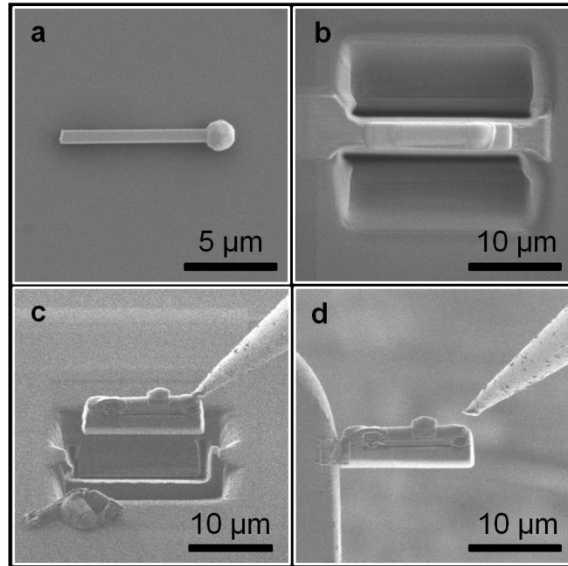
Figure 9. Representative SEM images of FIB processing to create TEM specimen. (a) Wire dispersion on a clean Si substrate, (b) encasement of the wire with Pt and milling trenches on either side, (c) lift-out using Pt tip, and (d) attachment to TEM grid.

The final PbS structure is approximately 50 nm thick with original wire material in the TEM beam direction and residual Pt on the wire sidewalls (inset, Figure 10). The FIB process for TEM sample preparation exposes the wire cap and body for separate elemental and crystallographic analysis.
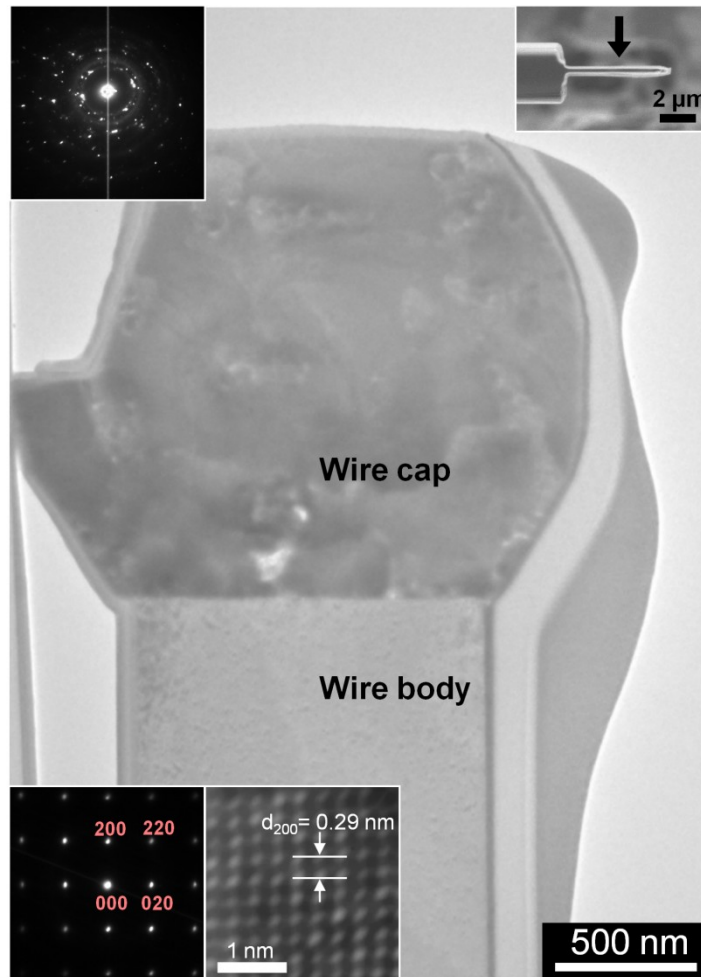
Figure 10. TEM images and diffraction patterns from thinned PbS wire. Inset, top right: SEM image of wire cross section. Arrow represents TEM beam direction.

2.2.3.2. TEM

Figure 10 contains TEM image of the PbS wire and cap. The diffraction pattern of the round cap shows rings of spots due to the polycrystalline grain structure. The diffraction pattern from the PbS wire reveals the <100> zone axis, with the (200) diffraction spots parallel to the wire sidewall, indicating that the wire growth direction is <100>. This is consistent with the square cross section of the wires, which is the equilibrium shape for a wire with (200) planes constructing the sidewalls of the structure. The high resolution TEM image shows lattice fringe

spots with an average spacing of 0.29 nm which corresponds well to the actual

0.2967 nm (200) spacing of bulk PbS, also confirming <100> growth direction.

2.2.3.3. EDS

EDS point scans were performed on the cap and body regions of the wire.

There are some challenges involved in the EDS analysis of PbS due to overlap

between the Pb M_α absorption edge and S K_α line. For this analysis, it is assumed

that the peak around those energies is attributed to S K_α, and the Pb L line was

taken as the Pb signal strength for quantitative calculation. Strong peaks from Pb

and S are apparent in the EDS spectrum with no unexpected impurity elements.

According to quantitative analysis, the molar ratio of S to Pb in the wire body is

1 : 1.1, which is consistent with the expected stoichiometric PbS crystal, and is

within experimental error due to x-ray peak overlap and FIB processing damage.

This amount of deviation from stoichiometry is similar to other reported

quantitative EDS analysis of PbS nanostructures.[52,69] The molar ratio of S to Pb in

the round wire cap is 1 : 8.4. This indicates that the cap contains some PbS in

addition to significant amounts of metallic Pb. The measurement of the isolated

Pb-rich cap is consistent with the wire growth mechanism of nucleation by

spontaneously generated Pb and subsequent VLS growth, as will be proposed.

2.3. Unification of Growth Modes

Based on the diverse morphologies observed in SEM, it is apparent that

multiple processes generate nanowire and bulk deposition during growth

depending on the experimental parameters. Here the growth modes are identified

and evaluated in terms of gas-phase supersaturation.

29

2.3.1. Origins of Catalyst

First, it is interesting to understand several possible origins and role of catalyst in the formation of various morphologies. For samples without intentionally added Pb film, some Pb is spontaneously generated to supply the required metal catalyst for VLS wire growth. There are two ways that Pb catalyst particles can form depending on the presence or absence of H_2. In the first case, H_2 present within the carrier gas is expected to reduce some PbS vapor to form volatile sulfur compounds, thus isolating elemental Pb atoms to be carried downstream.[50] Similar behavior has been observed for the reduction of $PbCl_2$ in PbS CVD growth.[48-51] The Pb vapor then condenses on the substrate, becoming the liquid catalyst for subsequent VLS growth of PbS wires. The importance of H_2 gas for consistent growth of PbS wires catalyzed by spontaneously generated Pb was identified by Bierman *et al.*, and they used SEM-EDS to verify the presence of a Pb-rich cap of a PbSe wire.[48] In this dissertation, the mechanism is further verified by the TEM-EDS analysis of PbS wires. Alternatively, without H_2 gas, PbS can incongruently sublimate to continually provide catalyst in the form of elemental Pb vapor.

For samples grown with pre-deposited catalyst, there are two sources of catalyst metal for the VLS growth: the pre-deposited layer on the substrate and the spontaneously formed catalyst particles as described above. PbS wires nucleated by Pb, either pre-deposited or spontaneously generated, are self-catalyzed, meaning that the metal catalyst is an element of the semiconductor compound to be grown, as opposed to a foreign metal such as Au.

30

2.3.2. Identification of Growth Modes

From the growth experiments and materials characterization, several growth modes and their associated mechanisms are proposed. The VLS growth mechanism is very common and well established for the growth of wires. A characteristic feature of VLS is a metal-rich round cap at the tip of the wire. As the wire grows, this liquid droplet remains on the top of the wire as solid material crystallizes at the bottom of the liquid droplet. The liquid droplet serves as the catalyst because it lowers the activation energy of nucleation and promotes subsequent one-dimensional growth.[23] All of the SEM images show some PbS wires with round caps.

If the conditions are such that the energy required for vapor incorporation into the VLS liquid droplet is similar to that of the energy required for vapor to form a critical nucleation cluster directly on the substrate surface, then wire growth and bulk growth can occur simultaneously, although possibly at different rates. VS deposition is the proposed mechanism for the growth of bulk crystallites with flat facets without metal caps, see Figure 5b, Figure 6 (arrow), and Figure 7. In the VS process, source vapor condenses to the substrate, and the molecules arrange to maintain structural symmetry, creating a nucleation center.[27] Additional vapor molecules incorporate directly onto the solid to form the lowest energy surfaces possible, which tend to be flat facets. As in Figure 6, the wires with round caps are taller than the surrounding flat crystallites, indicating that the one-dimensional VLS growth rate is faster than direct incorporation into the solid by VS.

31

A third growth mode, VLS wire growth on bulk-like crystallites, is proposed to account for the SEM evidence of wires connected directly to PbS bulk crystallites. In this case, wires are nucleated from the spontaneously generated catalyst particles that developed on top of the already formed bulk crystallites. Since the base of the wire is sometimes surrounded by bulk crystallites as in Figure 5b and Figure 6, it is not always possible to definitively distinguish which wires are nucleated by the original pre-deposited Pb or incoming Pb vapor. Figure 7 shows an area of dilute bulk deposition with individual reversely tapered wires clearly nucleated on top. The diameter of the wire increases with growth, from 500 nm to 2 microns. This is consistent with the proposed mechanism of spontaneous formation of Pb catalyst, whereby continually incoming elemental Pb adds to the existing catalyst cap. The liquid droplet, which defines the diameter of the growing wire, is continuously increasing in volume; thus, the diameter of the wire increases correspondingly.[70-72] In both Figure 6 and Figure 7, an orientation relationship is observed between the bulk and the wires nucleating on top. It appears that the wires on top of bulk crystallize homoepitaxially to the flat PbS surface below, as verified for other materials systems, including GaSb.[73] In summary, the observed PbS growth is divided into three categories: VLS wires nucleated directly from the substrate, VS of bulk crystallites, and VLS wire growth nucleated by spontaneously formed Pb on top of the bulk crystallites.

2.3.3. Gas-Phase Supersaturation

In order to investigate the favorable growth conditions for each growth

mode, the samples were organized by their distinct PbS gas-phase

supersaturations. Gas-phase supersaturation, S, is formally defined as:

$$S = \frac{p - p_0}{p_0}$$

where p is the actual gas phase pressure and p_0 is the equilibrium vapor

pressure.[74] Gas-phase supersaturation at the substrate is estimated by considering

the magnitude of the source temperature and the difference between the source

and substrate temperatures. The magnitude of the source temperature controls the

rate of sublimation from the source powder, as the vapor pressure of PbS

increases with temperature.[75] When the source temperature is low (~ 600 °C),

there is very little vapor available to move downstream to the lower temperature

substrate zone. This results in low supersaturation over the substrate. Nearly all of

the precipitation from vapor phase can be accommodated by the VLS liquid

droplets. The rate of incorporation of new material into the liquid particle is much

larger than incorporation onto the substrate surface. When the source temperature

is high (> 650 °C), large amounts of vapor are available to move downstream. If

this vapor transitions to a moderately high substrate temperature zone, the

supersaturation is intermediate. The precipitating vapor can crystallize into both

VS bulk crystallites and VLS wires. There is substantial thermal energy at the

substrate that provides high mobility to the atoms on the substrate so they can

arrange into large grains or domains of similar orientation as in Figure 6.

Subsequently, VLS growth can occur on top of these ordered bulk crystallites as previously described. If large amounts of vapor immediately encounter a much lower temperature zone, there is high supersaturation at the substrate. The vapor crystallizes rapidly, favoring VS growth of bulk crystallites. Transition of the PbS vapor to solid occurs too rapidly to be completely accommodated by VLS liquid particles. Growth at even higher supersaturations than listed in Table 1 generally produce only bulk crystallite morphology. In general, samples grown at different supersaturation conditions reveal a complex growth process with the possibility for three simultaneous growth modes.

2.4. PL

PL is one of the most important methods of characterization for materials with optoelectronic applications. Unfortunately, PL measurement in the mid-IR range is more challenging due to typically weak emission, limited detector availability, and atmospheric absorption. Previous literature reports of PL measurements on PbS wires are limited to quantized structures with PL emission extremely blue-shifted away from the bulk value. The wires studied by Paleta *et al.* have diameters of 1.8 nm with band-edge emission at 480 nm.[61] Wu *et al.* reported PbS nanowires with 30 nm diameter with PL emission peaks at 365 nm and 678 nm.[53] The optical properties of quantized PbS structures are completely different from the mid-IR optical properties of the PbS wires in this work. The large wires obtained here do not show any quantization and allow the fundamental band gap emission in the mid-IR wavelength range to be studied. As displayed in

34

Figure 11, very strong band-edge emission is observed with no defect emission, indicating high quality wires.
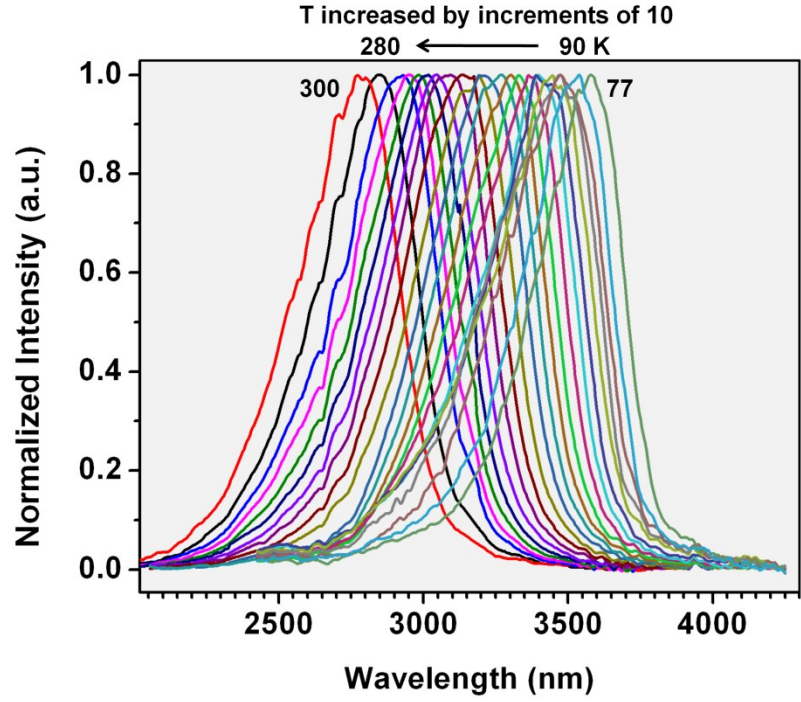
Figure 11. PL spectra measured at various temperatures showing band edge emission with blue-shift with increasing temperature. Dips are due to atmospheric absorption.

A change in temperature modifies two main behaviors within a semiconductor crystal: vibration of ion cores around equilibrium positions and the overall spacing of said equilibrium positions. Each of these effects provides a contribution to the change of band gap with temperature. The band gap (E_0) temperature dependence can be written as:

$$\left(\frac{\partial E_0}{\partial T}\right)_P = \left(\frac{\partial E_0}{\partial T}\right)_V - \alpha B \left(\frac{\partial E_0}{\partial P}\right)_T,$$

where α is the volume coefficient of thermal expansion, and B is the bulk modulus.[76]

The first term describes the effect of the electron-phonon interactions. With increasing temperature, the ion core vibrations increase in amplitude, which influences the behavior of the electrons. For most semiconductors including PbS, this term is positive.[76]

The second term considers the contributions from lattice effects. With temperature, the equilibrium positions of ions within the lattice either expand or contract depending on the magnitude of α, which is positive for PbS.[77] The bulk modulus of a material describes its resistance to uniform compression, which is positive for all materials. Finally, the second term also contains the band gap pressure coefficient, which is negative for PbS.[76] Under hydrostatic pressure, the ion cores are compressed such that the lattice constant is reduced while structural symmetry is maintained.[78] Even small changes in lattice constant have large electronic effects, observable on the band structure. As neighboring Pb and S ions come in closer proximity to each other, strong p-d wave function mixing occurs. This serves to increase the energy of the valence band relative to the conduction band at the L position, thus decreasing the band gap with increasing pressure.[79] All of these combined contributions lead to a positive value of the total temperature band gap coefficient. Accordingly, the band-edge emission peak from PbS wires in Figure 11 shows obvious blue-shift with increasing temperature, consistent with the established behavior of bulk PbS.[80]

As previously mentioned, the strong light emission of PbS is a result of symmetric band structure which enhances the radiative process and inhibits the non-radiative processes such as Auger recombination. The high-quality crystal

and strong light emission make PbS an appealing material for optoelectronic applications in the mid-IR wavelength range. This is especially important since emission sources in the wavelength range around 3 microns are rare and typically very weak due to various competing non-radiative processes.

2.5. Device Application: Mid-IR Lasing

As introduced, PbS intrinsically provides a band structure that favors strong radiative recombination. The growth procedure developed here resulted in high-quality crystal PbS material. The combination of these two aspects permits the PbS wires produced here to achieve lasing. Single-wire measurements were performed on individual PbS wires as shown in Figure 4. The flat and parallel sidewalls defined an appropriate optical cavity for minimal losses. The lasing results are summarized in Figure 12. At 10K under optical excitation (Ti:sapphire laser, SpectraPhysics Tsunami, 800 nm, 150 fs pulse duration, 80 MHz repetition rate) with initially low laser power, only a broad band of spontaneous emission is observed. With increasing lasing power, one lasing mode around 4140 nm becomes dominant and obvious over the broad background. Eventually the spontaneous emission saturates, while the simulated emission continues increasing to extremely high intensities (note the change in vertical axis scale).
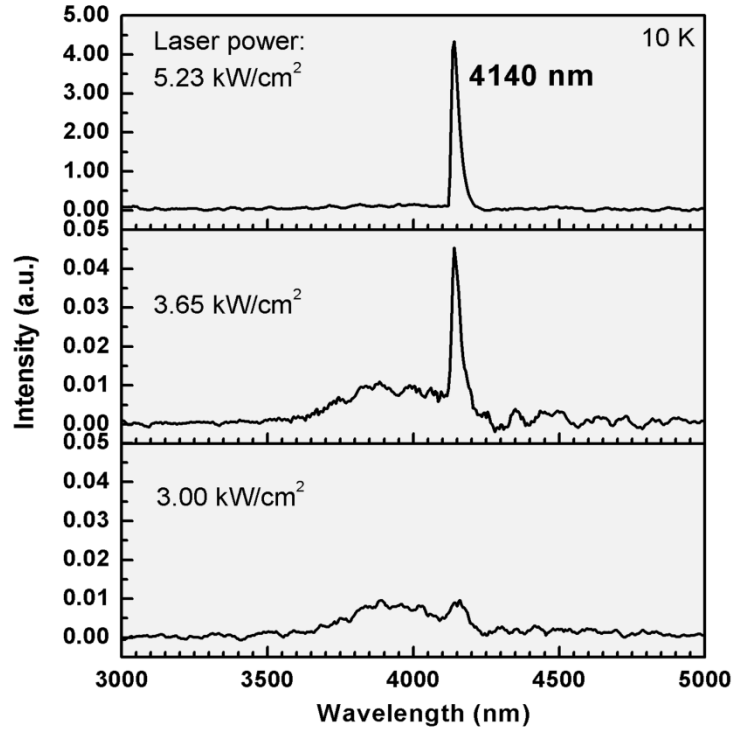
Figure 12. Individual PbS wire lasing at 10 K.

In comparison, literature examples of long wavelength emission from nanowires include GaSb lasing at ~1600 nm[81] and InAs emission around 3000 nm.[33] The result here with lasing beyond 4000 nm represents the longest reported lasing wavelength from a wire structure with sub-wavelength optical cavity dimensions.

2.6. Summary

In conclusion, high quality PbS wires were produced by a simple CVD synthesis method, utilizing pure PbS powder as the source material. The growth conditions for PbS wires are promising for integration with silicon-based electronics because the potentially low substrate temperature is compatible with traditional integrated circuit processing. Temperature-dependent PL showed strong band-edge emission in the mid-IR up to room temperature, and lasing was achieved with a wavelength over 4000 nm. The <100> growth direction and the

VLS growth mechanism were confirmed by FIB thinning, subsequent TEM imaging, and EDS. Multiple catalyst sources, both pre-deposited or spontaneously formed, contribute to the growth of PbS wires.

Growth modes were systematically investigated under different growth conditions, resulting in VLS growth of wires directly from the substrate, VS deposition of bulk crystallites, and subsequent VLS wire growth on top of the bulk crystallites. Gas-phase supersaturation relates the growth modes to the experimental parameters, with VLS on the substrate dominating at low supersaturation and VS growth of bulk crystallites dominating at high supersaturation. The effect of supersaturation on the appearance of wires and bulk crystallites is important to CVD growth of various morphologies and compositions of nanostructures. Such systematic understanding of various growth modes greatly contributes toward achieving synthesis by design, or achieving nanowires of a given morphology by controlled experimental conditions.

Chapter 3

Cd$_x$Pb$_{1-x}$S ALLOY NANOWIRES

A phase diagram displays the thermodynamically predicted equilibrium phases that occur in a bulk materials system for a given pressure and temperature range. Each distinct phase represents the most stable configuration, which has no driving force to change over time. As shown in Figure 13, the stable equilibrium state is represented as a global minimum in a plot of Gibbs free energy versus all possible atomic arrangements. However, a materials system exhibits many other configurations in addition to the equilibrium phase. If the Gibbs free energy of a configuration sits at a local minimum position, then that configuration corresponds to a metastable state.
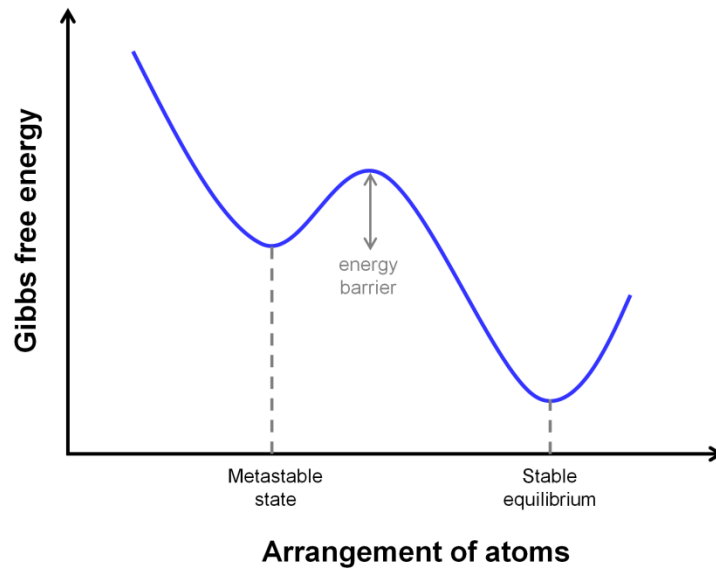
Figure 13. Plot of Gibbs free energy versus arrangement of atoms, schematically depicting metastable and equilibrium states.

Transformation rates can be incredibly slow such that metastable phases can be sustained at ambient conditions, even over long periods of time.

Thermodynamic calculations do not predict the rate of phase transformation; thus, kinetic considerations are required to understand changes over time. In general, large energy barriers lead to slower transformation rates. Many interesting engineered materials take advantage of metastable phases to produce useful material properties. Additionally, phase diagrams are constructed for bulk materials with large volumes relative to surface area. Therefore, low-dimensional materials, such as quantum wells, thin films, nanowires, nanoparticles and quantum dots, frequently exhibit phase and alloying behaviors distinct from those described by phase diagrams.

The CdS-PbS alloy system is a pseudo-binary system with a large miscibility gap in the solid phase region, as shown in the phase diagram (Figure 14). Within the solid region, it is thermodynamically favorable for the crystal to segregate into separate Pb-rich cubic and Cd-rich hexagonal phases. On the Pb-rich side of the phase diagram, the solid solubility of Cd in the PbS cubic phase is up to 24 mole percent at 920°C.[82] On the Cd-rich side, the measured solubility of Pb in the CdS hexagonal phase is negligible, even up to temperatures near the melting point.
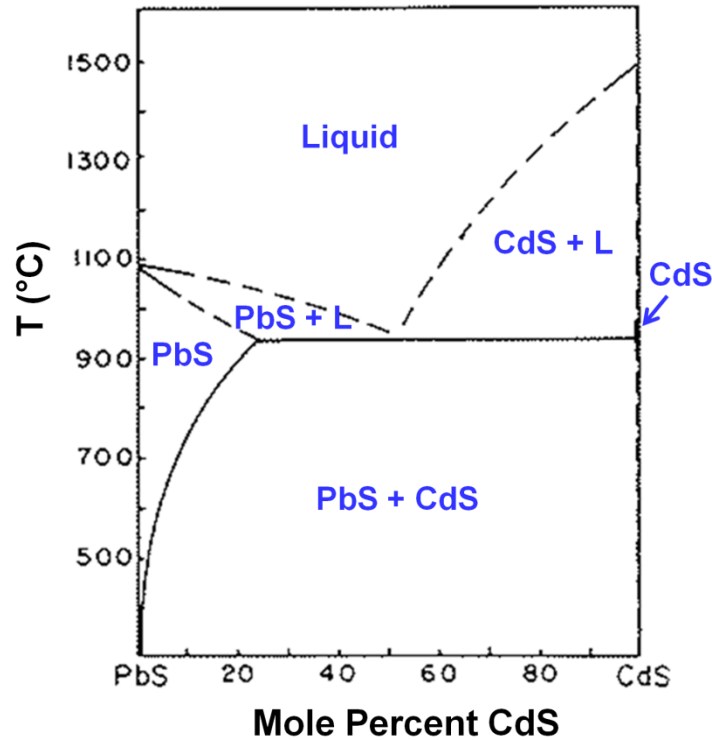
Figure 14. Experimentally determined phase diagram for the CdS-PbS system. Adapted from Bethke and Barton.[82]

The main crystal structure of PbS is cubic with NaCl rocksalt configuration ($Fm\bar{3}m$ (International notation), O_h^5 (Schoenflies notation)). In contrast, CdS is known to be allotropic with several possible crystal structures. The most stable and most frequently observed phase is wurtzite ($P63mc, C_{6v}^4$). CdS also crystallizes in two cubic forms, zincblende ($F\bar{4}3m, T_d^2$) and NaCl, although the NaCl lattice is most commonly observed by a polymorphic transformation under a high pressure.[83]

The CdS-PbS alloy system is of particular interest for optoelectronic applications due to its potential for band gap tailoring over a wide range, corresponding to wavelengths from the mid-IR into the visible spectrum. Because both PbS and CdS can exist in the same cubic crystal structure, it is

crystallographically feasible to propose an ideal solid solution across the full range of relative concentrations of Pb and Cd atoms. This theoretical alloy represents a substitutional solid solution consisting of a crystalline phase with compositional homogeneity, meaning Pb and Cd atoms randomly and uniformly dispersed across the cation sites within the lattice. Attainment of the $Cd_xPb_{1-x}S$ solid solution across the whole composition range is hindered by two main inhomogeneity issues: composition and phase.

First, compositional inhomogeneity occurs if the single phase material divides into Pb-rich and Cd-rich regions. Even if non-equilibrium growth conditions are found to produce both PbS and CdS cubic crystal structures, separation into distinct Pb-rich and Cd-rich regions might occur depending on kinetic limitations, in order to reduce the overall Gibbs free energy of the material.

Second, phase inhomogeneity occurs as a result of the various possible crystal structures of CdS. Because CdS is more stable in the hexagonal phase rather than the cubic phase, the alloy material on the Cd-rich side of the phase diagram can exist in the hexagonal phase, while the Pb-rich side remains cubic. In this situation, there is a two-phase transition region in which both hexagonal and cubic phases exist simultaneously. In theory, both phases could even exhibit the same x value, with no compositional inhomogeneity across different regions. But because of the crystal structure distinctions, it is not a uniform solid solution.

A combination of composition and phase segregation are likely to occur simultaneously during alloying within this materials system. The strong

43

miscibility gap and distinct stable phases of PbS and CdS provide a fundamentally challenging system for alloy growth.

Achievements of alloying in the cubic phase beyond the solid solubilities predicted by the phase diagram have been reported and are summarized in Table 2.

Table 2. Summary of room temperature solid solubilities of $Cd_xPb_{1-x}S$ cubic alloys in literature

x	Morphology	Method	Characterization	Reference
0 - 0.25	Bulk	Furnace heating	XRD	84
0 - 0.4	Thin film	MBE	XRD	83
0 - 0.1	Thin film	MBE	TEM	85
0 - 0.18	Thin film	CBD	XRD	86
0 - 0.2	Thin film	CBD	XRD	87
0.05 - 0.25	Thin film	CBD	XRD	88
0 - 0.27	Thin film	CBD	XRD	89
0 - 0.4, 0.8 - 1	Thin film	CBD	XRD	90
0.4 - 0.8	Thin film	CBD	XRD	91,92
0.6 - 1	Thin film	CBD	XRD	93
0 - 1	Powder	High temperature compression	XRD	94

Calawa *et al.* formed solid solutions in bulk crystals with compositions beyond the stable phase boundary limit by heating PbS and CdS sources in sealed quartz ampoules, followed by water quenching. Epitaxial films with compositions up to x = 0.4 were reported on NaCl[83] and up to x = 0.1 on mica substrates by a two-source MBE method. The change in lattice parameter as measured by XRD was

44

found to follow Vegard's law. The linear relationship between lattice parameter and x was described by the following equation:[83]

$$a_0(Cd_xPb_{1-x}S) = 5.938 - 0.375x \text{ (Å)}.$$

Substitution of x = 1 for pure CdS results in a lattice parameter within the range of reported values for CdS with NaCl cubic lattice structure. Sood *et al.* also found that a growth temperature decrease was required to achieve increased cadmium concentrations. Moreover, single crystal growth of the alloy phase was favored over polycrystalline growth with Cd-rich protrusions only for a very narrow temperature range, indicating a sensitive metastable growth process.[83]

Chemical bath deposition (CBD) is the most widely explored method for thin film production of polycrystalline $Cd_xPb_{1-x}S$ films. Most alloying achievements are in the Pb-rich region of the composition spectrum, although some results have been indicated in the Cd-rich region and select values in the center of the composition range between 0.4 and 0.8. Rabinovich *et al.* proposed criticisms of previous CBD work, citing that the wide range of solubilities claimed was not always sufficiently supported by the XRD results.[86] They demonstrated CBD-grown films with x up to 0.18, as determined by detailed XRD and additionally verified by atomic absorption spectroscopy to measure the Cb:Pb ratio in the film. CBD involves a delicate optimization of parameters and does not always support the growth of solid solutions. Reddy *et al.* reported one such attempt that produced $(PbS)_{1-y}(CdS)_y$ two-phase material instead of a $Cd_xPb_{1-x}S$ uniphase ternary alloy.[95] Regardless of the exact Cd compositions within these thin films, the overall results prove that it is possible to maintain the

45

metastable $Cd_xPb_{1-x}S$ cubic alloy in thin films through suitable preparation conditions.

Under high temperature and extreme pressure compression, a mixture of PbS and CdS powders were converted into a $Cd_xPb_{1-x}S$ solid solution.[94] The cubic metastable phase was retained for the entire range of compositions, $0 \leq x \leq 1$, even after the temperature and pressure were returned to ambient conditions. For pure CdS, some hexagonal phase material was detected in addition to the cubic phase.

No literature reports indicate $Cd_xPb_{1-x}S$ alloying in nanowire form. Jang *et al.* performed gas-phase substitution to convert hexagonal CdS nanowires to cubic PbS nanowires.[52] No measureable alloying was detected, although some partial conversion at lower temperatures resulted in separate domains of PbS and CdS material within a single wire. Although the cubic structure of CdS is not the thermodynamically predicted equilibrium crystal structure, Xu *et al.* reported pure CdS nanowires with cubic structure by physical vapor deposition.[96] Selected area diffraction in TEM and imaging of the lattice fringes indicated the cubic structure of the nanowire. This result demonstrates that pure CdS nanowires can maintain the metastable cubic phase under atmospheric pressure growth conditions.

In this chapter, the goal was to create and characterize high-quality $Cd_xPb_{1-x}S$ alloy material in nanowire form by CVD for band-gap tailored applications. Nanowires were achieved with significant alloying in the cubic phase, up to $x = 0.14$ as measured by XRD. The study of growth variables focused on the effect of post-growth cooling treatment on alloy composition and

46

phase segregation morphology. The resulting nanowires were characterized in detail to expand the understanding of the growth and stability of the $Cd_xPb_{1-x}S$ system.

3.1. Growth Procedure

Several CVD configurations were attempted for $Cd_xPb_{1-x}S$ alloy growth. Of all the methods, the simplest (Figure 15) is similar to that of pure PbS growth (Figure 3). A mixture of source powder with a 1:1 molar ratio of PbS and CdS was placed in the center of a one-zone tube furnace (Lindberg/Blue M). One or more substrates with sputtered Au catalyst film were placed horizontally in the temperature gradient region.
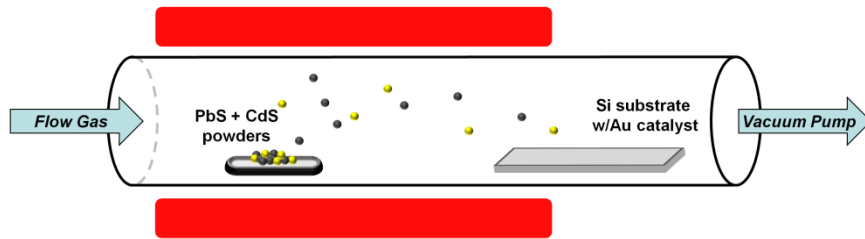
Figure 15. Side view of CVD system for $Cd_xPb_{1-x}S$ alloy growth using mixed source powders.

The main benefit of this setup is that it permitted exploration of a wide range of supersaturation values because multiple substrates, corresponding to a wide range of temperature values, can be included in a single growth experiment.

A more complicated CVD setup utilized a dual port configuration to maintain CdS and PbS source powders in separate source dispersion tubes within the furnace (Figure 16). The inset shows the temperature profile for the one-zone furnace at a typical set temperature of 700°C.
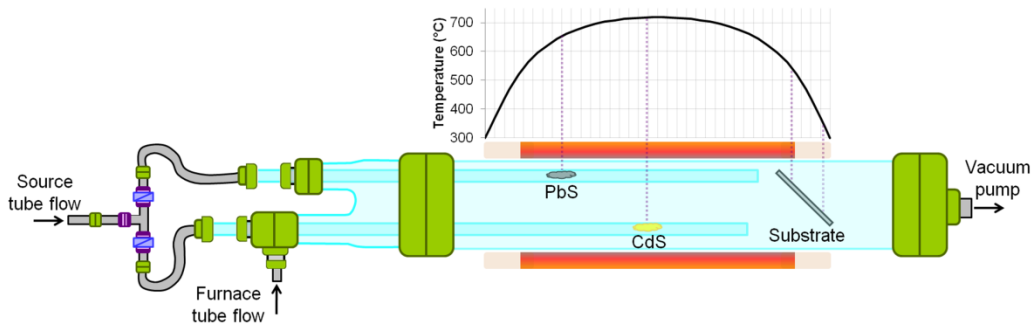
Figure 16. Top view of CVD system for $Cd_xPb_{1-x}S$ alloy growth by the dual gradient method. Inset: temperature profile for one-zone furnace, 700°C set temperature.

Advantageously, this setup allowed individual temperature selection for each source material, as marked by the vertical dashed lines. The source vapors were collimated and directed toward the substrate surface where they were permitted to intermix and form crystal alloy material. Combined with a vertical substrate position at an angle, this setup created two gradients across the substrate, with both source material composition and temperature changing with position. In general, the dual gradient method has demonstrated great potential as a growth strategy to achieve organized composition grading across a substrate surface.[29]

Although a wide range of parameter space was tested, including variations in source and substrate temperature, flow, and pressure, the deposition always appeared non-uniform with irregular deposition density across the substrate surface, including regions of no deposition or textured bulk film. Nanowire growth tended to favor positions near the edges, indicating some sort of preferential edge effects possibly due to temperature or flow. Due to heat loss, the edges of the substrate experience different temperature conditions as compared to

48

the bulk center section. Flow around substrate edges may be subject to complex boundary conditions.

To consider these edge effects, the flow regime of the CVD growth condition is evaluated. The mean free path is defined as the average distance a molecule travels before colliding with another, and is given by the formula:

$$\lambda = \frac{k_b T}{\sqrt{2}\pi d^2 P},$$

where k_b is the Boltzmann constant, T is temperature, d is the molecular diameter, and P is pressure.[97] For a typical set of growth conditions for $Cd_xPb_{1-x}S$ alloy nanowires (T = 700°C, P = 15 Torr, Ar atmosphere), the mean free path is 0.075 mm. The Knudsen number is a dimensionless quality as follows:

$$K_n = \frac{\lambda}{D},$$

where D is the diameter of the tube.[97] A tube diameter of 38 mm results in a Knudsen number less than 0.002, which corresponds to the laminar flow regime. In this regime, the gas velocity is zero along the sidewalls of the tube and transitions smoothly to the maximum at the center of the tube. These boundary conditions could also play an effect as the source vapor flows around the edges of the substrate. Especially for vertical positions, the substrate effectively disrupts the laminar flow paths. Further work is required to understand and optimize the growth conditions to favor nanowire deposition equally over the whole substrate surface.

Of all the growth configurations and parameters, post-growth cooling treatment was identified as the most critical variable for alloy composition and

phase segregation. Figure 17 shows a graph of substrate temperature with time during a standard $Cd_xPb_{1-x}S$ growth procedure. The furnace was heated to the set temperature over a period of 15 minutes, and the temperature was maintained for 30 minutes of growth. Until this step, the conditions were identical for both procedures; thus, the deposition is assumed to be identical as well. After turning off the furnace, the quenched procedure involved immediately translating the quartz tube downstream and simultaneously turning on a high-speed cooling fan directed at the exposed tube surface. The substrate region was surrounded by flowing air that effectively dissipated heat in a rapid manner by increased convection.
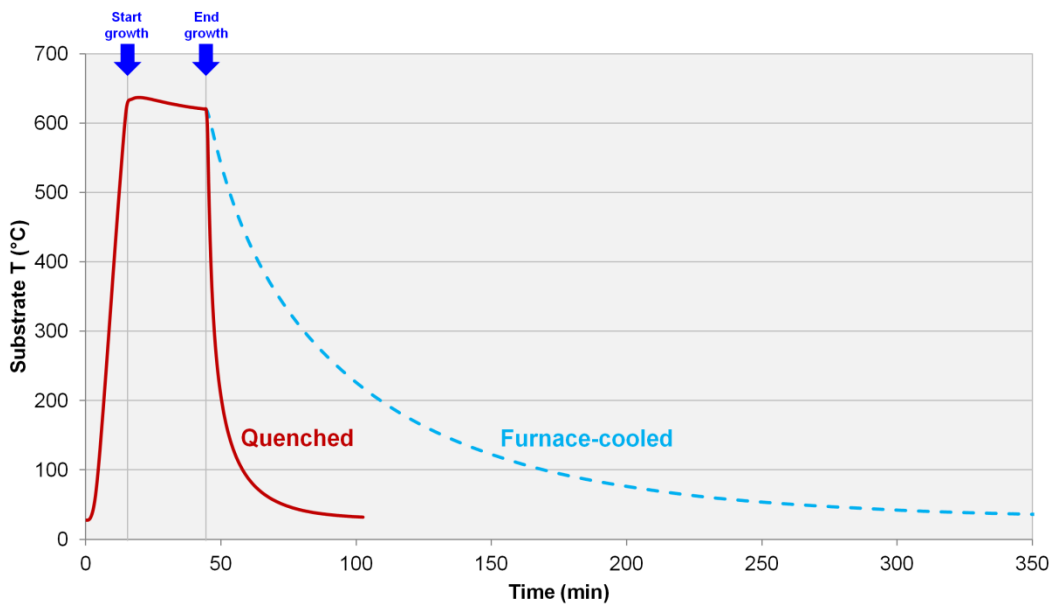
Figure 17. Substrate temperature versus time for post-growth cooling treatments: quenched (red solid line), furnace-cooled (blue dashed line).

As shown in the temperature plot, the cooling rate for quenching immediately after completion of growth was in excess of 120°C per minute. Conversely, the furnace-cooled procedure involved no movement to the furnace tube, permitting

the system to naturally radiate heat and slowly come down to room temperature. The cooling rate immediately after growth was a mere 14°C per minute. The substrate remained at elevated temperatures for over 3 hours as the temperature incrementally decreased over time. The drastic difference in thermal energy experienced by the nanowires in the two post-growth cooling procedures caused definitive effects on phase segregation and composition, as will be discussed.

3.2. Materials Characterization and Discussion

3.2.1. SEM

SEM images of typical morphologies of $Cd_xPb_{1-x}S$ nanostructures are depicted in Figures 18, 19, and 20. The dense nanowires in Figure 18 were imaged in a cross-section perspective near the edge of a sample that was quenched after growth. The round catalyst tips indicate that the nanowires were grown by the VLS mechanism. Figure 18b is of the same region but in BSE imaging mode. As brightness scales with atomic number, the Au-rich catalyst tips appear the brightest as expected because the atomic number of Au is greater than the average atomic number of the $Cd_xPb_{1-x}S$ crystal material. No phase segregation is observed for the quenched sample, as evident by the uniform contrast within each nanowire.
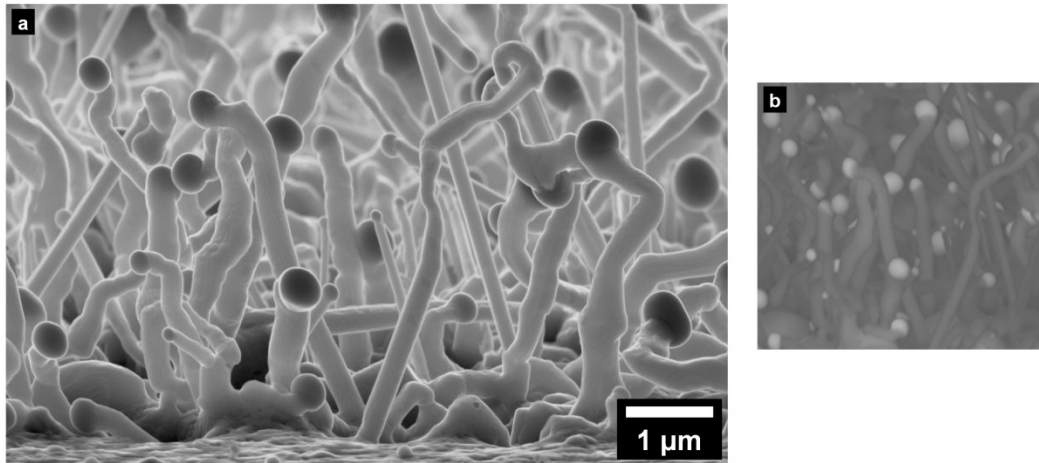
Figure 18. Cross-sectional SEM view of typical quenched $Cd_xPb_{1-x}S$ nanowires: (a) SE mode, (b) BSE mode.

In furnace-cooled samples, phase segregation was observed to occur in both the axial and radial directions. Axial phase segregation created heterojunctions between distinct composition regions along the axis of each tapered nanobelt (Figure 19). Phase segregation in the radial direction appeared in another sample as shown in Figure 20.
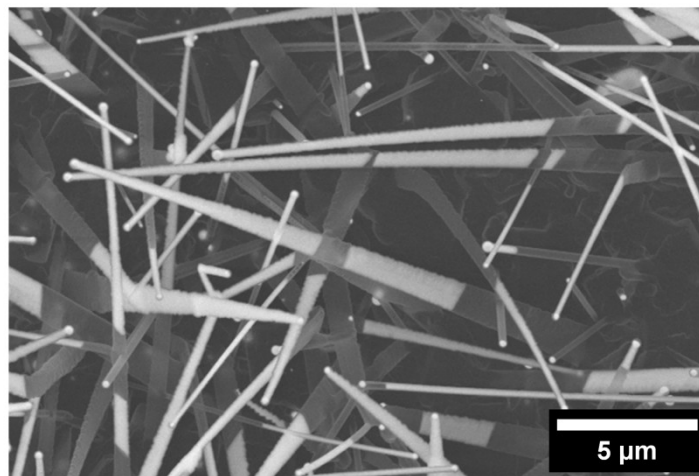
Figure 19. Furnace-cooled $Cd_xPb_{1-x}S$ nanobelts with axial phase segregation.
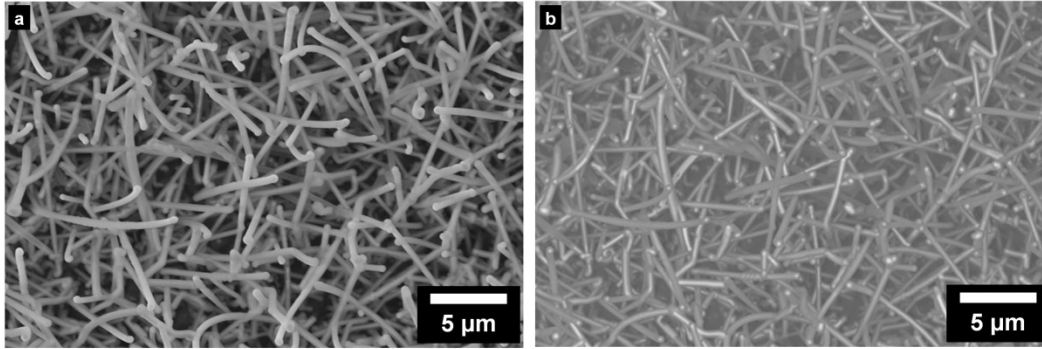
Figure 20. SEM of furnace-cooled $Cd_xPb_{1-x}S$ nanowires: (a) SE mode, (b) BSE mode reveals some nanowires with radial phase segregation (bright core and dark shell).

Although TEM is better suited for internal morphology characterization, the electron beam in SEM characterization contains enough energy to penetrate slightly into the small wires and probe beyond the surface. The corresponding BSE image of Figure 20b clearly shows a contrast distinction between the center and edges of some nanowires, indicating a core-shell type configuration. The nanowire diameters are around 400 nm, while the core diameters are around 150 nm. Additionally, some wires exhibit a contrast change along the length, demonstrating that phase segregation occurs simultaneously in the radial and axial directions. TEM is required for more precise characterization of the internal structure.

3.2.2. TEM

Nanowires from a sample area similar to Figure 20 were dispersed onto a copper TEM grid with lacy carbon support film. Figure 21 contains TEM and dark-field STEM images of a grouping of three nanowires. The sidewalls, especially of the larger nanowire, show some incomplete faceting behavior. In the

dark-field STEM image, where contrast corresponds to atomic mass, there is

clearly non-uniform distribution of material in all of the nanowires.
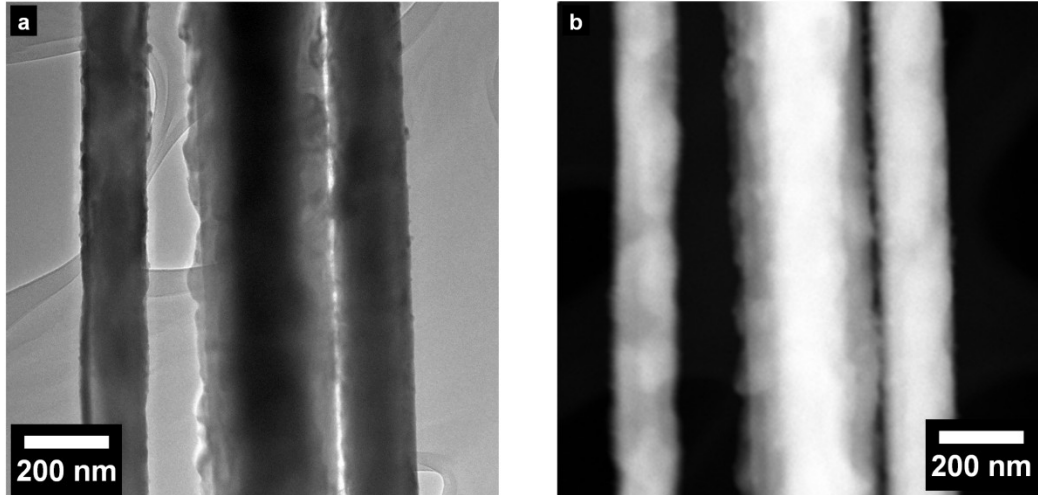
Figure 21. (a) TEM and (b) STEM images of three furnace-cooled $Cd_xPb_{1-x}S$ nanowires.

The large diameter nanowire exhibits distinct contrast strips of equal width on

both sides of the center bright section, consistent with the two-dimensional

projection of a core-shell nanowire heterostructure. The thinner wires did not

show a continuous, central segregation of material, instead exhibiting irregular,

patchy contrast. In order to fully characterize the complex internal configuration

of phases, cross-sectional TEM specimen preparation would be necessary.

Although EDS was attempted for all of the wires imaged in TEM, the results were

inconclusive due to the minimal Pb signal detected. Only a few large area scans

collected any Pb signal above the background noise level. Of the vapor pressures

of the three elemental constituents of the alloy crystal, Pb has the lowest; thus,

during long times at elevated temperatures during furnace-cooling, Pb is not

expected to diffuse out and leave behind a surface depletion layer.[98]

3.2.3. XRD

To determine the metastable alloy composition, XRD was completed on as-grown furnace-cooled and quenched $Cd_xPb_{1-x}S$ samples (Figure 22). The (111) peak was selected for detailed characterization.
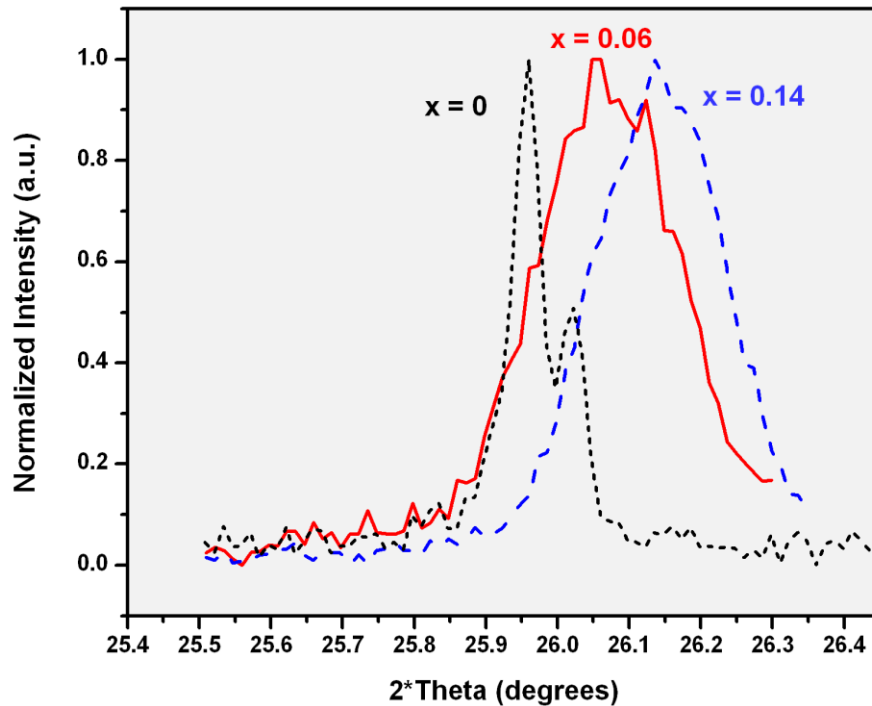
Figure 22. XRD of as-grown $Cd_xPb_{1-x}S$ alloy samples: furnace-cooled (red solid line), quenched (blue dashed line). Pure PbS wires (black dotted line) shown for reference.

Due to the large x-ray beam spot size relative to individual nanowires, the characterization sampled many wires with a range of crystal compositions. Because a range of composition values was probed simultaneously, the peaks corresponding to alloy material were broader than that of a single composition material (see PbS for reference). The K_α doublet cannot be resolved; thus, the copper wavelength used in Bragg's law for calculation of the lattice plane spacing was the weighted average value of $K_{\alpha1}$ and $K_{\alpha2}$ (λ= 1.541874 Å). The lattice plane

spacing was converted into the lattice parameter for the cubic alloy materials. The Cd fraction x was extracted by a linear interpolation of the known NaCl cubic lattice parameters of the two binary endpoints (CdS: JCPDS card no. 03-065-8873, PbS: JCPDS card no. 01-077-0244). Out of all of the furnace-cooled samples measured, the largest detected alloy composition was x = 0.06. For quenched samples, the largest detected alloy composition was x = 0.14. As discussed, it is expected that the quenching procedure prevents or at least severely suppresses the post-growth diffusion that reduces the alloy fraction accomplished during growth. The quenching procedure successfully retains metastable cubic phase alloy material.

3.2.4. Discussion of Composition and Phase Segregation

In the CVD setup of Figure 15, substrates positioned along the entire deposition region effectively sample a wide range of supersaturation values in a single experimental run. Because of the temperature gradient, each substrate is at a distinct temperature with a specific amount of available source vapor. Combining the most favorable growth conditions with a large range of substrates did not improve the composition range achieved. For the given values of supersaturation possible in this CVD system, x = 0.14 is considered to be the maximum value of Cd available in the cubic alloy phase. As suggested from literature, extension of the cubic alloy composition range into more Cd-rich values may only be possible with growth conditions further away from equilibrium, such as high temperature compression to extreme pressures.

The SEM and TEM results support that quenching inhibits phase segregation in the $Cd_xPb_{1-x}S$ alloy nanowires. The results are consistent with the diffusion-controlled mechanism for phase segregation proposed for $Cd_xPb_{1-x}S$ thin films. According to Sood *et al.*, a matrix of dislocations acted as fast pathways for diffusion of material during cooling after growth.[83] Also in regard to direction of phase segregation, it is apparent that axial versus radial segregation depends more on nanowire diameter than on growth conditions because the grouping of wires in TEM were from the same area of a sample. Only the larger diameter wire exhibited obvious core-shell radial segregation, while the thinner nanowires showed irregular, splotchy segregation in the axial direction.

The generation and morphology of compositional inhomogeneity involves a balance of energy. Because Pb-rich and Cd-rich regions exist along the entire length of the nanowire, the core-shell structure requires only short diffusion lengths to reach an enriched region. The trade-off is that a cylinder of interfacial area, with an associated energy cost, is generated along the entire length of the nanowire. This configuration is apparently not favorable for small diameter nanowires or nanobelts, which have higher surface-to-volume ratios. Nanowires with small diameters, and nanobelts with a thin thickness dimension, appear to favor axial segregation. Generally, axial segregation produces less interfacial area than the core-shell type segregation, although Pb and Cd atoms may have to diffuse farther to reach an enriched region. The diameter or thickness of each nanostructure indicates its directional preference for segregating into distinct composition regions while minimizing its overall energy. The phase segregation

effectively creates self-organized heterostructures by a single step growth method, with the useful potential to offer visible and mid-IR emission from the same nanostructure.

3.3. Optical Characterization

Given that CdS and PbS are direct band gap materials, alloys are expected to have interesting optical properties with emission corresponding to band gaps between that of CdS and PbS.

3.3.1. PL

PL characterization of dispersed, furnace-cooled nanowires, similar to those in Figure 20, produced two band edge emission peaks corresponding to Cd-rich and Pb-rich material (Figure 23, red solid lines). The 505 nm peak in the visible spectrum corresponds to pure CdS material. The 2277 nm peak in the mid-IR is significantly shifted from that of pure PbS (shown for reference), indicating an alloy composition between PbS and CdS. Emission from quenched nanowires (dashed blue line) showed a mid-IR peak at 2085 nm, which corresponds to an alloy composition that is more Cd-rich than that of the furnace-cooled sample. Depending on the PL spot position, the visible peak was occasionally detected as well. For quenched samples, it is believed that the Cd-rich emission originates from separate nanostructures, not due to phase segregation within single nanowires, as supported by SEM-BSE imaging.

Comparison of the mid-IR peak widths reveals that the furnace-cooled peak is significantly wider than the quenched peak. The quenched peak exhibits similar width as the single composition pure PbS, indicating uniform, high-quality

crystal material. The peak broadening for the furnace-cooled sample has two

possible contributions. Peak broadening can arise from near-band-edge defect

emission. Also, it is expected that because the slow furnace-cooling permitted

composition segregation, a range of Pb-rich alloys contribute to the light emission

contained within the broad peak.
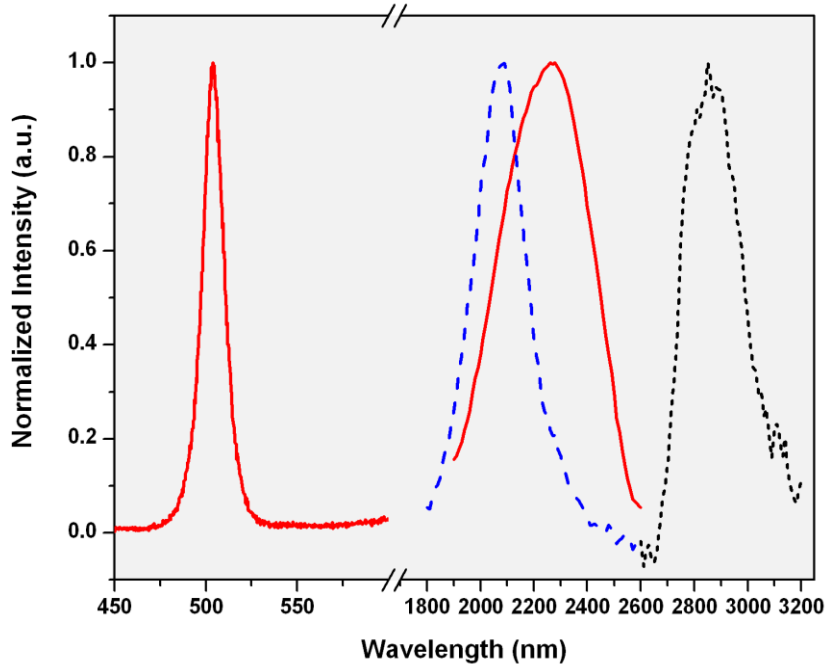
Figure 23. PL emission from furnace-cooled $Cd_xPb_{1-x}S$ nanowires (red solid
lines), quenched nanowires (blue dashed line), and pure PbS wires (black dotted
line).

3.3.2. Band Gap Tailoring with Composition

To consider the effect of band gap tailoring relative to alloy composition,

PL emission peaks were converted into band gap values and plotted against their

corresponding x values as extracted from XRD. Each pair of Cd fraction and band

gap, from pure PbS, furnace-cooled, and quenched nanowires, are plotted in

Figure 24. With limited data points in the Pb-rich end, it is not clear how the band

gap trend continues with increasing x. But for the available data, a simple linear

fit produces a slope around 1.2. The band gap of $Cd_xPb_{1-x}S$ alloy nanowires appears less sensitive to increasing x than previously reported for this alloy system. Literature-reported linear slope values for thin films range from 1.8 to 3.5.[84,85,92,93,99] If linear behavior continues for increasing x, the low slope value established here for the Pb-rich range does not predict the known pure CdS band gap at x = 1.
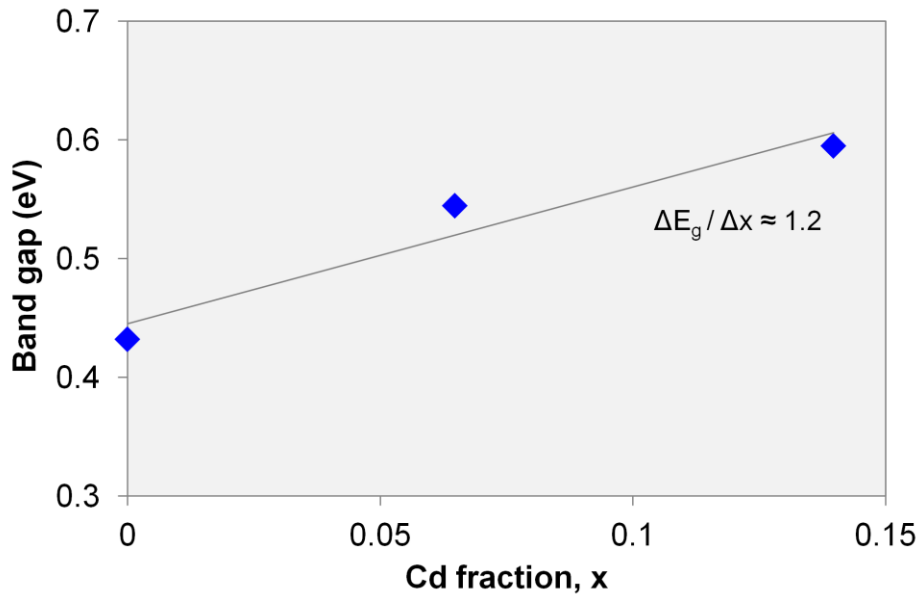
Figure 24. Band gap tailoring by $Cd_xPb_{1-x}S$ alloy composition.

Sood *et al.* proposed that a non-linear variation of band gap with composition is likely, especially due to the complex alloy band structure with conduction band minima and valence band maxima that occur at different symmetry points in k-space, depending on composition.[99] It is also possible that the nanowire morphology itself contributes to the unusual band gap tailoring properties due to the strain relaxation provided, as detailed for nanowires in other chalcogenide alloy materials systems.[100] In general, band gap tailoring with composition permits the selection of the functional wavelength of an optoelectronic device. In

combination with fast and sensitive photoconductive response, lead chalcogenide ternary systems offer properties and band gap ranges useful for IR detection applications.[85]

3.3.3. Individual Nanobelt Characterization

Figure 25 contains the characterization of an individual furnace-cooled $Cd_xPb_{1-x}S$ self-organized axial heterostructure nanobelt. Several distinct composition segments along the length of the nanobelt were indicated by contrast variation in the SEM-BSE image of Figure 25a. Figure 25b and 25c contain the optical microscopy images of the same nanobelt under broadband and UV-illumination, respectively.
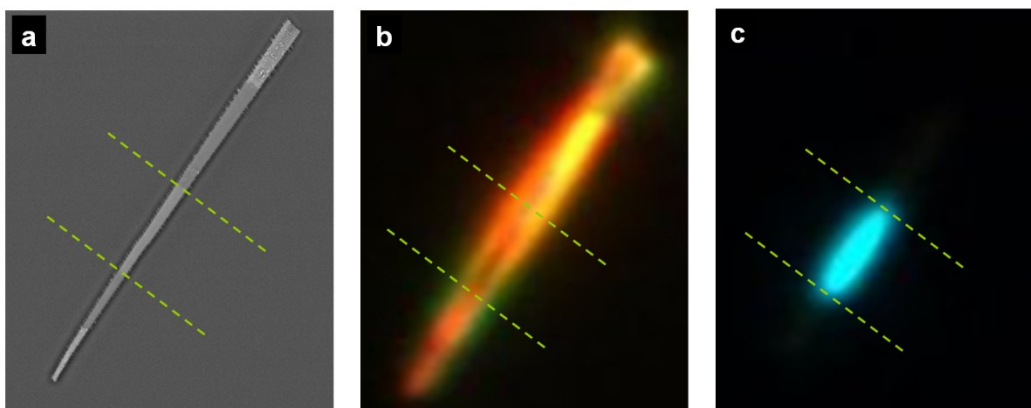
Figure 25. Characterization of an individual $Cd_xPb_{1-x}S$ nanobelt (length = 17 microns). (a) BSE-SEM image revealing contrast segments along the axis length, (b) optical microscopy image under broadband illumination, (c) UV-illuminated PL image with emission corresponding to 505 nm.

One segment of the nanobelt emitted visible light at 505 nm, consistent with pure CdS material. The mid-IR signal from a single nanobelt is too weak to be detected. EDS indicated Pb-rich material near the wide end of the nanostructure, at a Cd:Pb ratio of 1 : 26. This region did not emit visible light and can assume to emit in the mid-IR spectrum, with the specific wavelength dependent on its local

alloy composition. This combination of materials and optical characterization proves that phase segregation generates complex structures within each wire. As also found by TEM, there is a significant amount of wire-to-wire variation, even within the same sample. It is difficult to exactly correlate the bulk measurements from XRD and PL to those of individual wires in TEM and PL imaging.

3.3.4. Temperature-Dependent PL

Another interesting optical effect available for study in the $Cd_xPb_{1-x}S$ materials system is the band gap temperature dependence. As discussed in Section 2.4, the emission from pure PbS is known to blue-shift to shorter wavelengths with increasing temperature due to its unusual negative band gap pressure coefficient. On the other hand, CdS shows the typical semiconductor behavior, with an emission red-shift to longer wavelengths with increasing temperature. Therefore, an alloy between these two materials is expected to show a transition from blue-shift to red-shift behavior at some point along the composition spectrum. The semiconductor alloy crystal at this changeover point shows complete temperature insensitivity; the band edge emission is the same wavelength over all temperatures. Using the known temperature dependences for bulk CdS[101] and PbS[80], the crossover from positive to negative dependence is theoretically calculated to occur around x = 0.6.

The temperature dependence of PL emission from $Cd_xPb_{1-x}S$ nanowires is shown in Figure 26. Two long-wavelength emission peaks were detected from a sample that was furnace cooled. Emission from pure PbS wires (x = 0, see Section 2.1) is also shown for reference. Indicated by the smaller wavelength values, the

emission peaks represented by blue triangles originate from crystal alloy material with larger x than the orange squares. The slope of the larger x material, in terms of change in emission wavelength per change in temperature, is closer to zero. With increasing x from the Pb-rich side of the alloy, it is expected that the $Cd_xPb_{1-x}S$ alloy material exhibits less temperature sensitivity as it approaches the predicted temperature insensitivity composition. Although the data from alloy nanowires demonstrates the expected trend of temperature sensitivity reduction, it occurs at a much faster rate than previously demonstrated in literature.
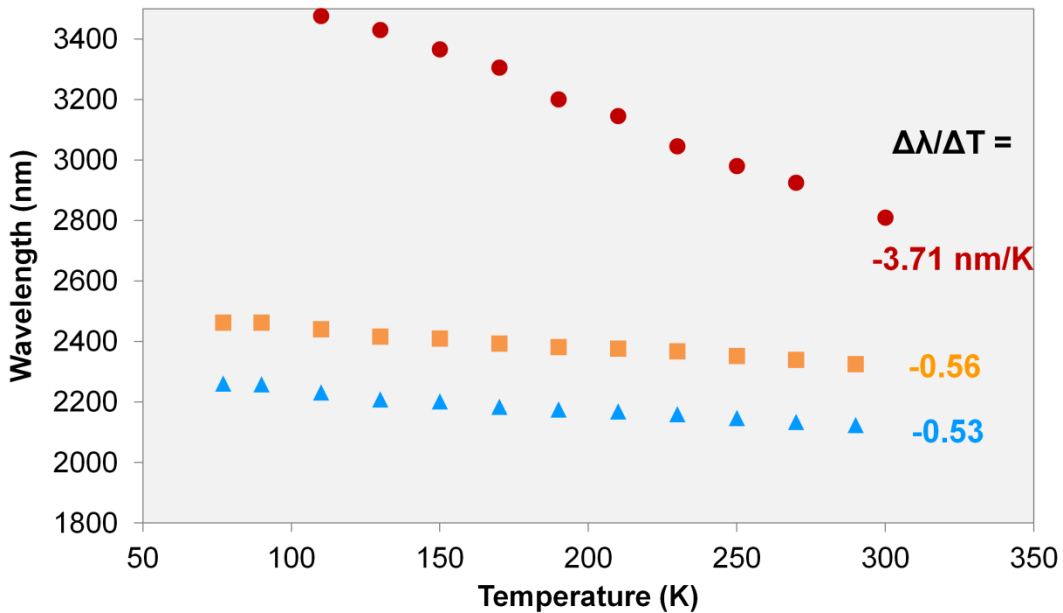
Figure 26. Change in PL emission wavelength with temperature for two $Cd_xPb_{1-x}S$ alloys (orange squares and blue triangles) and pure PbS (red circles).

Zolotov *et al.* reported emission from $Cd_xPb_{1-x}S$ thin films in a similar wavelength range to the data plotted here. They demonstrated that increased Cd content from x = 0.06 to x = 0.08 produced a corresponding decrease in temperature sensitivity from -2.21 nm/K to -1.75 nm/K.[102] The slope values observed for the nanowire alloys of this chapter (-0.56 nm/K and -0.53 nm/K) are

much closer to zero than for the reported thin films; thus, the alloy material shows significantly reduced temperature sensitivity. Based on this comparison, perhaps a temperature insensitive $Cd_xPb_{1-x}S$ alloy nanowire material exists with a much smaller x than the predicted value of 0.6. Because the ability to retain metastable phases is plagued by increasing thermodynamic instabilities with increasing x, a material with smaller x is more easily achieved. A material with temperature-independent emission and absorption is useful in devices that experience extreme temperature conditions and require stable optical performance. Possibly, the observed temperature insensitivity has contributions from near-band-edge defect emission that influences the measured peak positions. Determining the precise origin of the decreased temperature sensitivity requires further optical characterization.

3.4. Device Application: Solar Cell

In general, $Cd_xPb_{1-x}S$ alloys are of interest for solar cells because the band gap tailoring property permits selection of a favorable band gap for a single cell solar device.[88,90-92,95] According to the Shockley-Queisser limit, the maximum theoretical efficiency of a solar cell using a single band gap p-n junction is only around 30%.[103] Significant intrinsic losses arise because the single band gap of the solar cell is not properly matched to the broad solar spectrum. Incoming photons with energies greater than the band gap are subject to energy loss by thermalization of hot carriers; low energy photons are wasted by transmission through the active material.[104] In order to increase the efficiency of a photovoltaic solar cell device, multiple band gaps are required to minimize thermalization and

transmission losses. Although multi-junction solar cells in a stacked design provide multiple band gaps, the crystal growth involves careful lattice matching, which drastically limits the selection of possible materials. Laterally arranged subcells provide an alternative to stacked multi-junction cell designs.

The nanowire alloy growth work completed in this chapter was originally motivated by the potential applications in broad-spectrum solar cells. The band gaps of the $Cd_xPb_{1-x}S$ alloy correspond well to the solar spectrum of sunlight, ranging from the mid-IR into the visible spectrum. The nanowire morphology permits growth of a wide range of compositions on a single substrate without lattice mismatch concerns. In conjunction with the growth experiments, efforts within the C. Z. Ning research group were made to design a proposed solar cell device with $Cd_xPb_{1-x}S$ alloys as the active, light-absorbing material, as pictured in Figure 27. With this configuration, a dispersive concentrator is necessary to split the incoming broadband sunlight into its distinct spectral components, and then concentrate and direct the light to its associated band gap subcell. Detailed device simulations predicted an impressive efficiency of 42% under 240 sun illumination.[105] Work is ongoing to overcome the fabrication challenges associated with the nanowire solar device design.
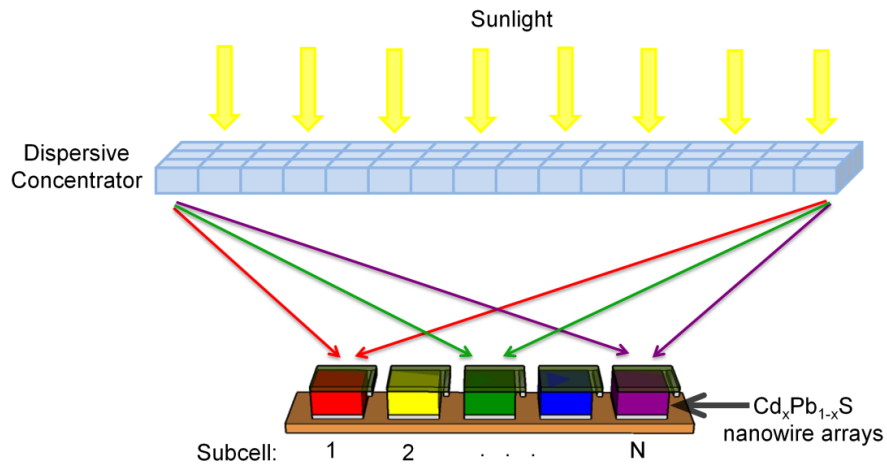
Figure 27. Schematic representation of $Cd_xPb_{1-x}S$ laterally arranged solar cell. Adapted from Caselli and Ning.[105]

3.5. Summary

The experiments of this chapter have demonstrated the growth of $Cd_xPb_{1-x}S$ alloy nanowires with compositions well into the metastable regime, up to x = 0.14 as verified by XRD. Consistent with predictions from the equilibrium phase diagram, significant alloying was achieved on the Pb-rich side, while the resulting Cd-rich hexagonal phase remained essentially pure. Elemental analysis by EDS has not yet confirmed the compositions of alloy materials, possibly due to significant variation between individual nanowires. Both furnace-cooled and quenching post-growth procedures were explored as variables of the growth procedure. Quenching was essential to maintain high x values in the metastable cubic phase. The furnace-cooled procedure permitted phase segregation to occur by diffusion, which generated Cd-rich and Pb-rich composition regions. These self-organized heterostructures were conveniently created through a single-step CVD growth process. Further experimentation is required to discover growth

parameters of a single experiment that generates composition grading in an

orderly fashion across the width of the substrate.

Chapter 4

CONTACT PRINTING OF CdS$_x$Se$_{1-x}$ NANOWIRES

Growing nanowires of varying compositions on a single substrate is a practical way to achieve a range of band gaps in a small spatial area. In general, alloying between two direct band gap semiconductors creates semiconductor material with intermediate values of band gap. Conventional epitaxial thin film growth techniques can only support the growth of a narrow range of compositions due to lattice mismatch between the film and substrate. However, growth of single crystal nanowires non-epitaxially on an arbitrary substrate eliminates the composition restrictions of thin film growth, and thus provides opportunity for unique optoelectronic devices with variable band gaps.

CdS$_x$Se$_{1-x}$ nanowires have been previously grown across the entire composition range on a single substrate.[106] Such a wide range of bandgaps in a narrow spatial range is very useful for many optoelectronic applications including chemical or biological sensing, photodetectors, solid-state lighting, solar cells, microdisplays, tunable light emitting diodes and lasers. Due to the random orientation of nanowires during growth, subsequent organization of the nanowires is required to actually construct an optoelectronic device. The aim of these investigations was to optimize CdS$_x$Se$_{1-x}$ growth parameters to meet the morphology and length requirements for contact printing device processing. Many growth variables were investigated, but the critical parameters identified during this optimization were source and substrate temperature, pressure during heat-up and growth, and flow rate. Ultimately, these factors served to unify the gas-phase

68

supersaturation over the substrate for both CdS and CdSe. This work represents an important push toward achieving complete device potential by exploiting the benefits that CdS_xSe_{1-x} nanostructured materials offer to the field of optoelectronics. The optimized CdSSe nanowires enabled the demonstration of a wavelength-variable photodetector device that covers a wide portion of the visible spectrum.[107]

4.1. Introduction to Contact Printing

Contact printing has been demonstrated as a successful technique for the direct transfer of nanowires from an original growth substrate to a new device substrate.[108-112] The basic process involves the directional sliding of the as-grown nanowire substrate on top of a receiver substrate. The nanowires are effectively combed by the shear force, aligning to the sliding direction while detaching from the original substrate and transferring to the receiver substrate. The assembly process creates ordered arrays of nanowires. It requires no elevated temperatures, allowing for compatibility with diverse substrate materials including plastics and papers.[113]

The surface force between the nanowires and the receiver substrate is the critical interaction that controls the transfer process. The chemical binding interactions or van der Waals forces between the wires and the receiver surface need to be significant enough to disturb the wires from their original nucleation sites.[109] The surface chemistry of the nanowire to be transferred is a fundamental property of its specific material composition. Surface chemical modification, for example, by application of siloxane monolayers or polymer thin films, can be

performed to optimize the interaction forces.[109] Additional variables for optimization include the amount of applied pressure between substrates, velocity of sliding, and use of lubricant. Lubricant forms a spacing layer between the two substrates and minimizes the nanowire-nanowire friction during the sliding process. Use of lubricant has been found to improve the overall alignment of transferred nanowires and to decrease the uncontrolled breakage and detachment of nanowires during the sliding process.[109]

Contact printing of a compositionally graded sample, as compared to a single-composition sample, introduces material and morphology complexities that significantly affect the printing process. First, different materials have inherently distinct surface chemistry characteristics, such that different regions of the graded sample could transfer with varying densities onto the receiver substrate. Second, the morphology of the nanostructures can vary across the sample due to the intentional temperature and source material gradients during growth, which are necessary to generate the desired composition grading. Specifically, CdS and CdSe demonstrate distinct preferred morphologies during growth. In the growth regime investigated for these samples, CdS tends to form long, parallel-sidewall wires for a large region of parameter space. Conversely, CdSe grown in the CVD system of this and previous work tends to form nanobelts, even for minimal deposition rates.[29,106] The desire for compositionally graded CdS_xSe_{1-x} nanostructures with uniform morphology across the whole range has lead to a more detailed study of CdSe growth characteristics, specifically the contributions of VLS and VS deposition.

70

4.2. Growth Characteristics of CdSe

As discussed for PbS growth in Section 2.2.3, the gas-phase supersaturation in CVD growth describes the driving force for source material to leave the vapor phase to form solid phase crystal material. Higher supersaturations tend to favor polycrystalline or bulk-like deposition by the VS growth mechanism. Lower supersaturations combined with appropriate catalyst conditions can promote VLS nanowire growth. The final morphologies observed on a sample are very sensitive to many growth variables. Identifying and understanding the essential variables is crucial to designing nanostructures with appropriate morphologies for devices.

Within a single substrate, it is not expected to observe perfectly uniform nanostructure morphology or sizes, due to several factors. Upon heating, the catalyst film becomes liquid and breaks into droplets. The droplets will naturally have a size distribution that is further intensified by Ostwald ripening. With increased annealing or hold time at high temperature prior to growth, the larger liquid metal droplets will increase in volume at the expense of the smaller shrinking droplets.[114] Additionally, the deposition rate has contributions from multiple growth modes including VS and VLS, which are sensitive to local fluctuations in temperature and availability of source material. To quantify nanostructure morphology and size, it is necessary to collect data from a representative area of the sample and average or generate a distribution of the possible sizes and morphologies.

4.2.1. Quantitative Stereology Analysis of Nanostructures

All of the nanostructures in this work nucleate and grow in random directions with no orientation relationship to the substrate. SEM of nanostructures are typically performed on the as-grown sample in a top-down orientation (beam direction parallel to substrate normal). This imaging condition creates a two-dimensional projection of three-dimensional structures. It is important to consider the errors introduced by performing measurements on projected images. Because of the random orientations, the measured projected length will underestimate the actual nanostructure length. Similarly, the nanostructures could be rotated with respect to the radial direction, resulting in underestimation of the sidewall angle. This is critical for tapered nanobelts with non-radially symmetric shapes. In contrast, pure nanowire shapes with parallel sidewalls would not be affected. For high nanostructure densities, the length may be additionally underestimated because the connection to the substrate is obscured by other structures. Processing techniques to alter the as-grown sample for improved measurement accuracy can be considered. Each, however, has its own merits and sources of error.

Alternative processing techniques for imaging include as-grown cross-sectional SEM or dispersion of nanostructures. Cross-sectional viewing requires that the as-grown sample is cleaved to expose a facet through the deposition region. This destructive process disrupts the original characteristic nanostructure distribution. Similarly, any dispersion method, including stamp printing, mechanical abrasion, or sonication, can introduce uncontrolled errors to the characteristic nanostructure size and morphology distribution.

Stamp printing dispersion involves touching a receiver substrate flat against the growth substrate. This method preferentially collects the longest nanostructures that extend the farthest from the substrate surface. Length breakage is also a concern as the nanostructures fracture at some unknown distance from the nucleation base.

Mechanical abrasion consists of scraping a razor blade or tweezers across the growth substrate surface and collecting the debris on a receiver substrate. With this method, both long and short nanostructures are collected, in addition to any film-like undergrowth layer deposited by the VS mechanism, which can complicate the interpretation of dispersed structures. Length breakage is also a potentially significant effect.

Sonicating the as-grown substrate in alcohol involves no direct contact to the nanostructures, but breakage can occur during or after the structures are agitated from the surface. Drops of alcohol containing the suspended nanostructures are then pipetted onto a clean substrate repeatedly and allowed to evaporate until the desired nanostructure density is achieved. For some materials this method is ineffective at removing large nanostructures if they are too strongly bound to the growth substrate surface.

In general, dispersed nanostructures have less geometrical projection error because they tend to lay flat on the receiver substrate surface. Also the flat distribution permits high-resolution imaging of all edges within a narrow depth of field. On the other hand, as-grown nanostructures require a large depth of field due to the large thickness distance over which the structures exist, and inevitably,

some edges will be blurred depending on the deviation from optimum focus length.

Each dispersion method exhibits preferential removal or destructive characteristics that would modify the original morphology and size distribution of the as-grown sample. The characterization of CdSe aims to compare samples grown over a wide range of growth rates with very different nanostructure lengths and densities, such that no single dispersion method would be appropriate for all samples. As-grown top-down SEM is the most comparable method for unbiased morphology measurements. The projection errors from the random orientation should be equivalent and affect all samples equally.

Nanostructure size and morphology were characterized through a statistical analysis of 50 nanostructures per sample. Measured parameters were the tip width (T), base width (B), and length (L). The tip width is defined as the diameter of the nanostructure at the intersection of the nanostructure with the metal catalyst droplet, base width as the diameter of the nanostructure at the intersection with the substrate, and length as the distance between base width and tip width. These measurements were performed only on samples with low nanostructure density such that the nucleation site on the substrate surface was visible to allow for an accurate assessment of length and base width. From these three parameters, the sidewall angle was calculated by the following equation:

$$\theta = \tan^{-1}\left(\frac{(B-T)}{2}\bigg/L\right).$$

The aspect ratio was defined by the length divided by average diameter:

$$AR = L \Big/ \frac{(B+T)}{2}.$$

As previously described, measured lengths are potentially underestimated; thus, the aspect ratios are subject to underestimation as well. Overall, the values should be reasonably comparable between samples.

The mean intercept length is a useful parameter to quantitatively describe nanostructure size for comparison between samples with high nanostructure density. Although not a direct measurement of nanostructure length or size, mean intercept length is an unbiased and well-established measurement technique for the characterization of many types of structures including grains, particles and voids. The mean intercept length is defined by:

$$L_3 = l \big/ p,$$

where l is the total test line length and p is the number of nanostructure intersections.[115] In the SEM two-dimensional projection of high density nanostructures, the nanobelt density is high enough such that there is no substrate area visible between the belts, and they can be considered to be space-filling along the test lines. The mean intercept lengths presented in the following section were collected by placing circular grid patterns on each SEM image and counting the number of intercepts between nanobelts. This method is an appropriate alternative for quantification of high density nanostructures with obscured lengths and base widths, without requiring removal from the substrate.

4.2.2. CdSe Growth

Generally in CVD growth, very low supersaturation favors epitaxial growth of perfect crystals; moderately low supersaturation favors nanowires; intermediate supersaturation promotes nanobelts or dendrites; and high supersaturation facilitates nanosheets, polycrystalline films, or textured bulk deposition.[74,116] Specifically, CdSe nanostructure growth is known to be rich with diverse morphologies of nanostructures.[117] For the CVD setup and growth regime characterized here, the liquid-catalyzed nanostructures exhibit sidewall angles greater than zero. Over a wide range of supersaturation values down to minimally detectable deposition, VS growth still contributed significantly to the overall growth process, as will be supported by the following nanostructure growth, characterization, and analysis.

CdS_xSe_{1-x} and pure CdSe nanostructures were grown in a one-zone horizontal tube furnace CVD system. The temperature gradient of this system is very different from the three-zone system utilized for the growth of PbS in Chapter 2. In the three-zone system, ceramic fiber insulation (Kaowool) isolated the two heating zones from each other (Figure 28, left). The source was placed in the upstream high temperature zone, and the substrate was placed immediately downstream from the sharp temperature gradient in the low temperature zone. The temperature of each zone was controlled independently, with a possible difference in temperature up to ~ 250°C.

Three-zone furnace   **One-zone furnace**
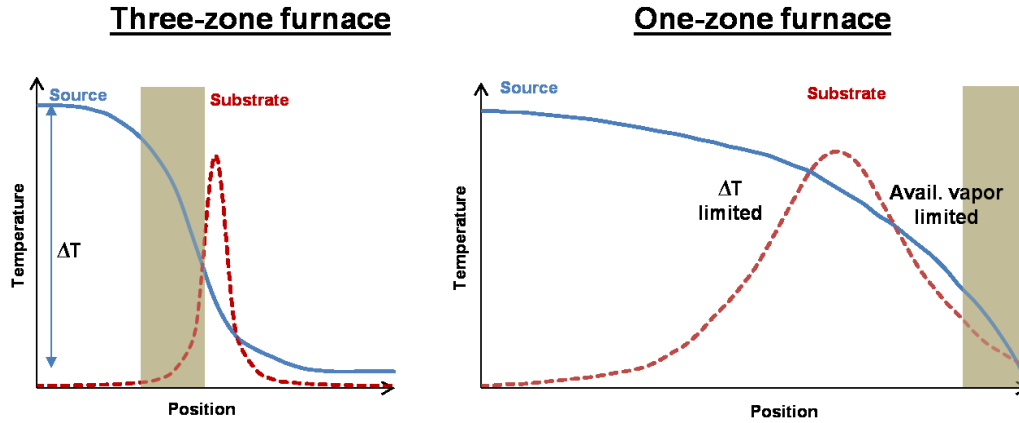
Figure 28. Schematic representation of temperature (blue solid line) and supersaturation (red dashed line) relative to position. The shaded rectangle in the three-zone setup represents the ceramic insulation between two heating zones for the three-zone furnace, and the insulation region at the exit of the furnace for the one-zone furnace.

The temperature difference between source and substrate, ΔT, is directly related to the gas-phase supersaturation. Supersaturation plotted with substrate position can be visualized as sharp peak. The proposed shape of the supersaturation curve is further supported by the very narrow region of visible deposition along the tube wall after growth. The resulting growth morphology has a step-function dependence on position. If the substrate is placed within the high supersaturation zone, then deposition occurs on its surface. If it is placed beyond the high supersaturation zone, then no deposition appears. During growth optimization in this setup, the substrate position is generally held constant while the magnitude of ΔT is used to adjust the peak value of supersaturation.

Conversely, the temperature profile in the one-zone furnace is a smooth gradient that slowly transitions from the source temperature incrementally through each lower temperature to eventually reach the substrate temperature.

Changing the source temperature alters the whole profile, including the temperatures and supersaturations in the substrate position region.

At the front end of the deposition zone, supersaturation can be controlled by ΔT as in the case of the three-zone furnace. As ΔT increases further downstream, supersaturation does not continue to increase. The source material originally present in the gas phase slowly condenses out, apparent as a long region of solid deposition along the tube sidewalls. In this region, supersaturation becomes limited by the available amount of source material. Describing supersaturation in the one-zone furnace is more complex than in the three-zone furance because it strongly depends on both ΔT and substrate position. For optimization, both furnace set temperature and substrate position cause dramatic changes in supersaturation, thus morphology.

The supersaturation curves plotted in Figure 28 are for growth conditions with low carrier gas flow rates. The effect of increasing carrier gas velocity is to increase forced diffusion downstream driven by carrier gas flow, rather than molecular diffusion driven by a concentration gradient. For fast carrier gas velocities, the supersaturation profile is generally flattened out, with a more constant value over a larger distance along the tube axis.[74]

Figure 29 contains SEM images of pure CdSe nanostructures grown at various substrate positions with a constant source temperature of 900°C. Visually, it is apparent that the features are quite large and dense, and decrease in size with decreasing substrate temperature. The size reduction is confirmed quantitatively by the decrease in mean intercept length, from 530 to 440 to 298 nm. Decreasing

nanostructure size confirms that these substrate positions are on the downstream

side of the supersaturation maximum in the one-zone furnace plot of Figure 28.
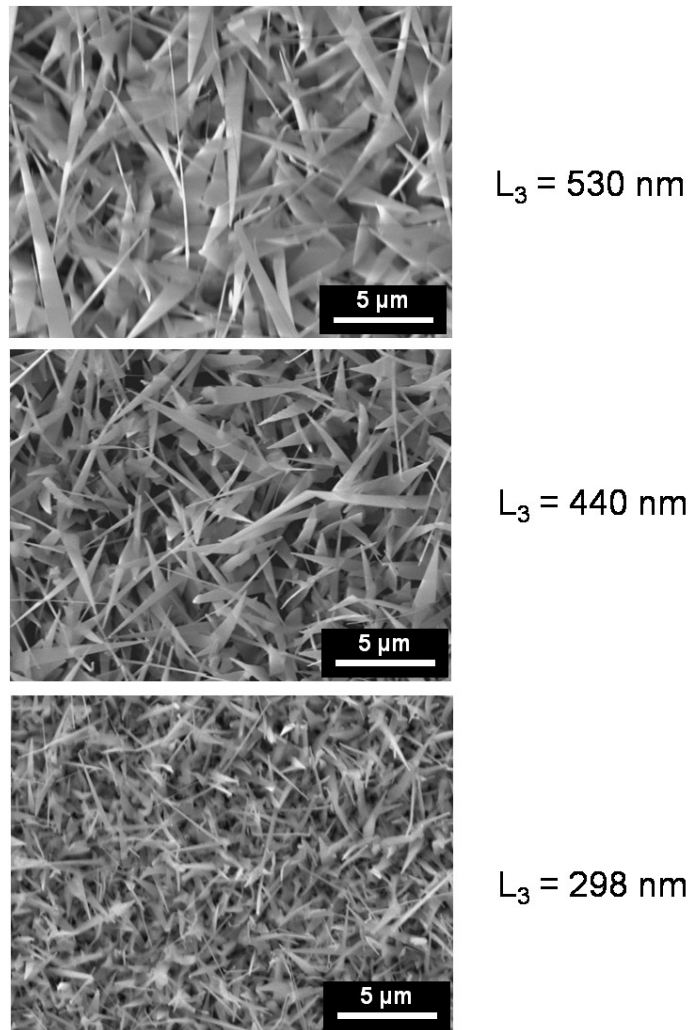
Figure 29. CdSe nanostructures grown in one-zone furnace with decreasing substrate temperatures from top to bottom. Mean intercept length L_3 decreases with temperature.

According to the general supersaturation trend, further decrease of supersaturation

should lead to a favorable regime for nanowire growth. However, this was not the

trend observed. Extending the supersaturation even closer toward zero results in

the CdSe nanostructures of Figure 30. From top to bottom, the supersaturation

during each growth run was gradually decreased to the point of minimally

detectable deposition. The low nanostructure densities allow for direct measurement and evaluation of the sidewall angle, length, and aspect ratio. The minimum projected length average is only 165 nm with an aspect ratio of 2, which represents barely any deposition. According to the histogram plots, sidewall angles greater than zero make up a significant fraction of apparent nanostructures at all values of supersaturation of CdSe. Decreasing supersaturation from the maximum (Figure 29, top) through to the minimum (Figure 30, bottom) does not provide a regime for complete one-dimensional growth. Even the smallest nanostructures still show belt-like character as indicated by the non-zero sidewall angles.

Sidewall angle is an indicator of the relative VLS and VS deposition rates. If the nanostructure is grown entirely by VLS, all of the vapor is accommodated by the liquid particle. Nucleation on any surface other than the nanostructure/catalyst interface is suppressed.[23] Assuming constant liquid catalyst droplet size, the sidewalls will be parallel with a sidewall angle equal to zero. Unlike PbS growth of Chapter 2 in which spontaneously generated catalyst plays a crucial role to observed diameter, this growth regime shows no distinguishable difference for growth in N_2 atmosphere compared to Ar/H_2, indicating no significant contribution of spontaneously generated catalyst by decomposition of binary sources or CdSe/H_2 reduction reaction. All of the measured features exhibit a round Au catalyst tip. This indicates that VLS makes at least some contribution to the deposition rate for all the resulting nanostructures.
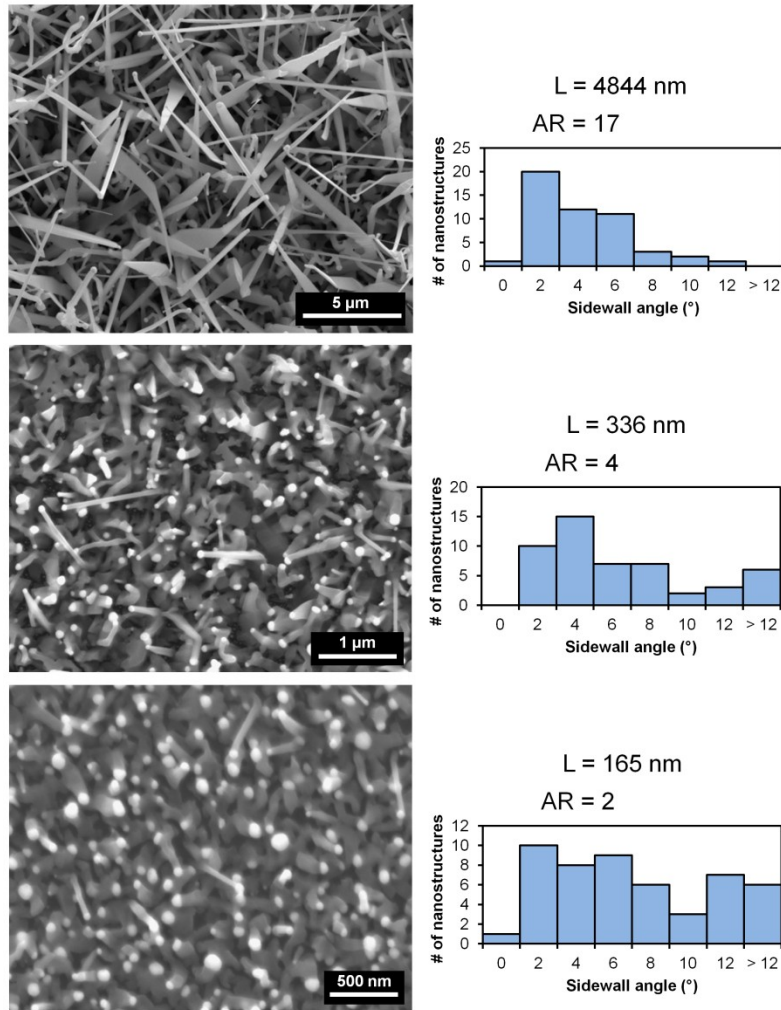
Figure 30. CdSe nanostructures grown in one-zone furnace with decreased supersaturation values from top to bottom. Average projected lengths (L) and aspect ratios (AR) as listed. The histograms of sidewall angles show prominent high-angle belt-like character at all supersaturations.

Generally for high supersaturation, not all of the incoming vapor species can be accommodated by the liquid droplet. The accommodation coefficient is defined as the fraction of the arriving growth species that are actually incorporated into the new phase, not desorbed or diffused away.[25] The accommodation coefficient for the liquid catalyst droplet is dependent on the concentration of source material in the solution. If the concentration of source material in the catalyst is very high, the chemical potential of the source material

in the liquid phase could exceed the chemical potential in the vapor phase, thus eliminating the driving force for preferential accommodation into the liquid.[25] This situation arises if the precipitation of crystal at the bottom of the droplet cannot keep up with the arrival of vapor attempting to incorporate into the droplet. The vapor molecules will instead incorporate elsewhere, nucleating new crystal growth *via* the VS mechanism. This is especially likely to occur on the recently grown nanostructure crystal immediately below the catalyst droplet. The newly formed surfaces may still be in a high energy state, and incoming molecules can incorporate there easily during the restructuring stage.[27] Any point along the sidewall can experience VS layer-by-layer epitaxial growth if the adsorbed atoms have enough thermal energy and surface mobility to reach their lowest energy configurations.[118] The tapered nanobelt morphology is a result of the VS sidewall incorporation process occurring continuously throughout growth. The base is wider than the tip because that area was grown initially, and thus experiences more time overall in the vapor atmosphere, accumulating more deposition on the sidewalls. Tapered belt-like nanostructures show a sidewall angle greater than zero.

In regard to optimization of CdS_xSe_{1-x} nanostructure growth for contact printing, this analysis indicates that no growth regime exists that perfectly favors CdSe nanowire morphology in the wide range of parameter space studied. In conjunction with VLS growth, VS growth contributes to the overall deposition rate even at low supersaturations. The supersaturation threshold above which VS growth dominates is lower for CdSe than for CdS. The optimization needs to

82

balance considerations for the total desired length with minimized sidewall angle to provide the most effective nanostructure morphology and size for successful contact printing.

4.3. Optimization of CdS$_x$Se$_{1-x}$ Growth

The growth parameters of selected procedures along the optimization process are presented in Table 3.

Table 3. Growth parameters of selected CdS$_x$Se$_{1-x}$ growth experiments along the optimization process

| Sample | Temperature (°C) | | | Nominal Pressure (Torr) | | Growth Time (min) | Flow Rate (sccm) | Flow Gas |
	CdS Source	CdSe Source	Substrate	Heating	Growth			
A	900	900	539	15	15	30	50	Ar, 5% H$_2$
B	900	774	522 - 490	15	15	30	50	Ar, 5% H$_2$
C	700	596	521	> 300	15	30	50	Ar, 5% H$_2$
D	700	580	521-515	> 300	5	30	100	Ar, 5% H$_2$

The starting point for the optimization of CdS$_x$Se$_{1-x}$ growth for contact printing was adapted from previously established growth procedures for a similar experimental setup.[106] In order to establish a composition gradient, the cited work used only a temperature gradient across the substrate and a mixture of binary source powders. The growth procedure of Sample A is comparable in that the two binary source powders were both maintained at the same temperature during growth. It differs in that it made use of source dispersion tubes to generate a source material gradient across the substrate surface, as first established for InGaN growth.[15] The two source vapors were isolated from each other until arriving at the substrate surface where they were permitted to intermix. The substrate was assumed to have a constant temperature due to its vertical position

83

perpendicular to the tube axis. Eventually, the two possible gradients across the substrate, source material and temperature, are combined to provide maximum control over the morphology and composition of the growing nanostructures.[29] The initial optimization process considers the source material variables separately before adding the complexities of substrate temperature gradient.

SEM images of Sample A shown in Figure 31 show straight, dense, and very long CdS nanowires. On the contrary, the Se-rich deposition formed tapered nanobelts with much shorter lengths. The center alloy region exhibits nanowires that are shorter than pure CdS with significant kinking along the wire length. PL spectra across the as-grown substrate in Figure 32 shows strong band edge emission ranging from around 520 nm to 690 nm. The composition gradient across the substrate successfully covers a large portion of the visible spectrum.
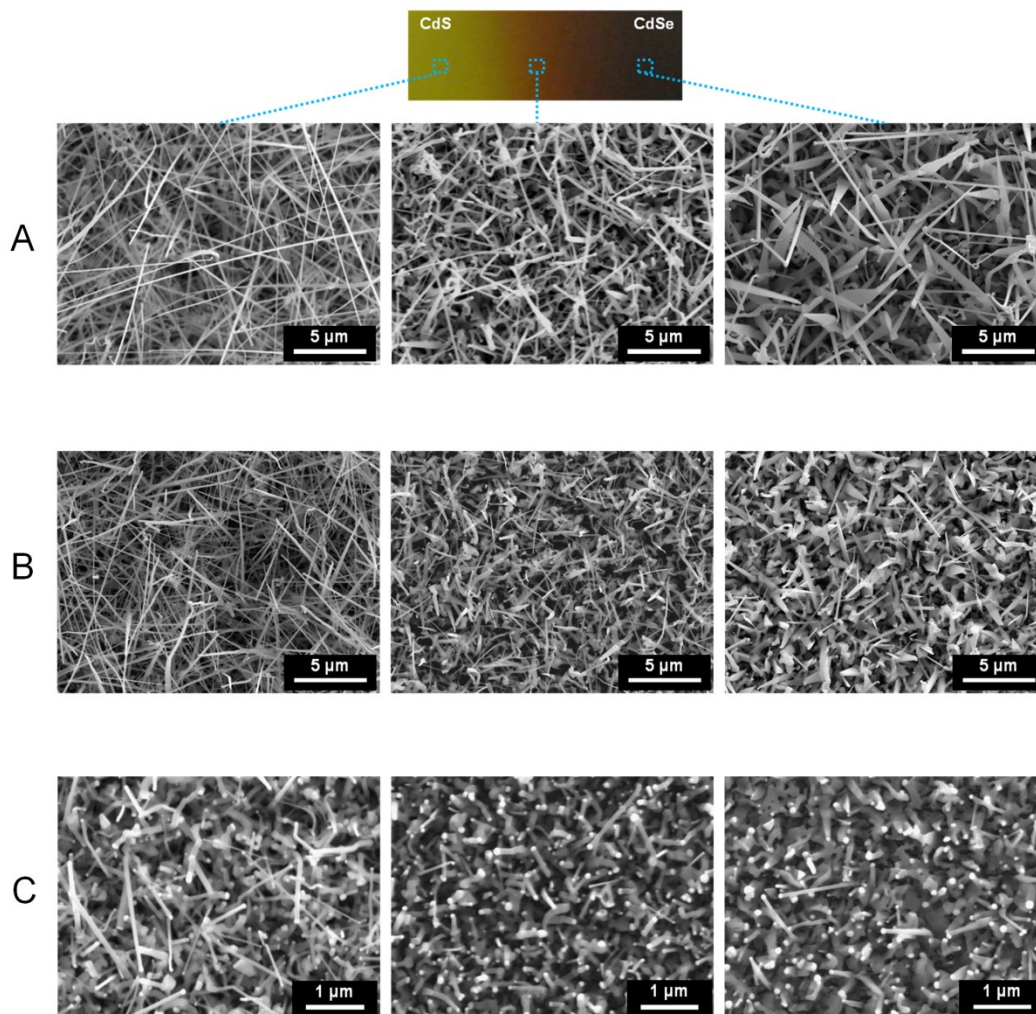
Figure 31. SEM images of the S-rich, center and Se-rich regions of CdSSe graded samples, left to right. Top, representative photograph of graded region of as-grown sample with length of 1 cm. Note the higher magnification of Sample C.
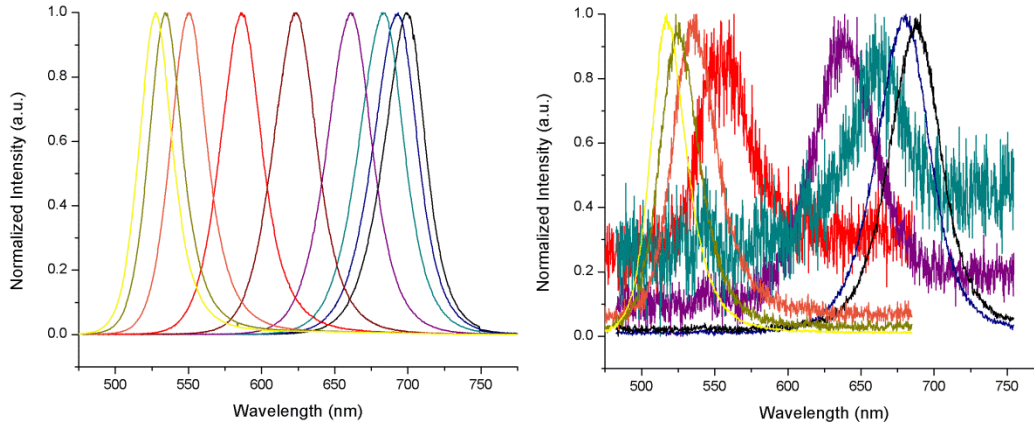
Figure 32. PL spectra from across the CdS$_x$Se$_{1-x}$ graded sample. As-grown (left). After contact printing (right).

Figure 33 shows SEM images of the first attempt of directional contact printing by collaborators in the Javey Research Group at University of California, Berkeley. In the S-rich region, CdS nanowires did not significantly adhere to the receiver substrate, even though they were of the appropriate morphology with long length, parallel sidewalls, and straight growth direction. This result implies that the contact printing variables required optimization as described previously in the introduction. In the Se-rich region, the nanostructures show a better sticking fraction but without much alignment in the direction of the sliding direction. The tapered nanobelt morphology was found to be non-ideal for contact printing. In the center alloy region, there was no transfer during the contact printing process. This region required improvement in both growth and contact printing aspects of the process.

Despite the poor printing quality, the PL spectra of the contact printed nanowires (Figure 32) can be correlated to the as-grown optical results. The overall range of wavelengths is the same from around 520 nm to 690 nm. Due to the low transferred density, the signal is much weaker for the contact printed

sample. The signal-to-noise ratio decreases dramatically for curves approaching

the mid-alloy range. The PL signal from the center section was completely

indistinguishable from the background noise due to lack of nanostructure

material. The comparison of optical characterization before and after printing

provides initial confirmation that the directional printing process does not disrupt

the band gap grading, and that it is a promising method deserving of continued

study.
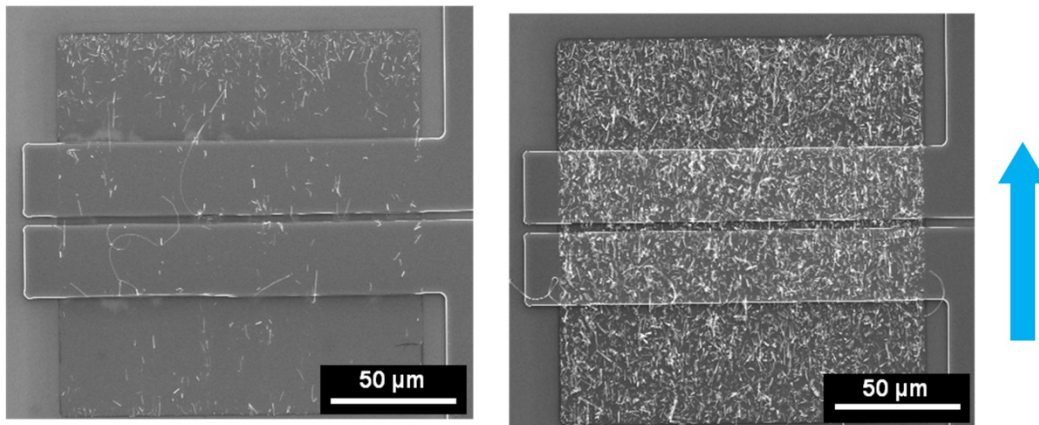
Figure 33. Contact printed alloy nanowires of S-rich (left) and Se-rich (right) regions. Sliding direction indicated by arrow. Rectangular source/drain contact electrodes are visible across the deposition.

From the initial contact printing feedback, the growth goal was defined to

be the creation of a uniform morphology across all compositions. Specifically that

involved reducing the belt-like qualities of the Se-rich segments while

maintaining high density of nanowires in the S-rich region. Because the gas-

phase supersaturation controls the morphology, a uniform supersaturation of CdS

and CdSe should promote a uniform morphology in the alloy nanostructures.

Comparison of the equilibrium vapor pressures of CdS and CdSe in Figure

34 shows that CdSe has a higher vapor pressure than CdS. This means that to

achieve similar supersaturations through production of similar amounts of available vapor, CdSe source material should be maintained at a lower temperature than CdS, assuming saturation of vapor above the source powders during growth.
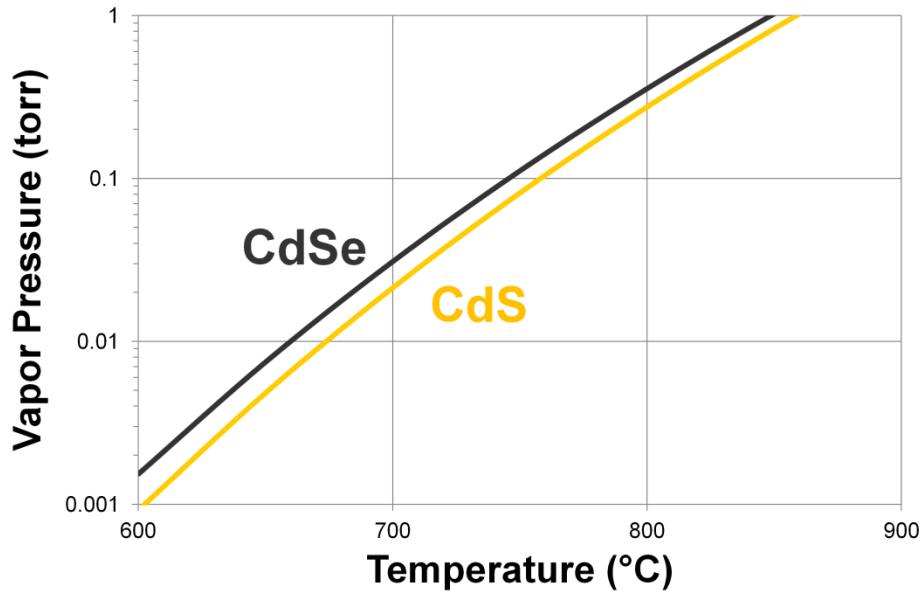
Figure 34. Comparison of equilibrium vapor pressure of CdSe and CdS. Adapted from Mills.[119]

Toward that end, the changes applied to the growth procedure for Sample B was the reduction of the CdSe source temperature by moving its position from the highest possible temperature at the center of the furnace to a position further downstream in the gradual temperature gradient region approaching the open end of the furnace. As discussed in the previous section on CdSe growth, reducing the source temperature limits the amount of available vapor and can reduce the gas-phase supersaturation in an attempt to minimize VS deposition. Also the substrate was placed at a small angle with respect to the tube axis to generate a slight temperature gradient across the surface. Compared to Sample A, the Se-rich

region was at a significantly lower temperature and the S-rich region temperature was reduced slightly. These changes resulted in a slightly reduced length in the S-rich wires and smaller features in the Se-rich region. Further progression was necessary to unify the morphology and length discrepancies between the two end regions.

The growth of Sample C reduced the source temperatures further by reducing the overall furnace set temperature from 900 to 700°C. The substrate position was adjusted toward the center of the furnace to maintain its temperature in the appropriate range for deposition. Additionally, the pressure during the furnace temperature ramp up portion of the growth procedure was maintained above 300 Torr. The pressure shutter method allowed for precise control of the onset of growth, isolating it to the steady state temperature regime only. According to Colli *et al.*, use of the pressure shutter results in less diversity of the final observed nanostructures and allows for characterization of the actual representative morphology for a given set of growth conditions.[120,121] The experimental setup for pure PbS growth of Chapter 2 achieved similar, accurate constraint of growth by using magnetic loading of the source powder in and out of the high temperature zone. Translation of the source powder by magnetic loading is not feasible in the CdS_xSe_{1-x} growth procedure. The complex source dispersion tube geometry within the furnace tube is too susceptible to disruption to permit manipulation of source placement after initial alignment.

The pressure shutter method exploits the relationship between the total pressure within the system and the interdiffusion coefficient of source vapor in the

carrier gas. The diffusion coefficient is inversely proportional to the total pressure.[122] Consequently, above a certain critical pressure, the diffusion of source vapor out of the region directly above the source powder becomes negligible. The flux of source vapor is severely suppressed; thus, there are not significant amounts of available source material arriving to the substrate. Although the carrier gas flow has an effect on the source vapor transport, diffusion is known to be a dominant process in the growth regime studied here, indicated by the locations of the source deposition. In a flow dominated regime, there would only be deposition at the downstream exit of the furnace tube. Actually, there is significant deposition along the tube walls at both the upstream and downstream openings of the furnace, indicating the strong influence of diffusive transport.[120]

With the addition of the pressure shutter to the CdS_xSe_{1-x} growth procedure, the resulting nanostructures of Sample C are much smaller in size (See Figure 31. Note the change in magnification compared to Samples A and B). This indicates that significant amounts of growth were occurring during the transient heat-up phase of the growth timeline. Although the morphology is more consistent due to isolation of growth to only the steady-state temperature regime, the nanostructures are too short for successful contact printing. The as-grown nanostructures need an initially long length because breakage incurred during the transfer process can reduce the average length up to 50%.[109] Also as noted in the previous discussion on CdSe growth, VS still contributes to belt-like growth even at low supersaturations without reaching an exclusively VLS regime. The best

possible compromise of conditions needs to balance all of the constraints for the desired qualities in length and morphology.

Figure 35 shows the nanostructures resulting from the final optimized growth procedure. The length and deposition amount was increased through the combination of decreased growth pressure and increased flow gas velocity. The purpose of reducing the growth pressure is the inverse of the mechanism of the pressure shutter. By lowering the pressure, the diffusion of source vapor was increased. There was a lower backpressure provided by the carrier gas molecules. Therefore, the sublimation rate was increased and led to a higher deposition rate at the substrate.
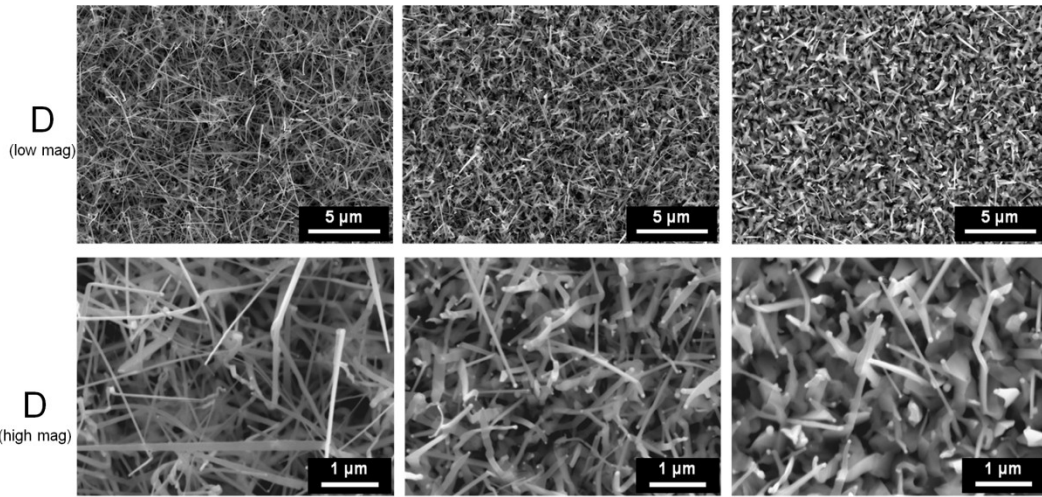
Figure 35. SEM images of final optimized CdS_xSe_{1-x} graded structure, from S-rich to Se-rich (left to right).

Increasing the flow gas velocity from 50 sccm to 100 sccm increased the flux of source vapor that reached the substrates. The flow disrupted the saturated vapor region above the source powders and carried it downstream more quickly. Also as mentioned previously, higher flow is predicted to lead to more constant values of supersaturation over larger areas of position.[74] The center section shows

more deposition and indicates a more equal combination of CdS and CdSe supersaturations.

Low magnification of Sample D compared to the original growth in Sample A shows that the length is more similar over larger regions of the substrate. A slight temperature gradient across the substrate positioned each composition into its preferred growth temperature regime. In the Se-rich region, all of the belt-like features could not be eliminated. Although some short and tapered nanostructures appear, especially at the substrate surface, nanowires extend out from the surface, which are available for transfer during contact printing.

4.4. Device Application: Variable-Wavelength Photodetector

In basic terms, the purpose of a photodetector is to sense light by converting the optical signal into an electrical signal. For a successful device, the active material must show a photoconductive response, meaning a significant increase in electrical conductivity after absorbing electromagnetic radiation. Specifically, nanowires can demonstrate the light-induced conductivity necessary for sensitive light detection or switching between "ON" and "OFF" states.[123] Here, the basic photodetection concept is applied and expanded to create a wavelength-variable phototector device containing CdS_xSe_{1-x} compositionally graded nanowires.

The basic device fabrication process path is displayed in Figure 36. First the nanowires were grown with a spatial composition gradient across a substrate around 1 cm in length. Then, the randomly oriented nanowires were arranged onto

92

the receiver substrate by contact printing. The directional sliding preserved the compositional grading and aligned the wires into parallel assemblies, as shown in the SEM image inset. Finally source/drain electrodes were deposited with electron beam evaporation (5 nm Ti, 40 nm Au).[107]
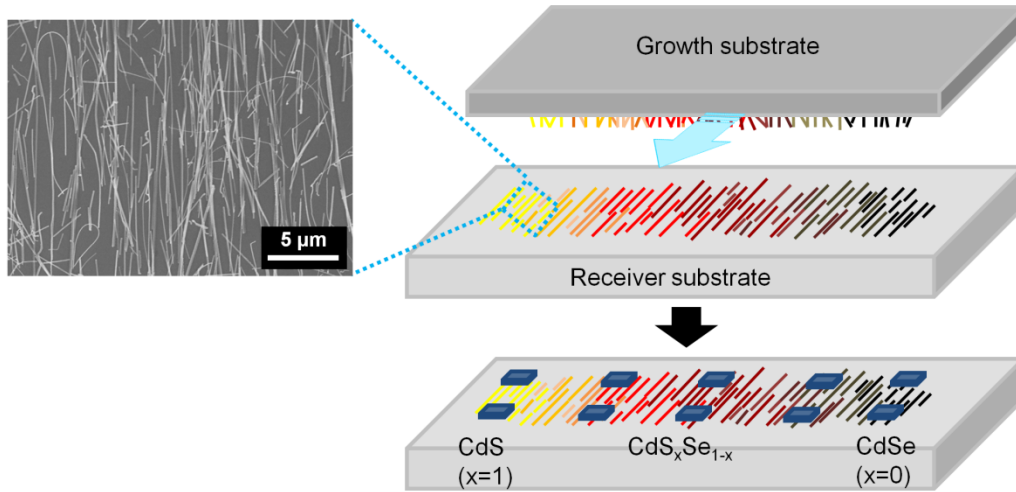
Figure 36. SEM images of final optimized CdS_xSe_{1-x} graded structure, from S-rich to Se-rich (left to right).

The device is comprised of many cells, each of which covers a small wavelength range. All of the cells within the device were fabricated simultaneously. A single growth run generated all of the desired compositions. The contact printing and metal electrode deposition are both single step processes as well, independent of the number of cells within the device.

Each cell detects a different color of light and can convert it into an electrical signal. The alloy composition controls the fundamental band gap value of the nanowire and determines the cutoff wavelength for exciting electron-hole pairs across the band gap.

93

The normalized PL intensity of the contact printing in Figure 37 shows much improvement over the noisy signal of the initial contact printing attempt as shown in Figure 32.
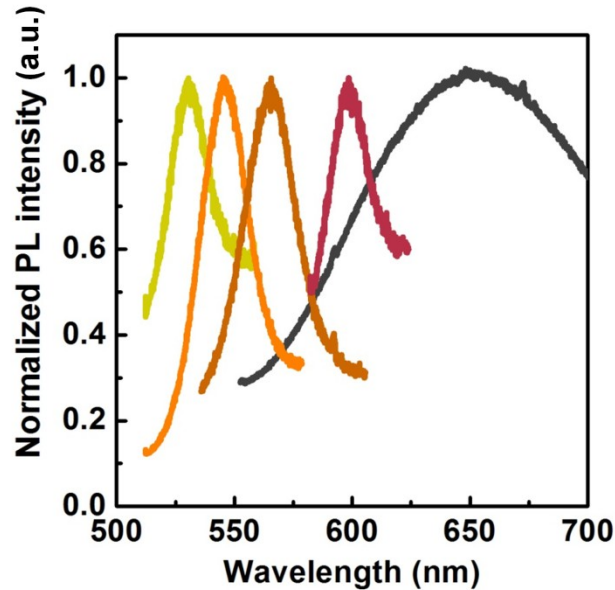
Figure 37. PL spectra from across the contact printed CdS_xSe_{1-x} sample. The peak positions vary between around 525 nm and 650 nm as a function of location across the substrate, corresponding to the S-rich and Se-rich regions, respectively. The peak broadening around the 650 nm range can be attributed to an inhomogeneous composition gradient near the edges of the sample. Future device processing should remove the inhomogeneous substrate edges prior to contact printing. Defect emission is not a likely contributor in this situation because the PL emission of the as-grown sample showed narrow peaks, indicating high quality crystal.

The normalized XRD spectra taken from three different locations on the printed substrate support that the change in wavelength is a direct function of the change in composition (Figure 38). For the small wavelength side, the peaks

match well with the typical bulk wurtzite crystal structure of CdS. Across the sample, the peaks gradually shift to smaller angles, indicating that the lattice constant gradually increases as the nanowires become Se-rich. The extracted lattice parameters are determined to be between the range $x = 1$ (CdS) and $x = 0.52$ ($CdS_{0.52}Se_{0.48}$).[124] The contact printing process is an effective method to maintain the composition grading as designed on the original grown substrate.
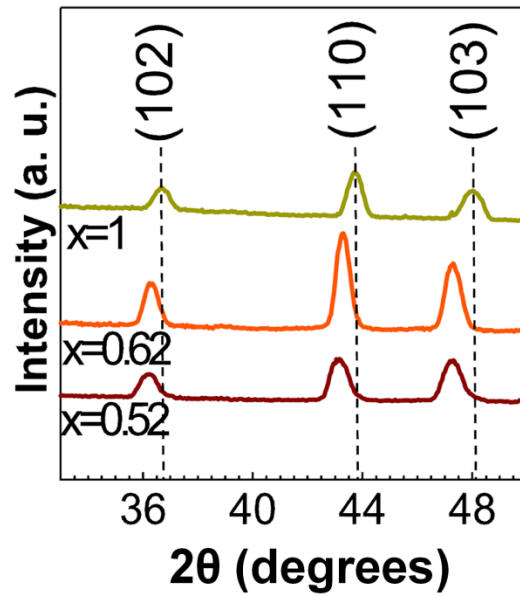
Figure 38. Normalized XRD spectra from three locations along contact printed device. Dashed lines correspond to pure CdS (JCPDS card no. 41-1049).
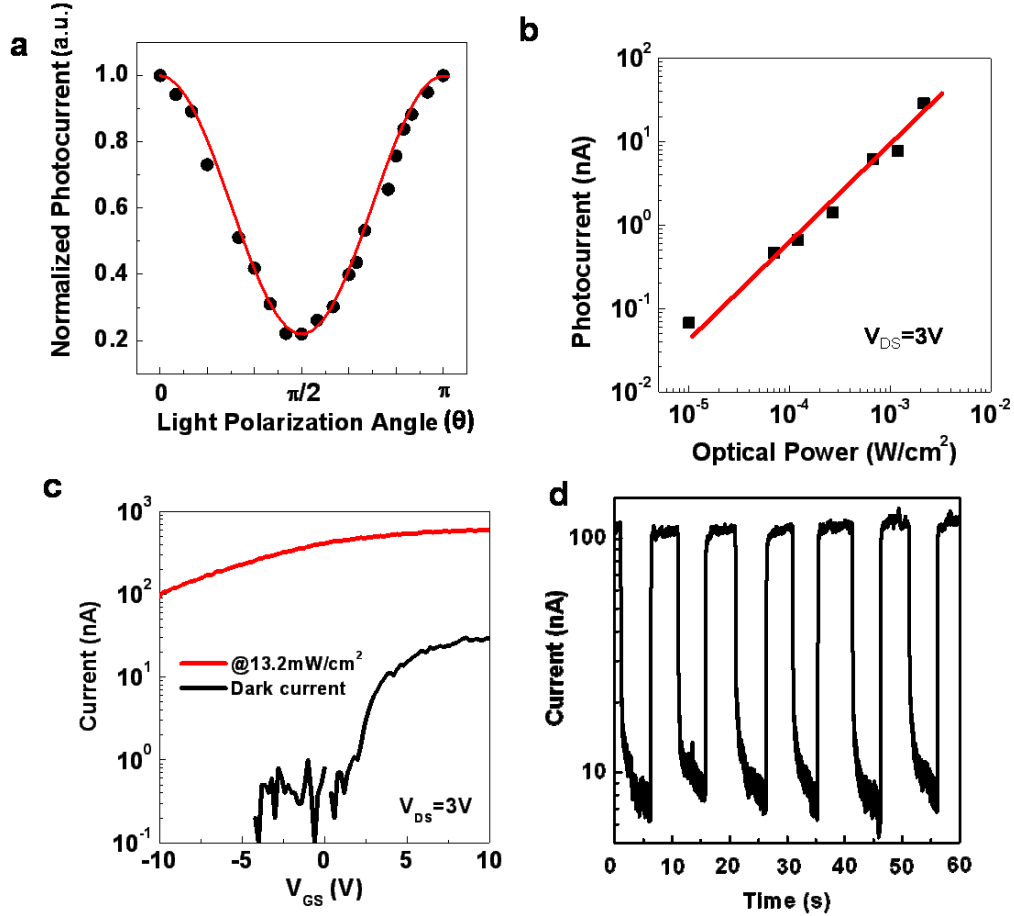
Figure 39. Detailed photoresponse characterization of one representative cell. (a) Normalized photocurrent with light polarization, (b) photocurrent with optical power. V_{DS}: voltage applied across source/drain contact electrodes, (c) light and dark current with back-gate voltage V_{GS}, (d) photoresponse under chopped light illumination (halogen lamp, 1 mW cm^{-2}).

Figure 39 contains the detailed photoresponse characterization of one representative cell within the nanowire photodetector device. This cell has a composition near the center of the alloy range with x = 0.52 ($CdS_{0.52}Se_{0.48}$). The polarization-dependent photoconduction measurement was performed to analyze the alignment of the nanowires, which is critical for uniform response of the devices.[113] Nanowire arrays with strong alignment show polarization sensitivity because the majority of light absorption occurs when the polarization of the

96

incident light is parallel to the long nanowire length axis.[125] The photocurrent was measured by rotating the polarization direction of the incident light source (halogen lamp, 1 mW cm^{-2}). θ is the angle between the nanowire orientation and the polarization direction of the incident light. The current was normalized by the current at $\theta = 0$. The photocurrent response shows the expected harmonic behavior and can be fitted to a $\cos^2\theta$ function. The polarization anisotropy is calculated through the relation:

$$\rho = \frac{(I_\parallel - I_\perp)}{(I_\parallel + I_\perp)}$$

where $I_\parallel$ and $I_\perp$ are the photocurrents obtained from light illumination parallel and perpendicular to the nanowire direction, respectively. Randomly oriented wires would show zero polarization anisotropy. Alternatively, even perfectly aligned wires would not show a value of 1 because some light absorption occurs when the polarization is aligned along the narrow radial dimension of the nanowires. The polarization anisotropy extracted from the data from this nanowire photodetector device is ~0.67, which represents significant polarization sensitivity and successful alignment by directional contact printing.

The dependence of the photocurrent amplitude on the optical power is shown in Figure 39b. A constant voltage of 3 volts was applied across the source/drain contact electrodes while the optical power (light intensity) was incrementally increased. The photocurrent response is basically linear with a fitted slope of 1.09. This slight deviation from linearity is attributed to the complex interactions between electron-hole generation, trapping, and

recombination processes.[110] For this device, the strength of the electrical signal is directly related to the strength of the light intensity incident upon it. This test demonstrates that the photodetector is uniformly sensitive over a large range of optical power.

The plot in Figure 39c compares the current output with and without illumination by a halogen lamp (13.2 mW cm^{-2}) as a function of gate bias, V_{GS}. For $V_{GS} = 0$ - 1 V, the ratio between photocurrent and dark current is very high (>100). Low dark current is desirable for high signal-to-noise ratios during device operation. The photocurrent/dark current ratio can be tuned depending on V_{GS}. Most importantly, this plot demonstrates that the device resistance is dramatically decreased under white light illumination. The light induces efficient electron/hole photogeneration within the CdSSe alloy nanowire. The electron/hole pairs are subject to field-induced carrier separation by the applied voltage. The electrons and holes then flow to the contacts to be detected as the photocurrent.

Time-resolved photoresponse measurements were conducted for multiple illumination cycles using chopped light illumination (halogen lamp, 1 mW cm^{-2}) as shown in Figure 39d. Each photoresponse cycle is comprised of three transient regimes: a sharp rise, a generally steady-state regime, and a sharp decay. The response time and recovery time, defined as the time between 10% and 90% of maximum photocurrent, are 200 ms and 800 ms, respectively. The time constant for response (τ_{resp}) is 130 ms, and those for slow and fast recovery ($\tau_{rec,slow}$, $\tau_{rec,fast}$) are 80 ms and 350 ms, respectively, which are found by fitting the equations $I = I_0(1 - e^{-t/\tau})$ and $I = I_0 e^{-t/\tau}$ to the leading and trailing edges of a single pulse. The

biexponential behavior of the recovery is consistent with previous studies of CdS and CdSe nanostructures.[126-128] Overall, the consistent photoresponse over multiple illumination cycles demonstrates the reproducibility and robustness of the nanowire optical photodetector.

The spectral response was investigated from representative cells corresponding to the S-rich, center, and Se-rich regions of the compositionally graded nanowire arrays. The normalized photocurrent with $V_{DS} = 3$ V is plotted in Figure 40 as a function of illumination wavelength. The illumination wavelength was controlled by passing it through filters to incrementally span a large range of incident light wavelengths.
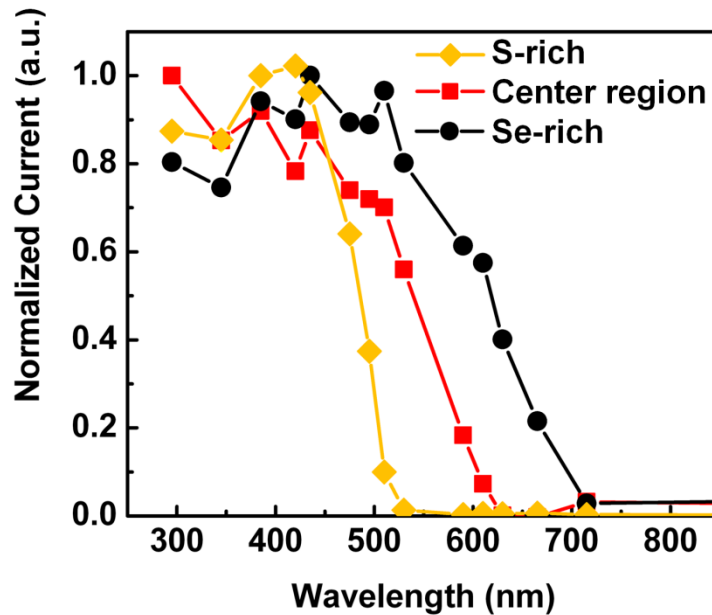
Figure 40. Spectral response from three cells within the photodetector device.

The response transition wavelengths extrapolated for the plotted devices are ~510 nm, ~600 nm, and ~690 nm. Above the transition wavelength, the cells do not show any photocurrent generation because the energies of the incoming photons are less than the semiconductor band gap energy of the nanowire

material. They do not contain enough energy to excite an electron-hole pair; thus, no photocurrent is generated. For incident wavelengths below the transition, the photon energy is sufficient to span the band gap energy. These generated electron-hole pairs are influenced by the applied voltage to separate into carriers, flow to the contacts, and contribute to the photocurrent. Especially for the Se-rich region, there is some noise in the below-threshold region that could be improved by higher quality printing or nanowire growth. The Se-rich region also exhibits a fairly wide wavelength range to transition from zero to full response, indicating a possible broad range of composition within that cell. Overall, the spectral response provides sufficient validation of a tunable-wavelength photodetector array based on the variable band gap of CdS_xSe_{1-x} alloy nanowires.

4.5. Summary

In conclusion, unifying the values of CdS and CdSe supersaturations across the substrate by altering source temperatures, substrate temperatures, pressure, and flow resulted in a more uniform morphology and length. Combined with optimization of the contact printing process variables, the growth optimization led to the successful demonstration of an optoelectronic device that utilizes the benefits of compositionally graded substrates.

The spectral response of the wavelength-variable photodetector device was demonstrated, with each cell containing a distinct composition of CdS_xSe_{1-x} alloy nanowires. The results prove the feasibility of devices fabricated from compositionally graded substrates and the contact printing method. The directional printing process successfully preserved the spatial composition

grading. Future devices will expand upon these techniques to extend wavelength coverage beyond the wavelengths demonstrated here and to increase spectral resolution. As the number of cells increases, so does the manufacturing advantage of using compositionally graded substrates. All of the required compositions are integrated on a single substrate and generated from a single growth run. Alternatively, if a device is constructed of nanowires grown in separate growth runs, it requires significantly more furnace time and post-growth manipulation to arrange composition grading with spatial position. Creating all desired alloys in only one CVD furnace run provides a great cost and time benefit to the overall device production process.

Chapter 5

CdSSe AXIAL HETEROSTRUCTURE NANOWIRES

Heterojunctions between different semiconductor materials are crucial to the function of advanced optoelectronic devices. Heterojunctions in thin films are well studied and fully exploited in commercial applications, including photodiodes, solar cells, lasers, and LEDs. On the other hand, heterojunctions in nanostructures represent an active area of research. Further exploration is required to achieve their complete device potential. Heterostructure nanowires offer the same size and property benefits of single component nanowires, but they also provide additional degrees of freedom for realization of novel functionalities. [129,130] Band engineering along the length of a nanowire through composition modulation can be used to tailor device properties. Axial heterostructure nanowires are an important area for research due to their potential contributions toward functional integrated nanosystems.

The most common growth mechanism utilized for axial heterostructure nanowires is VLS. Switching the vapor composition mid-growth changes the composition of the growing crystal. This technique is used to create a junction between two distinct composition segments within the nanowire. The segments are separated by an interface transition region due to the reservoir effect from the liquid catalyst droplet. [131] At the instant when the vapor composition is switched from the first growth species to the second, the liquid catalyst droplet still contains residual incorporated species from the first phase of growth. Growth in VLS proceeds by a layer-by-layer deposition process, such that each layer

crystallizes some of the first species until they are completely consumed and replaced by the second species.[132] The crystal grown during this transition regime contains both species, resulting in a diffuse interface.[131] The growing nanowire does not contain exclusively second phase species until all of the first phase species have been depleted from the catalyst. Thus, the width of the junction interface between the two segments is controlled by the solubility of the vapor species in the liquid catalyst droplet.[133] If the species are less soluble in the catalyst, there will be fewer of them available within the droplet to act as a reservoir. They will be depleted rapidly over a few layers of deposition, with the interface approaching atomic abruptness.

Reduction of solubility in the catalyst has been achieved by various methods. Perea *et al.* tuned the solubility by alloying the liquid gold catalyst with gallium.[133] They demonstrated a systematic increase in interface sharpness by increasing the Ga content, which decreased the solubilities of the source materials within the liquid catalyst droplet. Alternatively, Wen *et al.* eliminated the liquid catalyst and replaced it with a solid catalyst. Growth occurred through the vapor-solid-solid mechanism.[132] The low solubility of both Si and Ge in the solid catalyst permitted the creation of compositionally abrupt junctions between Si and Ge segments.

Conversely, a diffuse interface is essentially an alloyed region between the two distinct composition segments. This type of region is known to act as a buffer and mitigate the inherent lattice mismatch strain energy of the heterojunction.[134] The small nanowire cross-section provides further effective strain relief in the

103

junction region by elastic relaxation, as opposed to traditional thin film junctions, which are constrained in the lateral direction.[17]

Specifically for the CdS_xSe_{1-x} alloy system, single composition nanostructures have been grown by means of the VLS mechanism with one composition per growth run.[100,124,135-138] Nanowires across the whole composition range have also been fabricated on a single substrate in a single growth run.[106,107] With regard to heterostructures, various configurations have been reported. Kim *et al.* produced CdSe nanosheets with lateral CdS segments irregularly nucleated along the side edges.[138] They improved on the growth process to generate lateral heterostructure nanobelts with continuous CdS side segments surrounding a central CdSSe alloy section.[139] Using CVD, they first heated CdSe source powder to grow the central nanobelts, then cooled the system to room temperature, then heated CdS source at a lower growth temperature to generate the lateral segments. Xu *et al.* reported similar lateral heterostructure nanobelts with comparable morphology, but they were grown by a different CVD procedure.[140] CdS central belts were grown initially and then converted to CdSSe alloy by anion exchange of S for Se in the presence of CdSe vapor. Finally, an additional CdS growth stage at a lower temperature produced the CdS lateral side segments.

For nanowires, Gu *et al.* created compositionally graded CdSSe alloy nanowires with no abrupt junctions between composition regions.[141] The composition was smoothly altered from pure CdS to pure CdSe along the length of the wire. The CVD procedure involved slowly moving source materials

104

through the furnace to continuously modify the vapor composition ratio throughout growth. As an alternative to CVD methods, Ouyang *et al.* reported a solution-liquid-solid growth process in which metal catalysts were introduced to organic solutions containing the reactive precursor materials.[142] Nanowire heterostructures with CdS-CdSe-CdS segment modulation were grown, resulting in total lengths around a few microns. The 20 nm wide interfaces were found to be epitaxial with no alloying between the two phases and less than 5% stacking faults.

Based on the literature reported CVD growth of CdSSe heterostructures, dramatic or complete switching of the source vapor composition generally tends to terminate axial VLS growth and promote lateral VS growth of side segments. Slow continuous switching of the source vapor composition shows continuation of axial growth but does not actually form a heterojunction between two distinct segments. In order to achieve the desired heterostructure, some degree of two phase growth is required. The optimized growth procedure must appropriately balance between conditions to achieve a junction between two distinct composition regions and conditions to achieve continuation of axial growth. In the work described in this chapter, it was found that the axial growth continuation from Se-rich to S-rich regions is a sensitive process. A relatively subtle change in source vapor composition, in combination with a substrate temperature change, is sufficient for creating a heterojunction between two segments.

Also in literature, the substrate temperature was a direct function of the source temperature. The growth setup established in this chapter permits

independent control of the source and substrate temperatures, both in time and magnitude. This useful feature is important not only for the optimization CdSSe growth presented here, but also for general optimization of any heterostructure composition or morphology grown in this system. The independent variable control of this setup could ultimately lead to a wider variety of heterostructures containing higher quality crystal material.

For the optoelectronic applications of interest here, interface abruptness is less critical than high quality crystal in both segments and within the interface for strong radiative recombination, thus strong light emission. This work pushes the boundaries of heterostructure growth in direct band gap semiconductor material for potential optical applications in color-tunable LEDs and displays, as will be proposed.

5.1. Growth procedure

As shown in Figure 41, CdSSe heterostructure nanowires were grown by CVD in a one-zone tube furnace (Lindberg/Blue M). Within the 1.5 inch diameter quartz furnace tube, two 0.375 inch diameter quartz tubes individually controlled the source material position and flow. Measured amounts of source powder material (0.24 g CdS, 0.27 g CdSe. Sigma-Aldrich, 99.99%, trace metals basis) were placed near the openings of their respective source dispersion tubes. CdS source powder was located at the center of the furnace and CdSe was slightly upstream. A silicon substrate with sputtered gold film (~10 nm thick) was placed downstream. The system was evacuated to below 40 mTorr by a rotary vane vacuum pump (ULVAC GLD-136). The flow of N_2 carrier gas through the

furnace tube was used to backfill the system until the pressure reached 165 Torr. The source dispersion tube flows were then turned on at 55 sccm Ar, 5% H_2 through each tube. The furnace was heated to 925°C over a period of 20 minutes.
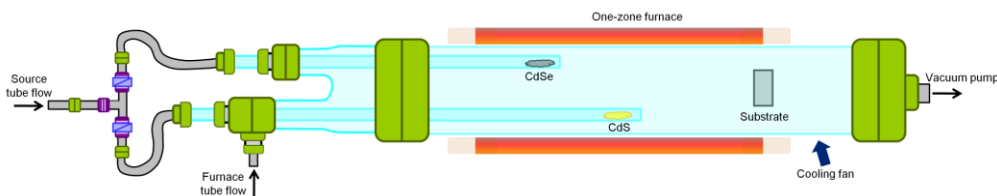
Figure 41: Schematic diagram of the CVD system and dual port configuration used for CdSSe axial heterostructure growth. The rounded green rectangles represent ultra-torr vacuum fittings. The purple crossed rectangles represent valves that control flow through each source dispersion tube. The cooling fan was directed at the exposed quartz tube at the outlet of the furnace.

Table 4 summarizes the differences in growth parameters for Phase 1 and Phase 2 of the growth procedure. Phase 1 began when the furnace reached the set temperature, and the conditions were maintained for 70 minutes. At the end of Phase 1, the cooling fan located at the downstream opening of the furnace was switched on at its maximum speed. This action caused the substrate temperature to be decreased by 265°C over a transition period of 20 minutes. The start of Phase 2 was marked by shutting off flow through the CdSe source dispersion tube and moving the CdSe source 1 cm upstream. Discontinued flow through the CdSe source dispersion tube effectively doubled the flow through the CdS tube because they were jointly connected to a common gas cylinder by a "T" connection as detailed in Figure 41. The CdSe source relocation effectively reduced the CdSe source temperature by about 15°C. At the conclusion of Phase 2 after 80 minutes of growth, the furnace was turned off. The cooling fan remained on, and the

system cooled to room temperature. Throughout growth, the pressure was maintained near the nominal value of 165 Torr. The flow gas composition was also constant, with N_2 through the furnace tube and Ar, 5% H_2 through the source dispersion tubes.

Table 4. CdSSe axial heterostructure nanowire growth parameters for standard condition of growth

Procedure Phase	Temperature (°C)			Flow (sccm)		Time (min)
	CdS Source	CdSe Source	Substrate	CdS	CdSe	
1st Phase	925	866	693	55	55	70
2nd Phase	925	852	428	110	0	80

In the following sections, this growth procedure will be referred to as the standard condition. In order to determine the contribution of each growth variable change between Phase 1 and Phase 2, the growth procedure will be divided into test conditions. The results of each test condition will be compared to the results of the standard condition.

5.2. Characterization of Segmented Wires

Figure 42 contains the SEM, optical microscopy, and UV-illuminated PL images of CdSSe axial heterostructure nanowires resulting from the standard condition. As clearly demonstrated in the representative SEM image, the standard growth procedure produced large, uniform areas of nanostructures with high number density.
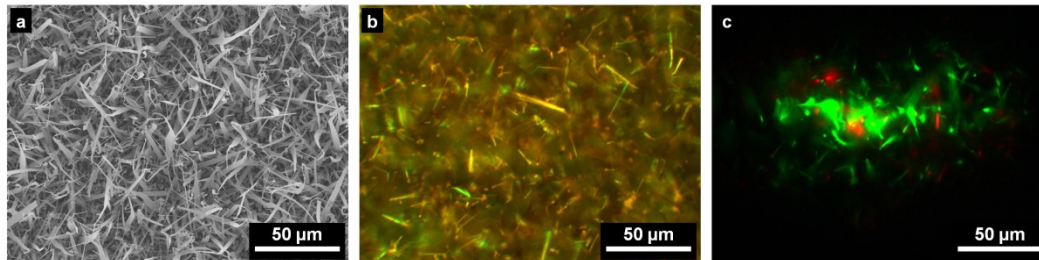
Figure 42. As-grown CdSSe axial heterostructure nanowires by the standard condition: (a) SEM, (b) optical microscopy, (c) UV-illuminated PL.

Figure 42b is an optical microscopy image illuminated by a broadband light source. The color results only from light scattering from the surfaces of the nanostructures. The internal optical properties of the nanostructures were characterized by an UV PL system (Picoquant semiconductor pulse diode laser, 40 megahertz repetition rate, 50 picosecond pulse width) with an excitation wavelength of 405 nm. Figure 42c shows the real color UV-illuminated PL image that corresponds to the broadband-illuminated image of Figure 42b. The UV-illuminated image reveals two-color emission from the nanostructures. The distinct red and green colors were emitted from separate segments along the nanowire axis, with the red color originating from the base region closest to the substrate. The red segments were therefore grown during Phase 1.

Figure 43 shows the PL spectrum of the colors emitted from the as-grown CdSSe axial heterostructure nanowire sample as shown in Figure 42c. As determined by Gaussian peak fitting, the peak wavelengths are 544 and 635 nm, corresponding to green and red color emission, respectively. The peak widths (full width at half maximum) are indicated by the capped lines. This notation will be utilized in later plots that summarize as-grown PL spectra for different growth conditions.

109
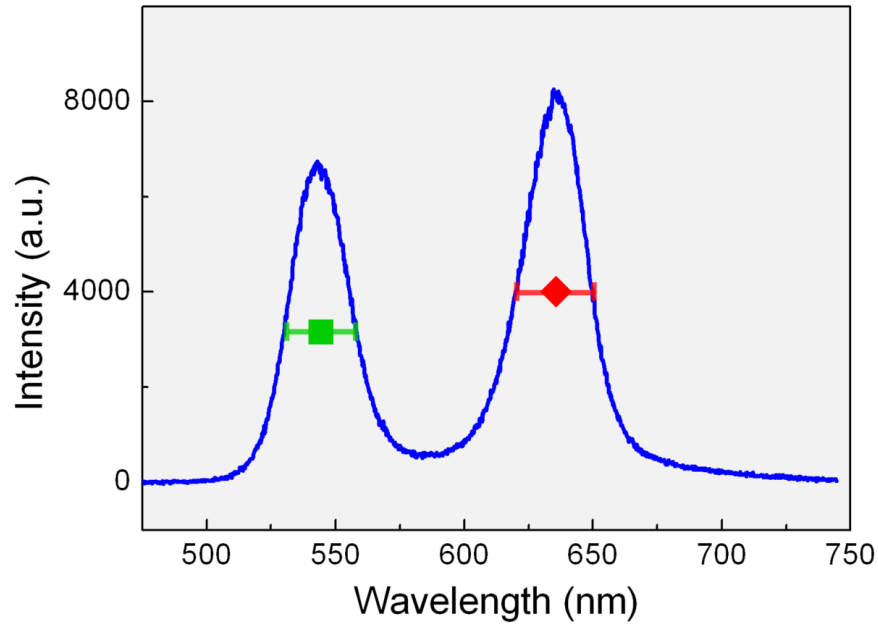
Figure 43. PL spectrum of as-grown CdSSe axial heterostructures, corresponding to the emission of Figure 42c. The green square and red diamond indicate the peak wavelength values and the capped lines represent the peak widths (full width at half maximum), as determined by Gaussian peak fitting.

Although the generated heterostructures were a mixture of both nanobelt and nanowire products, the individual heterostructure characterization of this work will focus on the long nanowires with uniform diameters. The standard condition of growth generates enough of the structures of interest, which can be located after a dispersion process. The proposed device application involves a single wire, as opposed to the contact-printed photodetector of Chapter 4 which involved thousands of nanostructures during the device processing. For future device manufacturing, the relative yield of nanowires compared to nanobelts can be improved by applying similar techniques as established for the contact printing optimization. Overall at this point in the research, the current yield of desired nanostructures is sufficient for characterization and device proposal.

The heterostructure nanowires were isolated for further characterization by a stamp printing dispersion process. The substrate surface was gently touched against a glass receiver substrate in order to preferentially collect the long, straight nanowires of interest. The nanowire lengths became obvious after they were positioned flat on the receiver substrate, and they can reach a length of more than 100 microns.

Figure 44 displays the change in composition along the length of an individual CdSSe axial heterostructure nanowire. In the UV-illuminated PL image, the Au catalyst tip is visible as a yellow bright spot at the end of the green segment. Because the liquid droplet rides on the top of the growing wire during VLS growth, this observation further supports the conclusion that the green region was grown during Phase 2, and the red region was grown during Phase 1.

The composition, plotted as sulfur fraction (x), was extracted from the position-dependent micro-PL scan data. The laser beam was focused down to a spot size around 2 microns, and it was scanned along the wire in 5 micron increments. Each collected PL spectrum along the length of the wire contained one strong peak, corresponding to the local light emission from that small region of the wire. The interface width between the two segments was estimated around 500 nm. This is a reasonable value because it is on the order of the wire diameter, which is standard for typical liquid-mediated heterostructure growth subject to the reservoir effect.[131] Both the interface region alloying and the small cross-section of the nanowire contribute to the alleviation of the lattice mismatch strain between

the segments, permitting high quality crystal without defects and strong emission from both segments.
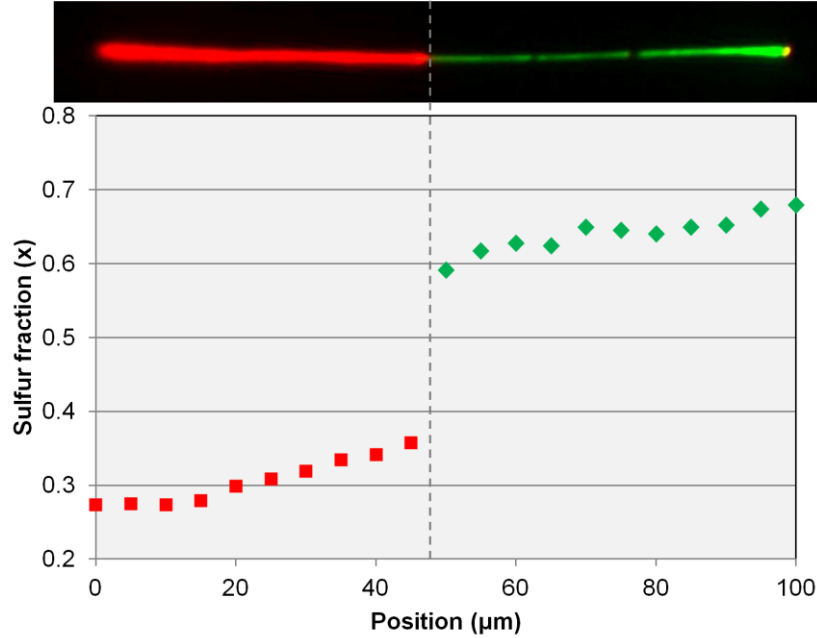
Figure 44. UV-illuminated PL image of a single CdSSe nanowire with axial heterojunction (top). Sulfur fraction (x) plotted along length of wire (bottom). The dark regions in the green section correspond to local regions with low emission intensity.

The detected light emission is from the band edge, meaning that the peak wavelength converted into energy corresponds to the band gap of the excited material. The alloy band gap is directly related to the alloy composition by the following equation:

$$E_g(CdS_xSe_{1-x}) = xE_g(CdS) + (1-x)E_g(CdSe),$$

where x is the sulfur fraction, and E_g are the known band gap values of the binary endpoints: 2.45 eV for CdS and 1.75 eV for CdSe. Here the quadratic bowing parameter is neglected according to Kwon *et al.* due to the effective strain relaxation provided by the nanowire structure.[100]

The composition plot clearly indicates a sharp transition between the red Se-rich segment and green S-rich segment of the nanowire, jumping from a composition of $x = 0.36$ to 0.59. Within each segment, there is a smaller variation in composition of around 0.09. The composition of the red region ranges from $x = 0.27$ to 0.36, and the composition of the green region ranges from $x = 0.59$ to 0.68. The mid-point composition of each section generally corresponds to the overall composition extracted from the as-grown PL measurement, which averages over the entire lengths of many wires. This indicates that the composition change along the length is roughly similar for all of the nanostructures grown on a single substrate. The growth parameter differences between Phase 1 and Phase 2 of the standard condition, which serve to change the source vapor composition and substrate temperature, successfully alter the growing wire composition dramatically without disrupting the growth continuation of the whole wire. Within each growth phase, there were apparently subtle fluctuations in the source vapor composition or substrate temperature that produce a composition change in the growing nanowire. Physical vapor transport methods in general are known to have local variations in gas flow dynamics and growth temperatures.[120] But overall, the smooth composition variation across each segment ($\Delta x = 0.09$ over ~50 microns) is minor in comparison to the significant composition change over a narrow region between the two segments ($\Delta x = 0.23$ over ~0.5 microns).

To review, a change in emission wavelength is observed along the length of the nanowire. The emission wavelength is converted to the band gap of the

113

material, which is controlled by the alloy composition. Therefore, a change in emission wavelength directly corresponds to a change in composition. Based on the band gap interpolation as described, it is equivalent to plot either wavelength or sulfur fraction. The plots based on PL data depicted in this chapter are plotted in terms of emission wavelength. As previously introduced, the emission wavelength peak is denoted with a solid data point, with the full width at half maximum indicated by capped lines.

5.3. Identification of Variable Effects

The general goal of the two-phase CVD procedure is to grow the first segment and then continue axial growth to the second segment without detrimentally affecting the initially grown material. Overall, the changes to the growth parameters between Phase 1 and Phase 2 serve to alter the source vapor composition and the substrate temperature. Each parameter has an influence on the final observed growth. In the following sections, each parameter is isolated, tested, and discussed.

5.3.1. Comparison to Pure Sources

To compare the effect of source vapor composition, CdSSe segmented growth was attempted with only CdSe source vapor during Phase 1 and only CdS source vapor during Phase 2. This is in contrast to the standard condition in which both CdS and CdSe source powders were intentionally heated at different ratios during each phase. Growth experiments following the standard condition and pure sources during each phase were halted mid-procedure to reveal the evolution of the optical and morphological characteristics throughout growth.

114

As expected, Phase 1 growth with only CdSe source in the furnace shows PL emission that is red-shifted toward the longer wavelength of pure CdSe as compared to the source configuration of the standard condition (Figure 45). The emission does not exactly correspond to pure CdSe, indicating that trace amounts of CdS incorporated into the growing CdSe. CdS was present in the CVD system as tube wall deposition, residual from previous growth experiments. The PL emission intensity is weak, possibly due to defects in the crystal structure because the growth parameters are not optimized for the growth of that specific composition. The morphology resulting from Phase 1 of pure CdSe source growth is also undesirable. The majority of deposition is in the form of short and wide nanobelts. During standard condition growth, intentionally introduced CdS present during Phase 1, influences the morphology toward long and radially symmetric nanowires. This is consistent with the observations made for optimization of CdS_xSe_{1-x} growth for contact printing in Chapter 4, in which S-rich alloys tend to be more wire-like than pure CdSe which tends to be belt-like. For future devices made up of these segmented heterostructure nanowires, it is more desirable to obtain long, constant diameter nanowires with alloy compositions, rather than the irregular nanobelt morphology made of pure CdSe.
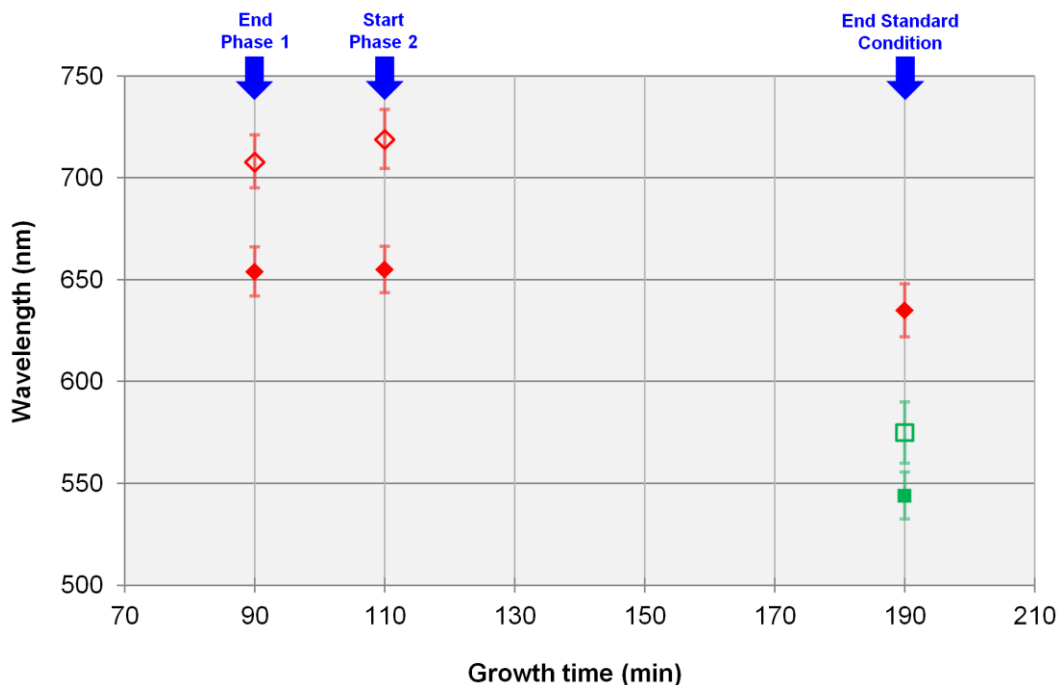
Figure 45. Comparison of PL emission wavelengths from as-grown samples with different source configurations: standard condition (solid points), and pure sources during each phase (hollow points).

After completion of Phase 2 with pure CdS source, the only observed peak is at 575 nm. The S-rich vapor environment during Phase 2 further degraded the quality of the original Se-rich nanobelts until the emission was below detectable limits. The new growth during Phase 2 corresponds to a composition of $x = 0.58$. Although CdSe source powder was not intentionally introduced during Phase 2, there was CdSe available in the form of deposition that occurred during Phase 1. The sulfur fraction of the wires grown during Phase 2 with pure CdS source ($x = 0.58$) is further away from pure CdS ($x = 1$) than the sulfur fraction of the green segment grown by the standard condition ($x = 0.76$). For standard condition growth, an appropriate ratio of CdS to CdSe source vapor during Phase 2 seemed to stabilize the quality of the originally grown Se-rich segment while still supporting growth of new S-rich material. Under these conditions, the emission

116

intensity of the red peak is not detrimentally affected by Phase 2 growth. The peak wavelength of the red emission is influenced by Phase 2 growth with a slight blue-shift from 655 to 635 nm. This wavelength shift with time will be investigated in more detail in the following section. Overall, the growth procedure using pure sources during each phase produces nanostructure morphology and PL emission that are unacceptable for device applications, mainly a smaller sulfur fraction, lack of Se-rich emission, and nanobelt morphology.

Although the use of pure sources during each growth phase has been reported for other CdSSe heterostructure growth,[138-140] a mixture of both CdS and CdSe vapor during the two growth phases was found to be more successful in producing the desired combination of composition values and morphology. The relatively subtle source vapor composition change between Phase 1 and Phase 2 of the standard condition, in combination with change in substrate temperature, is enough to achieve distinct compositions in the heterostructure nanowire.

5.3.2. Growth Time

For the CdSSe system, it is known that Se-rich material tends to grow at higher temperatures than S-rich material.[106,124,138,139] For the standard condition established here for axial heterostructure nanowires, Se-rich growth was selected for Phase 1 so that the substrate temperature would be decreased as opposed to increased during the subsequent Phase 2. Increased temperature during Phase 2 would cause re-sublimation of the deposited material, with the potential to completely vaporize the initially grown nanowire segments. Additionally, higher temperatures promote faster diffusion such that the heterojunctions would be less

117

stable. The heterostructures would be more susceptible to undesirable diffusion effects, including ion exchange with the vapor environment by diffusion across surface areas or interdiffusion within the wire around the interface, both of which will be discussed in more detail.

As mentioned in the previous section, the emission wavelength of the Se-rich segment changes between the onset and completion of Phase 2 (110 to 190 minutes). Nanowires by definition have a high surface to volume ratio compared to bulk materials. This fundamental characteristic is significant in this situation because the large surface areas can be dramatically affected by the vapor environment surrounding them.[30,140,143] As intended, the vapor composition changes cause a change in the composition of the growing nanowire. An additional consequence is that the vapor environment also influences the composition of the previously grown material through diffusion and ion exchange.

To investigate the effect of growth time on previously grown material and to characterize the ion exchange processes, eight growth experiments were completed according to the standard condition. Each experiment was halted at a different point along the growth timeline at 20 minute increments, including two experiments with even longer growth times than specified by the standard condition. It is assumed that interrupting the procedure effectively captures the wavelength characteristics at that moment during growth. Each experiment was cooled by the same procedure using the cooling fan at maximum speed. The samples were characterized by PL for their peak wavelengths and peak widths.

Figure 46 illustrates the variation in PL emission wavelength with time throughout the growth procedure. From the end of Phase 1 at 90 minutes, until the middle of Phase 2 at 170 minutes, the wavelengths are basically stable. This represents a steady-state condition in the vapor composition, which generates a relatively constant composition in the growing nanowire, as supported by the single wire scan of Figure 44. The red wavelength peak remains strong around 655 nm, indicating that the transition from Se-rich Phase 1 growth into S-rich Phase 2 growth does not destroy the initially grown CdSe segments. The new S-rich growth proceeds at the preferred composition for the specific combination of vapor composition and substrate temperature. During this regime, there exists a range of acceptable compositions that are not deteriorated by the surrounding vapor environment, including that of the Se-rich segment. The peaks do not show a dramatic increase in width, which indicates minimal interdiffusion within the wire. The interface between the two compositions is stable in this regime.

From 170 to 210 minutes into growth, there is noticeable blue-shift of the peak emission from both segments, corresponding to a value of -0.8 nm per minute. During this regime it is apparent that the surrounding vapor has become more S-rich than the previous regime. The S-rich atmosphere provided an increased number of S atoms available to diffuse into both segments of the nanowire through their large surface areas. The S atoms preferentially replaced Se atoms in the nanowire crystal material, changing the alloy composition as detected by the change in band edge emission wavelength. This anion exchange by diffusion of vapor through nanowire sidewalls is consistent with the observed

119

behavior for other CdSSe nanostructures.[140] Again, no broadening of the peaks is observed. It can be expected that the diffusion with the vapor over the surface areas will be a much more noticeable effect than diffusion across the interface within the wire due to the relative size difference between the entire surface area and the small cross-sectional diameter of the wire.
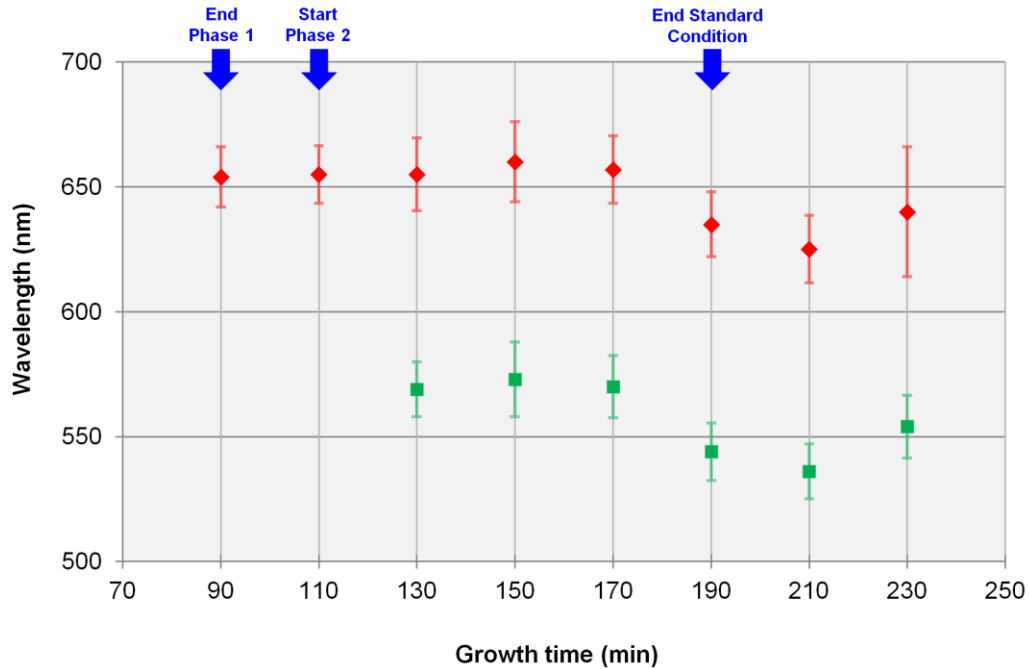
Figure 46. PL of as-grown CdSSe heterostructure nanowires by the standard condition, with growth interrupted at 20 minute increments.

The trend for very long growth times in the region from 210 to 230 minutes is a red-shift of both peaks and a broadening of the Se-rich emission peak. By this time during growth, the CdS source powder was nearly consumed, resulting in a Se-rich vapor environment. The CdS source material that did remain after growth exhibited an orange color instead of yellow, indicating that Se had incorporated into the previously pure CdS source powder. Analogously, the red-shifted emission peaks can be attributed to the Se atoms incorporating into both

segments of the nanowire by anion exchange. The peak broadening indicates interdiffusion within the wire around the interface between the Se-rich and S-rich segments. As the interface became more diffuse, a wider range of alloy compositions was created in the buffer region, corresponding to a broad range of emission wavelengths. A long growth time with the sample at elevated temperatures was sufficient to complete the apparent incubation period before interdiffusion within the wire became significant. During even longer growth times, the nanowires may continue to progress toward equilibrium by homogenization into single composition alloys, completely eliminating the heterojunction interface.

The PL emission wavelengths of both peaks were found to vary with growth time during the growth procedure. The vapor composition defines a preferred composition for new growth and a range of acceptable compositions for previously grown material that are stable in the vapor environment. For the current masses of source powders specified by the standard condition, the blue-shift trend ends at 210 minutes into growth. For other masses or ratios of source powders, the trend potentially could be extended further to create increasingly S-rich material. The current standard condition ends at 190 minutes into growth, which generates compositions corresponding to desirable wavelengths, prior to entering the peak broadening regime.

5.3.3. Effect of CdSe Flow

For Phase 2 of the standard condition, flow through the CdSe source dispersion tube was turned off. The only transportation method for CdSe was

121

diffusion, so the CdSe source flux arriving at the substrate was dramatically

reduced. For the test condition, the CdSe flow was left on at 55 sccm during

Phase 2. This implies that the CdS flow was also 55 sccm instead of 110 sccm due

to the joint connection to the gas cylinder as previously described.

As shown in Figure 47, the resulting growth of the test condition exhibits

only red and orange emission, centered between 600 and 650 nm.
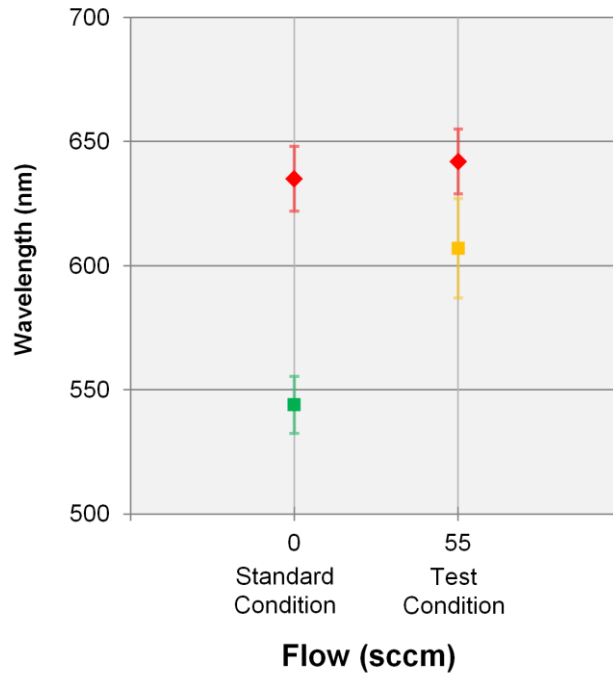
Figure 47. Effect of CdSe source dispersion tube flow during Phase 2.

The large amounts of CdSe source vapor arriving at the substrate during Phase 2

generated Se-rich growth, in spite of the reduced substrate temperature. The

decrease in substrate temperature was not sufficient to promote growth of S-rich

segments in the highly Se-rich vapor environment. In this situation, the source

vapor effect dominated over the substrate temperature effect. For this test

condition, the final lengths of the nanowires are much shorter than the standard

condition. This indicates that the increased CdS source flow during Phase 2 is

critical to achieving longer nanowire lengths. It is also possible that the Au liquid catalyst droplets are not as efficient at accommodating CdSe vapor when the substrate temperature does not correspond to the ideal preferred vapor concentration ratio of CdS to CdSe.

5.3.4. Effect of CdSe Source Temperature

Moving the CdSe source upstream to effectively lower its temperature was achieved by withdrawing the source dispersion tube though its port in the dual port configuration. The ultra-torr vacuum fitting o-ring provided a sliding seal that permitted translational motion while still maintaining vacuum pressure within the CVD system. The dual port configuration linked both source dispersion tubes to the area outside of the furnace, which permitted external manipulation of the source flow and temperature during the growth procedure. This represents a significant improvement over previous experimental designs that utlized unsecured source dispersion tubes contained completely inside the furnace. Dynamic adjustment of the source temperature and flow is a powerful variable available for optimization of this or any growth procedure performed in this system.

The test condition involved maintaining the same CdSe source position during Phase 2 as in Phase 1. The CdSe source remained at its high temperature. The growth resulted in morphology similar to that of the standard condition, with axial growth continuation from Se-rich to S-rich segments. For PL emission as plotted in Figure 48, both main peaks are red-shifted around 20 nm as compared

to the standard condition. Also, a weaker broad peak appears below strong red
peak.
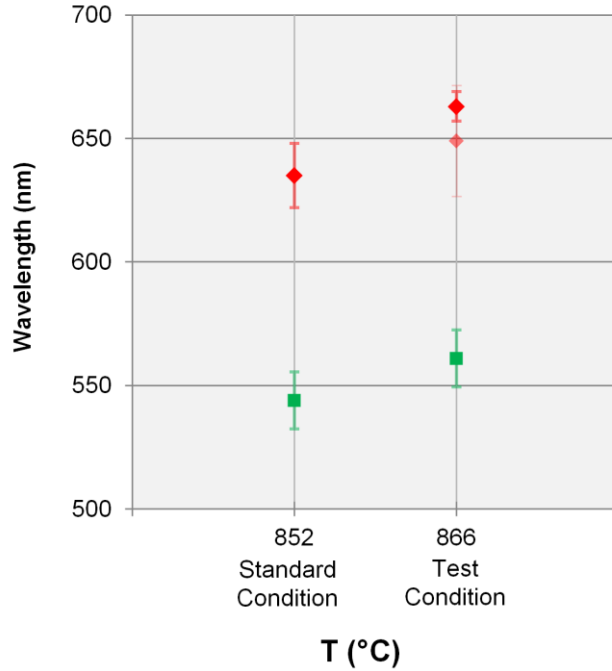
Figure 48. Effect of CdSe source powder temperature during Phase 2.

The effect of lowering the CdSe source temperature is to decrease the
amount of CdSe vapor available for deposition on the substrate by decreasing
amount of CdSe sublimation. Moving CdSe even further upstream disrupted axial
growth continuation between the two segments. Small changes of CdSe source
temperature during Phase 2 can be used to tune the desired final wavelengths of
the two segments. For this work, the wavelength goal for green emission is for it
to be less than 550 nm, so the CdSe source movement in Phase 2 is necessary to
meet that condition.

5.3.5. Effect of CdSe Substrate Temperature

As stated, procedures reported in literature for CdSSe heterostructures did
not optimize the substrate temperature independently; it was directly linked to the

source temperature. As part of the system constructed for the growth in this chapter, use of the cooling fan is an effective and precise method to independently adjust the temperature of the substrate during growth. The temperature can be lowered over 250°C due to the increased convective heat loss by the air flow moving across the exposed quartz tube at the downstream furnace opening. The speed of the cooling fan controls the substrate temperature. This method is much more reproducible for precise temperature changes than mechanical methods, including magnetic loading of the substrate or translation of the entire furnace tube. The mechanical methods serve to relocate the substrate relative to the furnace heating elements within the highly position-sensitive temperature gradient. Small errors in position correspond to large variations in substrate temperature. With the strong dependence of CdSSe alloy composition on substrate temperature, it is essential to use the highly reproducible cooling fan method. This section also addresses the importance of cooling after growth is completed.

The substrate temperature with various cooling fan speeds during Phase 2 was measured using an external thermocouple, and the results are shown in Figure 49. The standard condition (red solid line) utilized the cooling fan at its maximum speed, resulting in a decrease of substrate temperature by 265°C between Phase 1 and Phase 2. Typical growth procedures involved the cooling fan on at 100% during cool down after the furnace was shut off, resulting in an estimated cooling rate of about 40 degrees per minute as measured immediately after completion of the growth procedure. The plot includes one curve that had no cooling fan during

125

post-growth (green dashed-dot). The cooling rate without the fan is only around

15 degrees per minute, significantly slower than the cooling rate with the fan.
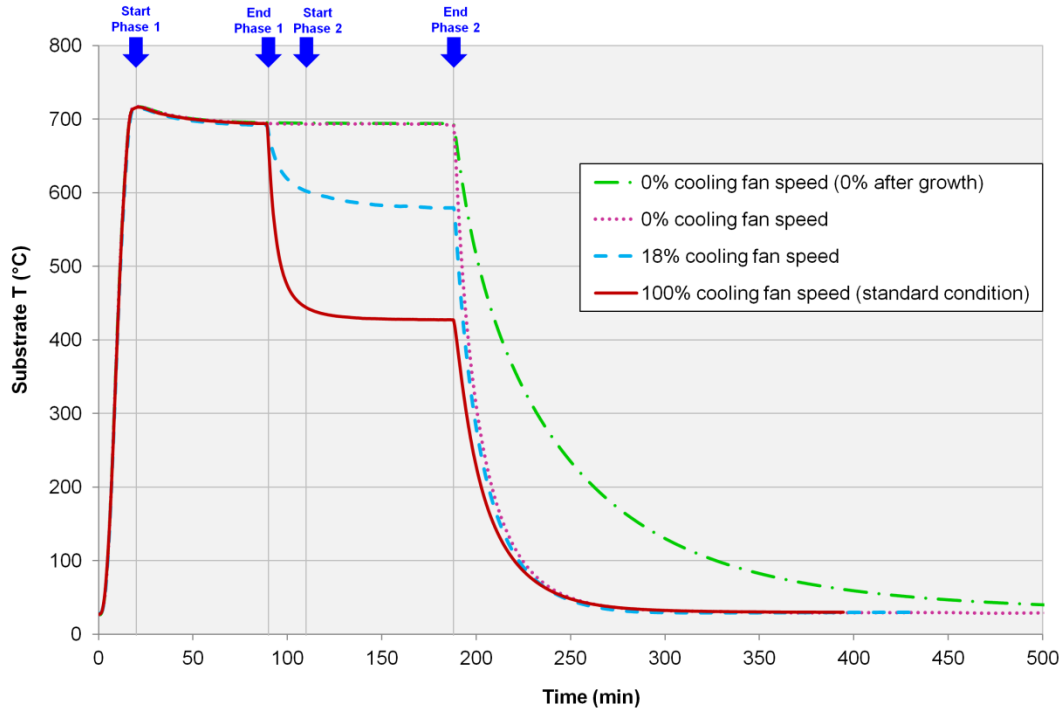
Figure 49. Substrate temperature with time for various cooling fan speeds during Phase 2.

PL was again used to characterize the emission of the resulting nanowires

(Figure 50). The right inset corresponds to the observed wavelengths for no

cooling fan during growth <u>and</u> no cooling fan during cool down. The emission

peaks have significantly broadened and blurred together. As measured between

peak centers, $\Delta\lambda$ is only 16 nm. The peaks are nearly indistinguishable as distinct

colors. As visualized in Figure 49, the furnace takes over 3 hours to cool to room

temperature without the cooling fan, as compared to around 1 hour with the

cooling fan. Ultimately, the substrate remains at elevated temperatures for a much

longer period of time. This additional thermal energy results in higher atomic

motilities, thus faster diffusion processes. Interdiffusion within the wire smoothed

126

out the interface composition gradient to produce alloys with compositions closer to the overall median composition value.
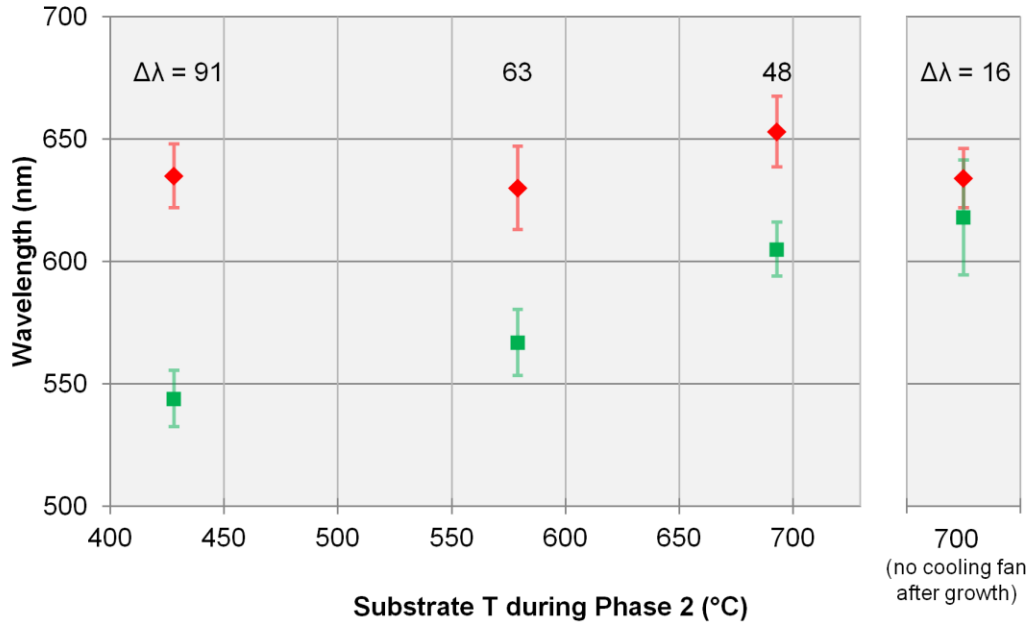
Figure 50. Effect of substrate temperature during Phase 2. In main plot, all experiments had 100% cooling fan during cool down. In right inset, there was no cooling fan during cool down.

Even though the growth parameters were identical to the comparable Phase 2 substrate temperature experiment in the main plot, the wavelength results are very dissimilar because of the difference in post-growth cooling procedure. The cooling procedure is critical to maintaining the interface between segments in the heterostructure nanowire. Because the distances between distinct compositions can be on the order of possible diffusion lengths, nanowires with multiple compositions within a single wire are much more sensitive to cooling than samples with multiple compositions on a single substrate but in well-separated wires.

127

During Phase 2, the composition of the S-rich growth is highly dependent on the substrate temperature and can produce a wide range of wavelengths. The green wavelength shows a variation of approximately 0.2 nm per degree cooling, as measured relative to the maximum substrate temperature during Phase 2 at 693°C. The initially grown Se-rich segment emission is relatively stable to changes in Phase 2 substrate temperature and vapor environment.

In addition to directly changing the substrate temperature, the cooling fan also decreases the amount of available CdSe source vapor above substrate because the temperature at which excess CdSe vapor condenses is moved further upstream from substrate position.

The cooling fan is critical for tuning the wavelength of S-rich growth during Phase 2. Cooling fan speed at 100%, with a substrate temperature of 428°C, produced the most S-rich growth corresponding to a desirable green wavelength below 550 nm. With increasing cooling fan speed, $\Delta\lambda$ reaches a maximum of 91 nm, which represents increasingly distinct colors valuable for broader wavelength coverage in optoelectronic applications. A further decrease in substrate temperature, in order to access possibly increased ranges of S-rich compositions, could be possible by adding multiple or higher power fans. However, the growth achieved here is sufficient for the specific optoelectronic application of interest.

5.4. Device Application: Color-Tunable LED

Using nanowires to establish p-n junctions has led to advances in a wide range of optoelectronic applications including lasers,[144,145] solar cells,[146,147] and

LEDs.[148-153] The CdSSe axial heterostructure nanowires created in this work

demonstrate strong light emission in the visible spectrum, which is highly relevant

to LED and display applications. The device design proposed here for an

electrical injection LED with tunable color is a feasible method to take advantage

of the capabilities enabled by these unique heterostructure nanowires.

In order to provide context for the color tuning potential of the proposed

device, the CIE 1931 color space chromaticity diagram is shown in Figure 51.[154]
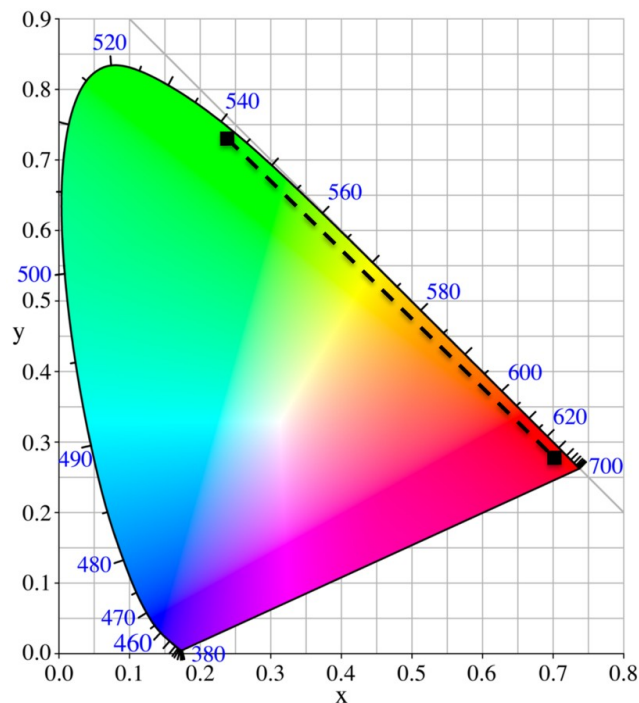
Figure 51. CIE 1931 color space chromaticity diagram. Solid squares correspond to CdSSe axial heterostructure nanowire emission.

This diagram specifies how the human eye experiences light with a given

spectrum, which is essential to consider for LED and display applications. The

outer curved boundary represents monochromatic light with wavelengths shown

in nanometers. All of the colors along any straight line on the diagram can be

created by mixing the two colors at the line endpoints. Specifically, the emission

129

wavelength peak centers resulting from the standard condition of growth, 544 and 635 nm, are shown as solid squares connected by a dashed line. This combination of wavelengths, with a large $\Delta\lambda$ of 91 nm, is appropriate for creating a large portion of the visible spectrum, including green, yellow, orange, and red.

Reports of color control in literature typically refer to separate nanostructures that have distinct alloy compositions or sizes.[124,151,155] Both of these parameters are permanently fixed after growth and processing is completed. Huang *et al.* integrated completely different nanowire materials into an LED array which was capable of generating three spectrally distinct light emission peaks.[149] Yang *et al.* reported individual composition gradient nanowires, each with a different composition corresponding to a fixed, single point near the center of the CIE diagram.[143] The goal of the device proposed here is to enable dynamic color tuning from a single structure during operation.

A device capable of color control must be able to vary the relative intensity of each wavelength that contributes to the perceived output color. The schematic diagram of the proposed CdSSe axial heterostructure nanowire device is shown in Figure 52. There are two separate metallic n-contacts which connect to each segment of the nanowire individually. The nanowire is dispersed flat on a p-doped Si substrate such that its entire length is in contact with the substrate. Regions of electrical insulator material surrounding the nanowire prevent direct contact between the n-contacts and the substrate, which would short out the device. A metallic p-contact pad is deposited on the substrate separate from the nanowire.
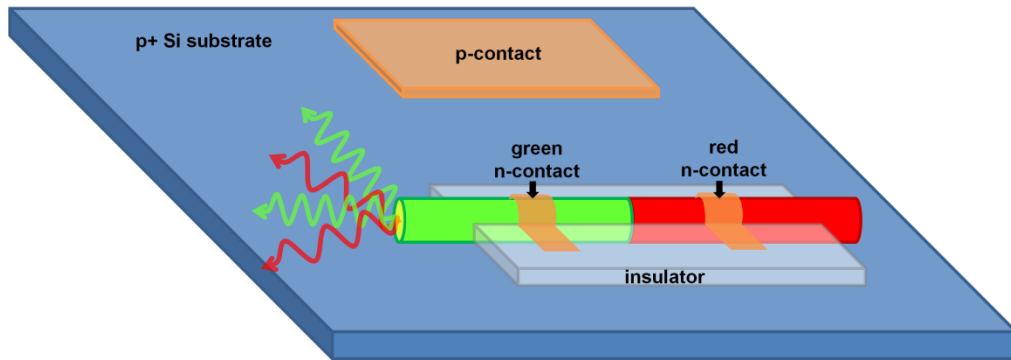
Figure 52: Schematic diagram of the color-tunable LED device based on a CdSSe axial heterostructure nanowire.

In the proposed device, a voltage is applied across the p-contact and n-contacts to inject electrons into the nanowire at the n-contacts and to inject holes into the nanowire from the p-type substrate. The locally generated carriers within the nanowire recombine radiatively to create photons. Because nanowires with smooth sidewalls define an optical cavity, they can act as waveguides.[156] The generated light emission is strongly guided and propagates to the end facets, mimicking a conventional optical fiber. For the specific CdSSe axial heterostructure geometry of this device, the green light that propagates into the red region will be absorbed because the material has a smaller band gap than the energy contained in the light. The larger band gap material of the green segment is transparent to the red light, such that both wavelengths can propagate through the green segment and out the end facet of the axial nanowire as pictured in Figure 52. The waveguiding effect is confirmed by the PL image of the single wire in Figure 44, in which the combination of red and green emission is visible at the end facet of the green segment as yellow color.

The voltages applied to each n-contact can be independently adjusted by the user during device operation to change the color of the output light. A higher voltage provides more carries within the nanowire, which implies a higher radiative recombination rate, resulting in a higher emission intensity of that band edge emission peak. The wavelength value emitted from each segment is constant, but the relative ratio of the two peak intensities can be tuned and controlled dynamically. Also, the overall magnitude of voltage can be used to tailor the brightness. For LED applications, an entire array of nanowires could be connected such that many wires emit in the same way. For a display application, the n-contacts of each wire could be independently controlled such that each nanowire emission represents one pixel in a high-resolution display. For these applications, it is beneficial that the nanowires have minimal composition grading across each segment. The n-contacts on top of the nanowires excite a local region of the wire. If there were many alloy compositions in that region, the emission peaks would be broad and not capable of displaying spectrally pure colors.

5.5. Summary

In summary, a standard growth procedure was established to create CdSSe axial heterostructure nanowires. The procedure makes use of multiple growth parameter variables to alter the source vapor composition and the substrate temperature between Phase 1 and Phase 2. The parameters were isolated to consider their individual contribution to the resulting growth morphology and wavelength as desired for device applications. A mixture of CdS and CdSe source vapors during both growth phases is required to achieve Se-rich nanowire

132

morphology that continued by axial growth to S-rich material. Depending on the growth regime, the growth time can be used to tune the wavelengths of both segments by anion exchange with the vapor environment. The reduction of CdSe flow dramatically affects the wavelength of growth during Phase 2 and is necessary to continue growth of S-rich material. The CdSe source temperature exhibited a minor influence on the resulting wavelengths of both segments. The substrate temperature during Phase 2 is the most critical variable for tuning the CdSSe alloy composition. The impressive ability to incorporate segments of distinct composition material within a single nanowire can be expanded in the future to include a blue light emission material for a wider range of color coverage, represented by a triangular area on the CIE diagram instead of a single line.

Chapter 6

CONCLUSIONS AND RECOMMENDATIONS FOR FUTURE

RESEARCH

Methods to control the composition of chalcogenide alloy nanowires have been established for spatial variation across a substrate and within individual wires. The material and optical properties of the nanowires have been carefully studied and considered for potential optoelectronic devices. Overall, this dissertation has demonstrated the value of chalocogenide alloy nanowires as interesting structures for materials characterization, while also offering new device functionalities in the field of optoelectronics.

6.1. Conclusions

The identified growth modes for PbS were especially complex due to the spontaneously generated catalyst from the vapor phase. The preference for each growth mode was organized in terms of gas-phase supersaturation. Ultimately, the growth led to PbS wires with efficient radiative recombination in the mid-IR range. Single wire lasing was demonstrated with wavelengths over 4000 nm, longer than any reported wavelength for sub-wavelength wires.

$Cd_xPb_{1-x}S$ metastable alloys were achieved in nanowire form for the first time. Although many growth variables were investigated, the cooling of the substrate after growth was identified as the most critical parameter for alloy composition and structure. Rapid cooling by quenching retained metastable alloy material with compositions up to $x = 0.14$. Gradual cooling permitted phase segregation into distinct Cd-rich and Pb-rich regions. Depending on wire

134

diameter, the phase segregation preferred to occur along different directions. In thinner nanowires and nanobelts, segregation occurred along the axis to form axial heterostructures. In nanowires with larger diameter, the segregation appeared in the radial direction to form core-shell structures. The composition variation in $Cd_xPb_{1-x}S$ alloy nanowires was used to demonstrate band gap tailoring in the mid-IR range.

The CdS-CdSe alloy system was fully exploited for spatial composition variation. CdS_xSe_{1-x} over the entire composition range was grown on a single substrate. The composition changed along the length of the substrate, with a uniform alloy within each nanowire. Through the optimization of growth parameters, the supersaturation was made uniform across the substrate to promote uniform morphology. Subsequent device processing by contact printing preserved the original composition variation. Ordered arrays of high-quality nanowires with band gap variation along the substrate were critical to the demonstration of a variable-wavelength photodetector device.

Moreover, axial heterostructure nanowires were achieved with each structure containing distinct segments of CdSSe alloy material. In the growth process, a relatively subtle change in source vapor composition, in combination with a controllable change in substrate temperature, was established as a successful procedure to generate segments with compositions corresponding to the desired band gaps. As a result of the deliberate growth process, both red and green light emission was observed from single nanowires.

6.2. Future Work

Although the PbS wires grown here were capable of mid-IR lasing at low temperatures by optical pumping, a more useful device would be capable of lasing at room temperature by electrical injection. Further research is required to determine the optimum device design and fabricate an electrically driven mid-IR laser based on the PbS wires achieved in this work.

Band gap tailoring of $Cd_xPb_{1-x}S$ demonstrated for alloys on the Pb-rich side is suitable for use in tunable mid-IR detection. In regard to the proposed broad spectrum solar cell design, it is recommended that future research pursues alternative alloy material systems. Initial results indicate that the band gaps of $Cd_xPb_{1-x}S$ alloy nanowires do not follow a linear interpolation between the two endpoint band gaps. Therefore, even if alloy nanowires with increased x values are achieved, they may not exhibit the required band gaps to achieve the high-efficiency solar cell as simulated.

Sequential probing of three cells within a variable-wavelength photodetector device was completed in this work. In future devices, the number of cells should be increased for better wavelength resolution and larger wavelength range. Furthermore, for complete device functionality, all of the cells should be integrated and calibrated, such that a single broadband light exposure could be characterized over a wide wavelength range in parallel. Multi-spectral detection with no moving parts would permit reliable and stable optoelectronic performance.

Although the desired CdSSe axial heterostructure nanowires were achieved, the yield of desired nanowires relative to the yield of nanobelts was relatively low. Therefore, it is recommended that the growth parameters are further optimized for improved morphology yield, as already completed for other CdSSe growth procedures. As mentioned, the addition of a third segment with blue emission would significantly enhance the color tuning capability, opening the potential for white light emission. Zinc sulfide and zinc selenide are appropriate materials for consideration. Distinct composition segments within a single nanowire offer a general strategy to achieve tunable multi-color or white light emission.

REFERENCES

1. Dick, K. A.; Kodambaka, S.; Reuter, M. C.; Deppert, K.; Samuelson, L.; Seifert, W.; Wallenberg, L. R.; Ross, F. M. The Morphology of Axial and Branched Nanowire Heterostructures. *Nano Lett.* **2007**, *7*, 1817-1822.

2. Maslov, A. V.; Ning, C. Z. Modal Gain in a Semiconductor Nanowire Laser With Anisotropic Bandstructure. *IEEE J. Quantum Elect.* **2004**, *40*, 1389-1397.

3. Kelzenberg, M. D.; Boettcher, S. W.; Petykiewicz, J. A.; Turner-Evans, D. B.; Putnam, M. C.; Warren, E. L.; Spurgeon, J. M.; Briggs, R. M.; Lewis, N. S.; Atwater, H. A. Enhanced Absorption and Carrier Collection in Si Wire Arrays for Photovoltaic Applications. *Nat. Mater.* **2010**, *9*, 239-244.

4. Lagos, N.; Sigalas, M. M.; Niarchos, D. The Optical Absorption of Nanowire Arrays. *Photon. Nanostruct. Fundam. Appl.* **2011**, *9*, 163-167.

5. Galicka, M.; Bukala, M.; Buczko, R.; Kacman, P. Modelling the Structure of GaAs and InAs Nanwires. *J. Phys.: Condens. Matter* **2008**, *20*, 454226.

6. Diao, J.; Gall, K.; Dunn, M. L. Surface-Stress-Induced Phase Transformation in Metal Nanowires. *Nature Mater.* **2003**, *2*, 656-660.

7. Xiang, H. J.; Wei, S. H.; Da Silva, J. L. F.; Li, J. Strain Relaxation and Band-Gap Tunability in $In_xGa_{1-x}N$. *Phys. Rev. B* **2008**, *78*, 193301.

8. Nasibov, A. S.; Korostelin, Y. V.; Shapkin, P. V.; Suslina, L. G.; Fedorov, D. L.; Markov, L. S. Exciton Luminescence in Ideal Solid Solutions ($Zn_xCd_{1-x}Se$ System, $0 < x < 1$). *Solid State Commun.* **1989**, *71*, 867-869.

9. Shan, C. X.; Liu, Z.; Ng, C. M.; Hark, S. K. $Zn_xCd_{1-x}Se$ Alloy Nanowires Covering the Entire Compositional Range Grown by Metalorganic Chemical Vapor Deposition. *Appl Phys. Lett*. **2005**, *87*, 033108.

10. Ho, I.; Stringfellow, G. B. Solid Phase Immiscibility in GaInN. *Appl. Phys. Lett*. **1996**, *69*, 2701-2703.

11. Caetano, C.; Teles, L. K.; Marques, M.; Pino, A. D.; Ferreira, L. G. Phase Stability, Chemical Bonds, and Gap Bowing of $In_xGa_{1-x}N$ Alloys:

Comparison Between Cubic and Wurtzite Stuctures. *Phys. Rev. B* **2006**, *74*, 045215.

12. Bartel, T. P.; Specht, P.; Ho, J. C.; Kisielowski, C. Phase Separation in In$_x$Ga$_{1-x}$N. *Phil. Mag.* **2007**, *87*, 1983-1998.

13. Singh, R.; Doppalapudi, D.; Moustakas, T. D.; Romano, L. T. Phase Separation in InGaN Thick Films and Formation of InGaN/GaN Double Heterostructures in the Entire Alloy Composition. *Appl. Phys. Lett.* **1997**, *70*, 1089-1091.

14. Tabata, A.; Teles, L. K.; Scolfaro, L. M. R.; Leite, J. R.; Kharchenko, A.; Frey, T.; As, D. J.; Schikora, D.; Lischka, K.; Furthmuller, J.; Bechstedt, F. Phase Separation Suppression in InGaN Epitaxial Layers Due to Biaxial Strain. *Appl. Phys. Lett.* **2002**, *80*, 769-771.

15. Kuykendall, T.; Ulrich, P.; Aloni, S.; Yang, P. Complete Composition Tunability of InGaN Nanowires Using a Combinatorial Approach. *Nature Mater.* **2007**, *6*, 951-956.

16. Pendyala, C.; Jasinski, J. B.; Kim, J. H.; Vendra, V. K.; Linsenkov, S.; Menon, M.; Sunkara, M. K. Nanowires as Semi-Rigid Substrates for Growth of Thick, In$_x$Ga$_{1-x}$N (x > 0.4) Epi-Layers Without Phase Segregation for Photoelectrochemical Water Splitting. *Nanoscale* **2012** *4*, 6269-6275.

17. Ertekin, E.; Greaney, P. A.; Chrzan, D. C.; Sands, T. D. Equilibrium Limits of Coherency in Strained Nanowire Heterostructures. *J. Appl. Phys.* **2005**, *97*, 114325.

18. Glas, F. Critical Dimensions for the Plastic Relaxation of Strained Axial Heterostructures in Free-Standing Nanowires. *Phys. Rev. B* **2006**, *74*, 121302.

19. Kobayashi, N. P.; Logeeswaran, V. J.; Islam, M. S.; Li, X.; Straznicky, J.; Wang, S. Y.; Williams, R. S.; Chen, Y. Hydrogenated Microcrystalline Silicon Electrodes Connected by Indium Phosphide Nanowires. *Appl. Phys. Lett.* **2007**, *91*, 113116.

20. Logeeswaran, V. J.; Sarkar, A.; Islam, M. S.; Kobayashi, N. P.; Straznicky, J.; Li, X.; Wu, W.; Mathai, S.; Tan, M. R. T.; Wang, S. Y.; Williams, R. S. A 14-ps Full Width at Half Maximum High-Speed Photoconductor Fabricated with Intersecting InP Nanowires on an Amorphous Surface. *Appl. Phys. A*, *Mater. Sci. Process.* **2008**, *91*, 1-5.

21. Grego, S.; Gilchrist, K. H.; Kim, J. Y.; Kwon, M. K.; Islam, M. S. Waveguide-Integrated Nanowire Photoconductors on a Non-Single Crystal Surface. *Proc. SPIE - Int. Soc. Opt. Eng*. **2009**, *7406*, 74060B.

22. Wagner, R. S.; Ellis, W. C. Vapor-Liquid-Solid Mechanism of Single Crystal Growth. *Appl. Phys. Lett*. **1964**, *4*, 89-90.

23. Kolasinski, K. W. Catalytic Growth of Nanowires: Vapor-Liquid-Solid, Vapor-Solid-Solid, Solution-Liquid-Solid and Solid-Liquid-Solid Growth. *Curr. Opin. Solid St. M*. **2006**, *10*, 182-191.

24. Bakkers, E. P.; Borgstrom, M. T.; Verheijen, M. A. Epitaxial Growth of III-V Nanowires on Group IV Substrates. *MRS Bull*. **2007**, *32*, 117-122.

25. Wacaser, B. A.; Dick, K. A.; Johansson, J.; Borgström, M. T.; Deppert, K.; Samuelson, L. Preferential Interface Nucleation: An Expansion of the VLS Growth Mechanism for Nanowires. *Adv. Mater*. **2009**, *21*, 153-165.

26. Ross, F. M. Controlling Nanowire Structures Through Real Time Growth Studies. *Rep. Prog. Phys*. **2010**, *73*, 114501.

27. Kar, S.; Chaudhuri, S. Shape Selective Growth of CdS One-Dimensional Nanostructures by a Thermal Evaporation Process. *J. Phys. Chem. B* **2006**, *110*, 4542-4547.

28. Blocher, J. M. Structure/Property/Process Relationships in Chemical Vapor Deposition CVD. *J. Vac. Sci. Technol*. **1974**, *11*, 680-686.

29. Pan, A.; Liu, R.; Sun, M.; Ning, C. Z. Spatial Composition Grading of Quaternary ZnCdSSe Alloy Nanowires with Tunable Light Emission between 350 and 710 nm on a Single Substrate. *ACS Nano* **2010**, *4*, 671-680.

30. Philipose, U.; Yang, S.; Xu, T.; Ruda, H. E. Origin of the Red Luminescence Band in Photoluminescence Spectra of ZnSe Nanowires. *Appl. Phys. Lett*. **2007**, *90*, 063103.

31. Dailey, E.; Madras, P.; Drucker, J. Au on Vapor-Liquid-Solid Grown Si Nanowires: Spreading of Liquid AuSi from the Catalytic Seed. *J. Appl. Phys*. **2010**, *108*, 064320.

32. Allen, J. E.; Hemesath, E. R.; Perea, D. E.; Lensch-Falk, J. L.; Li, Z. Y.; Yin, F.; Gass, M. H.; Wang, P.; Bleloch, A. L.; Palmer, R. E.; Lauhon, L. J. High-Resolution Detection of Au Catalyst Atoms in Si Nanowires. *Nature Nanotech*. **2008**, *3*, 168-173.

33. Sun, M. H.; Joyce, H. J.; Gao, Q.; Tan, H. H.; Jagadish, C.; Ning, C. Z. Removal of Surface States and Recovery of Band-Edge Emission in InAs Nanowires through Surface Passivation. *Nano Lett*. **2012**, *12*, 3378-3384.

34. Vegard, L. Die Konstitution der Mischkristalle und die Raumfullung der Atome. *Z. Phys*. **1921**, *5*, 17-26.

35. Bakueva, L.; Gorelikov, I.; Musikhin, S.; Zhao, X. S.; Sargent, E. H.; Kumacheva, E. PbS Quantum Dots with Stable Efficient Luminescence in the Near-IR Spectral Range. *Adv. Mater.* **2004**, *16*, 926-929.

36. Pentia, E.; Pintilie, L.; Matei, I.; Botila, T.; Pintilie, I. Combined Chemical-Physical Methods for Enhancing IR Photoconductive Properties of PbS Thin Films. *Infrared Phys.Techn.* **2003**, *44*, 207-211.

37. Bakueva, L.; Musikhin, S.; Hines, M. A.; Chang, T. W. F.; Tzolov, M.; Scholes, G. D.; Sargent, E. H. Size-Tunable Infrared (1000-1600nm) Electroluminescence from PbS Quantum-Dot Nanocrystals in a Semiconducting Polymer. *Appl. Phys. Lett.* **2003**, *82*, 2895-2897.

38. Sukhovatkin, V.; Musikhin, S.; Gorelikov, I.; Cauchi, S.; Bakueva, L.; Kumacheva, E.; Sargent, E. H. Room-Temperature Amplified Spontaneous Emission at 1300 nm in Solution-Processed PbS Quantum-Dot Films. *Opt. Lett.* **2005**, *30*, 171-173.

39. Tamulaitis, G.; Gulbinas, V.; Kodis, G.; Dementjev, A.; Valkunas, L.; Motchalov, I.; Raaben, H. Optical Nonlinearities of Glass Doped with PbS Nanocrystals. *J. Appl. Phys.* **2000**, *88*, 178-182.

40. Dantas, N. O.; Qu, F.; Silva, R. S.; Morais, P. C. Anti-Stokes Photoluminescence in Nanocrystal Quantum Dots. *J. Phys. Chem. B* **2002**, *106*, 7453-7457.

41. Koguchi, N; Takahashi, S. Double-Heterostructure $Pb_{1-x-y}Cd_xSr_yS/PbS/Pb_{1-x-y}Cd_xSr_yS$ Lasers Grown by Molecular Beam Epitaxy. *Appl. Phys. Lett.* **1991**, *58*, 799-800.

42. Plass, R.; Pelet, S.; Krueger, J.; Gratzel, M.; Bach, U. Quantum Dot Sensitization of Organic-Inorganic Hybrid Solar Cells. *J. Phys. Chem. B* **2002**, *106*, 7578-7580.

43. Dhere, N. G. Appropriate Materials and Preparation Techniques for Polycrystalline-Thin-Film Thermophotovoltaic Cells. *AIP Conf. Proc.* **1997**, *401*, 423-442.

44. Yablonovitch, E.; Kane, E. O. Band Structure Engineering of Semiconductor Lasers for Optical Communications. *J. Lightwave Techol.* **1988**, *6*, 1292-1299.

45. Ishida, A.; Ohashi, T.; Wang, S.; Tsuchiya, T.; Ishino, K.; Inoue, Y.; Fujiyasu, H. PbSnCaTe Films and PbSnCaTe/PbSnTe Superlattices Prepared by Molecular Beam Epitaxy. *Jpn. J. Appl. Phys*. **2002**, *41*, 3655-3657.

46. Ge, J. P.; Wang, J.; Zhang, H. X.; Wang, X.; Peng, Q.; Li, Y. D. Orthogonal PbS Nanowire Arrays and Networks and Their Raman Scattering Behavior. *Chem. Eur. J.* **2005**, *11*, 1889-1894.

47. Afzaal, M.; O'Brien, P. Silica Coated PbS Nanowires. *J. Mater. Chem.* **2006**, *16*, 1113-1115.

48. Bierman, M. J.; Lau, Y. K. A.; Jin, S. Hyperbranched PbS and PbSe Nanowires and the Effect of Hydrogen Gas on Their Synthesis. *Nano Lett.* **2007**, *7*, 2907-2912.

49. Bierman, M. J.; Lau, Y. K. A.; Kvit, A. V.; Schmitt, A. L.; Jin, S. Dislocation-Driven Nanowire Growth and Eshelby Twist. *Science* **2008**, *230*, 1060-1063.

50. Lau, Y. K. A.; Chernak, D. J.; Bierman, M. J.; Jin, S. Formation of PbS Nanowire Pine Trees Driven by Screw Dislocations. *J. Am. Chem. Soc*. **2009**, *131*, 16461-16471.

51. Lau, Y. K. A.; Chernak, D. J.; Bierman, M. J.; Jin, S. Epitaxial Growth of Hierarchical PbS Nanowires. *J. Mater. Chem.* **2009**, *19*, 934-940.

52. Jang, S. Y.; Song, Y. M.; Kim, H. S.; Cho, Y. J.; Seo, Y. S.; Jung, G. B.; Lee, C. W.; Park, J.; Jung, M.; Kim, J.; Kim, B.; Kim, J. G.; Kim, Y. J. Three Synthetic Routes to Single-Crystalline PbS Nanowires with Controlled Growth Directions and Their Electrical Transport Properties. *ACS Nano* **2010**, *4*, 2391-2401.

53. Wu, H.; Yang, Y.; Oh, E.; Lai, F.; Yu, D. Direct Synthesis of High-Density Lead Sulfide Nanowires on Metal Thin Films Towards Efficient Infrared Light Conversion. *Nanotechnology* **2012**, *23*, 265602.

54. Wang, S.; Pan, A.; Yin, H.; He, Y.; Lei, Y.; Xu, Z.; Zou, B. Synthesis of PbS Microcrystals *via* a Hydrothermal Process. *Mater. Lett*. **2006**, *60*, 1242-1246.

55. Kuang, D.; Xu, A.; Fang, Y.; Liu, H.; Frommen, C.; Fenske, D. Surfactant-Assisted Growth of Novel PbS Dendritic Nanostructures *via* Facile Hydrothermal Process. *Adv. Mater.* **2003**, *15*, 1747-1750.

56. Chen, J.; Chen, L.; Wu, L. M. The Solventless Syntheses of Unique PbS Nanowires of X-Shaped Cross Sections and the Cooperative Effects of Ethylenediamine and a Second Salt. *Inorg. Chem.* **2007**, *46*, 8038-8043.

57. Ding, B.; Shi, M.; Chen, F.; Zhou, R.; Deng, M.; Wang, M.; Chen, H. Shape-Controlled Syntheses of PbS Submicro-/Nano-Crystals *via* Hydrothermal Method. *J. Cryst. Growth* **2009**, *311*, 1533-1538.

58. Saraidarov, T.; Reisfeld, R.; Sashchiuk, A.; Lifshitz, E. Synthesis and Characterization of PbS Nanorods and Nanowires. *Physica E* **2007**, *37*, 173-177.

59. Wang, Z.; Zhao, B.; Zhang, F.; Mao, W.; Qian, G.; Fan, X. Novel Single-Crystal PbS Nanowires Directed by [200]. *Mater. Lett.* **2007**, *61*, 3733-3735.

60. Yong, K. T.; Sahoo, Y.; Choudhury, K. R.; Swihart, M. T.; Minter, J. R.; Prasad, P. N. Control of the Morphology and Size of PbS Nanowires using Gold Nanoparticles. *Chem. Mater.* **2006**, *18*, 5965-5972.

61. Patla, I.; Acharya, S.; Zeiri, L.; Israelachvili, J.; Efrima, S.; Golan, Y. Synthesis, Two-Dimensional Assembly, and Surface Pressure-Induced Coalescence of Ultranarrow PbS Nanowires. *Nano Lett.* **2007**, *7*, 1459-1462.

62. Onicha, A. C.; Petchsang, N.; Kosel, T. H.; Kuno, M. Controlled Synthesis of Compositionally Tunable Ternary PbS_xSe_{1-x} as Well as Binary PbSe and PbS Nanowires. *ACS Nano* **2012**, *6*, 2833-2843.

63. Xu, F.; Ma, X.; Gerlein, L. F.; Cloutier, S. G. Designing and Building Nanowires: Directed Nanocrystal Self-Assembly into Radically Branched and Zigzag PbS Nanowires. *Nanotechnology* **2011**, *22*, 265604.

64. Gao, F.; Lu, Q.; Liu, X.; Yan, Y.; Zhao, D. Controlled Synthesis of Semiconductor PbS Nanocrystals and Nanowires Inside Mesoporous Silica SBA-15 Phase. *Nano Lett.* **2001**, *1*, 743-748.

65. Mukherjee, P. K.; Chatterjee, K.; Chakravorty, D. Semiconductor to Metal Transition in PbS Nanowires Grown in Mica Channels. *Phys. Rev. B* **2006**, *73*, 035414.

66.   Wu, C.; Shi, J. B.; Chen, C. J.; Lin, J. Y. Synthesis and Optical Properties of Ordered 30 nm PbS Nanowire Arrays Fabricated into Sulfuric Anodic Alumina Membrane. *Mater. Lett.* **2006**, *60*, 3618-3621.

67.   Patel, A. R.; Sangwal, K. Growth and Etching of PbS Whiskers from the Vapour Phase. *J. Cryst. Growth* **1971**, *8*, 282-284.

68.   Nichols, P. L.; Sun, M.; Ning, C. Z. Influence of Supersaturation and Spontaneous Catalyst Formation on the Growth of PbS Wires: Toward a Unified Understanding of Growth Modes. *ACS Nano* **2011**, *5*, 8730-8738.

69.   Jana, S.; Goswami, S.; Nandy, S.; Chattopadhyay, K. K. Synthesis of Tetrapod like PbS Microcrystals by Hydrothermal Route and its Optical Characterization. *J. Alloy Compd.* **2009**, *481*, 806-810.

70.   Mattila, M.; Hakkarainen, T.; Lipsanen, H.; Jiang, H.; Kauppinen, E. I. Catalyst-Free Growth of In(As)P Nanowires on Silicon. *Appl. Phys. Lett.* **2006**, *89*, 063119.

71.   Colombo, C.; Spirkoska, D.; Frimmer, M.; Abstreiter, G.; Fontcuberta i Morral, A. Ga-Assisted Catalyst-Free Growth Mechanism of GaAs Nanowires by Molecular Beam Epitaxy. *Phys. Rev. B* **2008**, *77*, 155326.

72.   Plissard, S.; Dick, K. A.; Larrieu, G.; Godey, S.; Addad, A.; Wallart, X.; Caroff, P. Gold-Free Growth of GaAs Nanowires on Silicon: Arrays and Polytypism. *Nanotech.* **2010**, *21*, 385602.

73.   Vaddiraju, S.; Sunkara, M. K.; Chin, A. H.; Ning, C. Z.; Dholakia, G. R.; Meyyappan, M. Synthesis of Group III Antimonide Nanowires. *J. Phys. Chem. C* **2007**, *111*, 7339-7347.

74.   Ye, C.; Fang, X.; Hao, Y.; Teng, X.; Zhang, L. Zinc Oxide Nanostructures: Morphology Derivation and Evolution. *J. Phys. Chem. B* **2005**, *109*, 19758-19765.

75.   Botor, J.; Milkowska, G.; Konieczny, J. Vapour Pressure and Thermodynamics of PbS. *Thermochim. Acta* **1989**, *137*, 269-279.

76.   Dalven, R. Electronic Structure of PbS, PbSe, and PbTe. *Solid State Phys.* **1974**, *28*, 179-224.

77.   Novikova, S. I.; Abrikosov, N. K. Investigation of the Thermal Expansion of Lead Chalcogenides. *Soviet Phys. Solid State* **1964**, *5*, 1397-1398.

78. Wilkinson, V. A.; Adams, A. R. Pressure Effects on the Energy Band Parameters of AlGaAs. In *Properties of Aluminium Gallium Arsenide*; Adachi, S, Ed.; INSPEC: London, 1993, p 82.

79. Paul, W. High Pressure in Semiconductor Physics: A Historical Overview. In *Semiconductors and Semimetals*, vol. 54; Paul, W.; Suski, T., Eds.; Academic: San Diego, 1998, p 33.

80. Preier, H. Recent Advances in Lead-Chalcogenide Diode Lasers. *Appl. Phys.* **1979**, *20*, 189-206.

81. Chin, A. H.; Vaddiraju, S.; Maslov, A. V.; Ning, C. Z.; Sunkara, M. K.; Meyyappan, M. Near-Infrared Semiconductor Subwavelength-Wire Lasers. *Appl. Phys. Lett.* **2006**, *88*, 163115.

82. Bethke, P. M.; Barton, P. B. Sub-Solidus Relations in the System PbS-CdS. *Am. Mineral.* **1971**, *56*, 2034-2039.

83. Sood, A. K.; Wu, K.; Zemel, J. N. Metastable $Pb_{1-x}Cd_xS$ Epitaxial Films: I. Growth and Physical Properties. *Thin Solid Films* **1978**, *48*, 73-86.

84. Calawa, A. R.; Morczkowski, J. A.; Harman, T. C. Preparation and Properties of $Pb_{1-x}Cd_xS$. *J. Electron. Mater.* **1972**, *1*, 191-201.

85. Dawar, A. L.; Taneja, O. P.; Kumar, P.; Mathur, P. C. Electrical Transport Properties of p-Type $Pb_{1-x}Cd_xS$ Epitaxial Thin Films. *Thin Solid Films* **1981**, *79*, 185-191.

86. Rabinovich, E.; Wachtel, E.; Hodes, G. Chemical Bath Deposition of Single-Phase (Pb,Cd)S Solid Solutions. *Thin Solid Films* **2008**, *517*, 737-744.

87. Ivanov, P. N.; Markov, V. F.; Maskaeva, L. N. Role of the Size Effect in Hydrochemical Deposition of PbS-CdS Solid-Solution Films. *Inorg. Mater.* **2005**, *41*, 1135-1138.

88. Mohammed, M. A.; Mousa, A. M.; Ponpon, J. P. Optical and Optoelectric Properties of PbCdS Ternary Thin Films Deposited by CBD. J. *Semicond. Sci. Tech.* **2009**, *9*, 117-123.

89. Nayak, B. B.; Acharya, H. N. Characterization of Chemically Deposited $Pb_{1-x}Cd_xS$ Films by Scanning Electron Microscopy. *J. Mater. Sci. Lett.* **1985**, *4*, 651-652.

90. Pentia, E.; Draghici, V.; Sarau, G.; Bereu, B.; Pintilie, L.; Sava, F.; Popescu, M. Structural, Electrical, and Photoelectrical Properties of

$Cd_xPb_{1-x}S$ Thin Films Prepared by Chemical Bath Deposition. *J. Electrochem. Soc.* **2004**, *151*, G729-G733.

91. Ounissi, A.; Ouddai, N.; Achour, S. Optical Characterisation of Chemically Deposited $Pb_{(1-x)}Cd_xS$ Films and a $Pb_{1-x}Cd_xS(n)/Si(p)$ Heterojunction. *Eur. Phys. J. Appl. Phys.* **2007**, *37*, 241-245.

92. Ounissi, A.; Ouddai, N. Chemically Deposited Heterojunction Solar Cells $Pb_{(1-x)}Cd_{(x)}S(n)/Si(p)$. *Int. J. Nanosci.* **2010**, *9*, 599-604.

93. Upadhyaya, H. M.; Chandra, S. Chemical-Bath Deposition of Band-Gap-Tailored $Cd_xPb_{1-x}S$ Films. *J. Mater. Sci* **1994**, *29*, 2734-2740.

94. Susa, K.; Kobayashi, T.; Taniguchi, S. High-Pressure Synthesis of Rock-Salt Type CdS Using Metal Sulfide Additives. *J. Solid State Chem.* **1980**, *33*, 197-202.

95. Reddy, G. B.; Pandya, D. K.; Chopra, K. L. Solution Grown $(PbS)_{1-x}$-$(CdS)_x$ Composite Selective Surfaces. *Sol. Energy Mater.* **1987**, *15*, 383-390.

96. Xu, X. C.; Tao, Y. R. Growth of CdS Nanowires by Physical Vapor Deposition. *J. Cryst. Growth* **2002**, *242*, 309-312.

97. Hoffman, D. M.; Singh, B.; Thomas, J. H. *Handbook of Vacuum Science and Technology*; Academic Press: San Diego, 1998; pp 17-29.

98. Honig, R. E.; Kramer, D. A. Vapor Pressure Data for the Solid and Liquid Elements. *RCA Rev.* **1969**, *30*, 285-305.

99. Sood, A. K.; Zemel, J. N. Metastable $Pb_{1-x}Cd_xS$ Epitaxial Films: III. Optical Properties. *J. Appl. Phys.* **1978**, *49*, 5292-5294.

100. Kwon, S. J.; Choi, Y. J.; Park, J. H.; Hwang, I. S.; Park, J. G. Structural and Optical Properties of CdS_xSe_{1-x} Nanowires. *Phys. Rev. B* **2005**, *72*, 205312.

101. Gebhart, W.; Schotz, G. Properties of Wide Band Gap Semiconductors. In *EMIS Datareviews Series*, No. 17; Bhargava, R, Ed.; INSPEC: London, 1997, p 113.

102. Zolotov, S. I.; Trofimova, N. B.; Yunovich, A. E. Photoluminescence of Films of $Pb_{1-x}Cd_xS$ Ternary Solid Solutions. *Sov. Phys. Semicond.* **1984**, *18*, 393-395.

103. Shockley, W.; Queisser, H. J. Detailed Balance Limit of Efficiency of p-n Junction Solar Cells. *J. Appl. Phys.* **1961**, *32*, 510-519.

104. Henry, C. H. Limiting Efficiencies of Ideal Single and Multiple Energy Gap Terrestrial Solar Cells. *J. Appl. Phys*. **1980**, *51*, 4494-4500.

105. Caselli, D. A.; Ning, C. Z. High-Performance Laterally-Arranged Multiple-Bandgap Solar Cells Using Spatially Composition-Graded $Cd_xPb_{1-x}S$ Nanowires on a Single Substrate: A Design Study. *Opt. Express* **2011**, *19*, A686-A694.

106. Pan, A.; Zhou, W.; Leong, E. S. P.; Liu, R.; Chin, A. H.; Zou, B.; Ning, C. Z. Continuous Alloy-Composition Spatial Grading and Superbroad Wavlength-Tunable Nanowire Lasers on a Single Chip. *Nano Lett*. **2009**, *9*, 784-788.

107. Takahashi, T.; Nichols, P.; Takei, K.; Ford, A. C.; Jamshidi; A.; Wu, M. C.; Ning, C. Z.; Javey, A. Contact Printing of Compositionally Graded CdS_xSe_{1-x} Nanowire Parallel Arrays for Tunable Photodetectors. *Nanotechnology* **2012**, *23*, 045201.

108. Javey, A.; Nam, S.; Friedman, R. S.; Yan, H.; Lieber, C. M. Layer-by-layer Assembly of Nanowires for Three-Dimensional, Multifunctional Electronics. *Nano Lett*. **2007**, *7*, 773-777.

109. Fan, Z.; Ho, J. C.; Jacobson, Z. A.; Yerushalmi, R.; Alley, R. L.; Razavi, H.; Javey, A. Wafer-Scale Assembly of Highly Ordered Semiconductor Nanowire Arrays by Contact Printing. *Nano Lett*. **2008**, *8*, 20-25.

110. Takahashi, T.; Takei, K.; Ho, J. C.; Chueh, Y.; Fan, Z.; Javey, A. Monolayer Resist for Patterned Contact Printing of Aligned Nanowire Arrays. *J. Am. Chem. Soc*. **2009**, *131*, 2102-2103.

111. Ford, A. C.; Ho, J. C.; Fan, Z.; Ergen, O.; Altoe, V.; Aloni, S.; Razavi, H.; Javey, A. Synthesis, Contact Printing, and Device Characterization of Ni-Catalyzed, Crystalline InAs Nanowires. *Nano Res*. **2008**, *1*, 32-39.

112. Hou, J. J.; Han, N.; Wang, F.; Xiu, F.; Yip, S.; Hui, A. T.; Hung, T.; Ho, J. C. Synthesis and Characterizations of Ternary InGaAs Nanowires by a Two-Step Growth Method for High-Performance Electronic Devices. *ACS Nano* **2012**, *6*, 3624-3630.

113. Fan, Z.; Ho, J. C.; Jacobson, Z. A.; Razavi, H.; Javey, A. Large-Scale, Heterogeneous Integration of Nanowire Arrays for Image Sensor Circuitry. *Proc. Natl. Acad. Sci. U. S. A*. **2008**, *105*, 11066-11070.

114. Hannon, J. B.; Kodambaka, S.; Ross, F. M.; Tromp, R. M. The Influence of the Surface Migration of Gold on the Growth of Silicon Nanowires. *Nature* **2006**, *440*, 69-71.

115. Underwood, E. E. *Quantitative Stereology*; Addison-Wesley: Reading, MA, 1970; pp 34-36.

116. Carlsson, J.O. Chemical Vapor Deposition. In *Handbook of Deposition Technologies for Films and Coatings*, 3rd ed.; Martin, P. M., Ed.; Elsevier: Oxford, 2010; pp 400-459.

117. Ma, C.; Wang, Z. L. Road Map for the Controlled Synthesis of CdSe Nanowires, Nanobelts, and Nanosaws - A Step Towards Nanomanufacturing. *Adv. Mater*. **2005**, *17*, 1-6.

118. Wagner, R. S.; Ellis, W. C.; Jackson, K. A.; Arnold, S. M. Study of the Filamentary Growth of Silicon Crystals from the Vapor. *J. Appl. Phys*. **1964**, *35*, 2993-3000.

119. Mills, K. C. *Thermodynamic Data for Inorganic Sulphides, Selenides and Tellurides*; Butterworths: London, 1974; pp 192-517.

120. Colli, A.; Fasoli, A.; Hofmann, S.; Ducati, C.; Robertson, J.; Ferrari, A. C. Deterministic Shape-Selective Synthesis of Nanowires, Nanoribbons and Nanosaws by Steady-State Vapour-Transport. *Nanotechnology* **2006**, *17*, 1046-1051.

121. Fasoli, A.; Colli, A.; Hofmann, S.; Ducati, C.; Robertson, J.; Ferrari, A. C. Shape-Selective Synthesis of II-VI Semiconductor Nanowires. *Phys. Status Solidi B* **2006**, *243*, 3301-3305.

122. Merten, U.; Bell, W. E. The Transpiration Method. In *The Characterization of High-Temperature Vapors*; Margrave, J. L., Ed.; Wiley: New York, 1967; pp 91-114.

123. Kind, H.; Yan, H.; Messer, B.; Law, M.; Yang, P. Nanowire Ultraviolet Photodetectors and Optical Switches. *Adv. Mater*. **2002**, *14*, 158-160.

124. Choi, Y. J.; Hwang, I. S.; Park, J. H.; Nahm, S.; Park, J. G. Band Gap Modulation in CdS_xSe_{1-x} Nanowires Synthesized by a Pulsed Laser Ablation with the Au Catalyst. *Nanotechnology* **2006**, *17*, 3775-3778

125. Singh, A.; Li, X.; Protasenko, V.; Galantai, G.; Kuno, M.; Xing, H.; Jena, D. Polarization-Sensitive Nanowire Photodetectors Based on Solution-Synthesized CdSe Quantum-Wire Solids. *Nano Lett*. **2007**, *7*, 2999-3006.

126. Jie, J. S.; Zhang, W. J.; Jiang, Y.; Meng, X. M.; Li, Y. Q.; Lee, S. T. Photoconductive Characteristics of Single-Crystal CdS Nanoribbons. *Nano Lett*. **2006**, *6*, 1887-1892.

127. Jiang, Y.; Zhang, W. J.; Jie, J. S.; Meng, X. M.; Fan, X.; Lee, S. T. Photoresponse Properties of CdSe Single-Nanoribbon Photodetectors. *Adv. Funct. Mater*. **2007**, *17*, 1795-1800.

128. Kung, S. C.; van der Veer, W. E.; Yang, F.; Donavan, K. C.; Penner, R. M. 20 μs Photocurrent Response from Lithographically Patterned Nanocrystalline Cadmium Selenide Nanowires. *Nano Lett*. **2010**, *10*, 1481-1485.

129. Lieber, C. M.; Wang, Z. L. Functional Nanowires. *MRS Bull*. **2007**, *32*, 99-108.

130. Hu, J.; Bando, Y.; Golberg, D. Novel Semiconducting Nanowire Heterostructures: Synthesis, Properties and Applications. *J. Mater. Chem*. **2009**, *19*, 330-343.

131. Clark, T. E.; Nimmatoori, P.; Lew, K. K.; Pan, L.; Redwing, J. M.; Dickey, E. C. Diameter Dependent Growth Rate and Interfacial Abruptness in Vapor-Liquid-Solid $Si/Si_{1-x}Ge_x$ Heterostructure Nanowires. *Nano Lett*. **2008**, *8*, 1246-1252.

132. Wen, C. Y.; Reuter, M. C.; Bruley, J.; Tersoff, J.; Kodambaka, S.; Stach, E. A.; Ross, F. M. Formation of Compositionally Abrupt Axial Heterojunctions in Silicon-Germanium Nanowires. *Science* **2009**, *326*, 1247-1250.

133. Perea, D. E.; Li, N.; Dickerson, R. M.; Misra, A.; Picraux, S. T. Controlling Heterojunction Abruptness in VLS-Grown Semiconductor Nanowires via In Situ Catalyst Alloying. *Nano Lett*. **2011**, *11*, 3117-3122.

134. Tersoff, J. Dislocations and Strain Relief in Compositionally Graded Layers. *Appl. Phys. Lett*. **1993**, *62*, 693-695.

135. Pan, A.; Yang, H.; Liu, R.; Yu, R.; Zou, B.; Wang, Z. Color-Tunable Photoluminescence of Alloyed CdS_xSe_{1-x} Nanobelts. *J. Am. Chem. Soc*. **2005**, *127*, 15692-15693.

136. Pan, A.; Liu, R.; Wang, F.; Xie, S.; Zou, B.; Zacharias, M.; Wang, Z. L. High-Quality Alloyed CdS_xSe_{1-x} Whiskers as Waveguides with Tunable Stimulated Emission. *J. Phys. Chem. B* **2006**, *110*, 22313-22317.

137. Pan, A.; Yang, H.; Yu, R.; Zou, B. Fabrication and Photoluminescence of High-Quality Ternary CdSSe Nanowires and Nanoribbons. *Nanotechnology* **2006**, *17*, 1083-1086.

138. Kim, Y. L.; Jung, J. H.; Kim, K. H.; Yoon, H. S.; Song, M. S.; Bae, S, H.; Kim, Y. The Growth and Optical Properties of CdSSe Nanosheets. *Nanotechnology* **2009**, *20*, 095605.

139. Kim, Y. L.; Jung, J. H.; Yoon, H. S.; Song, M. S.; Bae, S. H.; Kim, Y.; Chen, Z. G.; Zou, J.; Joyce, H. J.; Gao, Q.; Tan, H. H.; Jagadish, C. CdS/CdSe Lateral Heterostructure Nanobelts by a Two-Step Physical Vapor Transport Method. *Nanotechnology* **2010**, *21*, 145602.

140. Xu, J.; Ma, L.; Guo, P.; Zhuang, X.; Zhu, X.; Hu, W.; Duan, X.; Pan, A. Room-Temperature Dual-Wavelength Lasing from Single-Nanoribbon Lateral Heterostructures. *J. Am. Chem. Soc*. **2012**, *134*, 12394-12397.

141. Gu, F.; Yang, Z.; Yu, H.; Xu, J.; Wang, P.; Tong, L.; Pan, A. Spatial Bandgap Engineering along Single Alloy Nanowires. *J. Am. Chem. Soc.* **2011**, *133*, 2037-2039.

142. Ouyang, L.; Maher, K. N.; Yu, C. L.; McCarty, J.; Park, H. Catalyst-Assisted Solution-Liquid-Solid Synthesis of CdS/CdSe Nanorod Heterostructures. *J. Am. Chem. Soc*. **2007**, *129*, 133-138.

143. Yang, Z.; Xu, J.; Wang, P.; Zhuang, X.; Pan, A.; Tong, L. On-Nanowire Spatial Band Gap Design for White Light Emission. *Nano Lett*. **2011**, *11*, 5085-5089.

144. Duan, X.; Huang, Y.; Agarwal, R.; Lieber, C. M. Single-Nanowire Electrically Driven Lasers. *Nature* **2003**, *421*, 241-245.

145. Qian, F.; Li, Y.; Gradecak, S.; Park, H.; Dong, Y.; Ding, Y.; Wang, Z. L.; Lieber, C. M. Multi-Quantum-Well Nanowire Heterostructures for Wavelength-Controlled Lasers. *Nat. Mater*. **2008**, *7*, 701-706.

146. Huynh, W. U.; Dittmer, J. J.; Alivisatos, A. P. Hybrid Nanorod-Polymer Solar Cells. *Science* **2002**, *295*, 2425-2427.

147. Mohite, A. D.; Perea, D. E.; Singh, S.; Dayeh, S. A.; Campbell, I. H.; Picraux, S. T.; Htoon, H. Highly Efficient Charge Separation and Collection Across in Situ Doped Axial VLS-Grown Si Nanowire p-n Junctions. *Nano Lett.* **2012**, *12*, 1965-1971.

148. Duan, X.; Huang, Y.; Cui, Y.; Wang, J.; Lieber, C. M. Indium Phosphide Nanowires as Building Blocks for Nanoscale Electronic and Optoelectronic Devices. *Nature* **2001**, *409*, 66-69.

149. Huang, Y.; Duan, X.; Lieber, C. M. Nanowires for Integrated Multicolor Nanophotonics. *Small* **2005**, *1*, 142-147.

150. Gudiksen, M. S.; Lauhon, L. J.; Wang, J.; Smith, D. C.; Lieber, C. M. Growth of Nanowire Superlattice Structures for Nanoscale Photonics and Electronics. *Nature* **2002**, *415*, 617-620.

151. Qian, F.; Gradecak, S.; Li, Y.; When, C.; Lieber, C. M. Core/Multishell Nanowire Heterostructures as Multicolor, High-Efficiency Light-Emitting Diodes. *Nano Lett.* **2005**, *5*, 2287-2291.

152. Bao, J.; Zimmler, M. A.; Capasso, F. Broadband ZnO Single-Nanowire Light-Emitting Diode. *Nano Lett*. **2006**, *6*, 1719-1722.

153. Zimmler, M. A.; Bao, J.; Shalish, I.; Yi, W.; Narayanamurti, V.; Capasso, F. A Two-Colour Heterojunction Unipolar Nanowire Light-Emitting Diode by Tunnel Injection. *Nanotechnology* **2007**, *18*, 395201.

154. Smith, T.; Guild, J. The C.I.E. Colorimetric Standards and Their Use. *Trans. Opt. Soc*. **1931**, *33*, 73-134.

155. Sekiguchi, H.; Kishino, K.; Kikuchi, A. Emission Color Control from Blue to Red with Nanocolumn Diameter of InGaN/GaN Nanocolumn Arrays Grown on Same Substrate. *Appl. Phys. Lett.* **2010**, *96*, 231104.

156. Law, M.; Sirbuly, D. J.; Johnson, J. C.; Goldberger, J.; Saykally, R. J.; Yang, P. Nanoribbon Waveguides for Subwavelength Photonics Integration. *Science* **2004**, *305*, 1269-1273.